Faculty of Physics and Astronomy
University of Heidelberg

Diploma Thesis in Physics

submitted by

FLORIAN KOCH
born in Darmstadt

2008

Nonlinear dynamics in the harmonically driven barrier

This diploma thesis has been carried out by FLORIAN KOCH at the

Physikalisches Institut der Universität Heidelberg

under the supervision of

PROF. DR. PETER SCHMELCHER

Abstract:

Subject of this thesis is the investigation of classical nonlinear dynamics in the system of a single driven square potential barrier with harmonically oscillating position. We analyze the system by using various analytical and numerical tools. The driven barrier can be described by just two effective parameters and possesses, for a specific range of parameters, a stable periodic orbit of period four that leads to an elaborate KAM structure in phase space. We derive for which parameters the stable orbits exists and study the parameter dependence of the fractal phase space structure. To locate the unstable periodic orbits of higher periods and their stable and unstable manifolds we use an advanced numerical method introduced in Ref. [1]. Due to the stable periodic orbits the driven barrier is a chaotic scatterer and shows typical stickiness effects. We analyze the fractal structure of the scattering functions, calculate the uncertainty dimension and study the connection between the stable manifolds of the unstable periodic orbits and the sticky initial conditions. Finally, we return to the transmission of an Gaussian-shaped ensemble through the barrier and make comparisons with quantum mechanical results in the literature.

Zusammenfassung:

Gegenstand dieser Diplomarbeit ist die Untersuchung der klassischen nicht-linearen Dynamik einer harmonisch getriebenen Barriere. Dazu benutzen wir verschiedene analytische Werkzeuge und numerische Simulationen. Das System lässt sich nach einer Umskalierung durch nur zwei effektive Parameter beschreiben. Erstaunlicherweise exististiert, für einen gewissen Bereich dieser Parameter, ein stabiler periodischer Orbit gebundener Teilchen der Periode vier. Dieser periodische Orbit ist von einer elliptischen KAM Insel und deren typischer fraktaler Struktur umgeben. Wir leiten die Position dieses Orbits und den Parameterbereich, in dem dieser Fixpunkt existiert, analytisch ab und untersuchen qualitativ die Parameterabhängigkeit der Phasenraumstruktur um diesen Fixpunkt. Zusätzlich berechnen wir mit Hilfe einer numerischen Methode aus Ref. [1] die Positionen der instabilen periodischen Fixpunkte und untersuchen die stabilen und instabilen Mannigfaltigkeiten dieser instabilen Orbits. Die KAM Insel im Phasenraum führt zu chaotischen Streueigenschaften des Systems, wie z.B. stickiness. Wir studieren die fraktalen Teile der Streufunktionen, bestimmen die Wahrscheinlichkeitsverteilung der Aufenthaltszeit und berechnen die uncertainty dimension der Streufunktion. Die Transmissionswahrscheinlichkeit eines gaussförmigen Teilchenpackets durch die Barriere zeigt die typischen Resonanzen, die schon früher in equivalenten quantenmechanischen Systemen gefunden wurden. Mit Hilfe unserer genauen Kenntnisse des Phasenraums und der elementaren Streuprozesse können wir diese Resonanzen im Detail erklären.

Contents

Chapter 1

Introduction

Periodically driven potentials quite naturally appear in many areas of current research activity, particularly in mesoscopic electronic semiconductor devices and other micro- and nanostructures driven by external voltages or applied laser fields. They also play a role in ultra cold atomic wave packets exposed to optical barriers and other photo-induced dynamics in strong laser fields or dissociation processes of molecules on solid surfaces. The strong external driving of the system typically leads to nonlinear quantum effects and chaos in the corresponding classical systems. Two archetypical potentials have been investigated in detail in the literature, the driven potential well and the driven potential barrier.

A laterally oscillating potential well is often the result of a "Kramers - Henneberger" transformation of an ac-driven static potential. The oscillating square well possesses a stable KAM island of trapped orbits and is therefore a chaotic scatterer. In the quantum regime the scattering shows resonant behavior which can be described by an effective potential with semi-stable bound states. (Ref. [2]) Additionally, the authors find signatures of the classical phase space structure in Wigner representations of propagated wave packets. The tunneling through a quare well with oscillating potential height behaves similar and exhibits a rich structure of sidebands due to multiphoton processes, see Ref. [3], Ref. [4] and also Ref. [5] for an analysis of a smooth potential well with oscillating bottom. The Floquet-states and the avoided crossings of the energy spectrum of driven potential wells are calculated in Ref. [6] and Ref. [7]. Finally, there is a study of the tunneling process in a driven double-well potential, Ref. [8].

The transmission through a Gaussian shaped oscillating potential barrier was first analyzed in Ref. [9] for a driving of the amplitude or position of the barrier in the classical and the quantum regime. The transmission function in these systems shows resonances for low incident energies when the interaction time and the oscillation period are of similar order of magnitude. This is explained by an effective potential that allows tunneling into bound states. Resonances in the tunneling probability also appear in the driven Eckart barrier (Ref. [10]) and in the ac-driven square potential barrier (Ref. [11] and Ref. [12]). The scattering of this ac-driven square barrier splits an initial wave packet into several separated pulses (Ref. [13]).

Although some of these works calculate the transmission function of classical particles through the ac-driven square barrier, the phase space structure of the

system is so far unknown. This is a major flaw, because the knowledge about the phase space is necessary to understand the scattering process. There is also so far no explanation of the resonances in the transmission function in the classical regime found in Ref. [9].

The aim of this work is to close this gap and to provide a comprehensive survey of the periodically driven square barrier with oscillating position in the classical regime. We will analyze the entire phase space, where we find stable KAM islands, the underlying dynamics and the chaotic scattering process. We also want to explore the full range of possible system parameters.

Our work is organized as follows: In chapter 2 we will introduce the mathematical model, derive effective parameters and cover the numerical aspects of the simulation. In chapter 3 we analyze the phase space of the system and explain the existence of trapped particles. We find stable periodic orbits, a KAM structure of sub-islands and unstable periodic orbits of higher periods. In chapter 4 we deal with the scattering on the driven barrier and come to a deep understanding of the system as a chaotic scatterer. We will also compare the transmission of a classical ensemble through the oscillating barrier with the quantum mechanical results in chapter 4.

Chapter 2

The model of the driven barrier

2.1 Mathematical model

2.1.1 The barrier

In this chapter we will study the problem of a single oscillating barrier and introduce its properties. Our classical system consists of a one-dimensional laterally oscillating potential of a finite and constant height. The driving function is assumed to be harmonic.

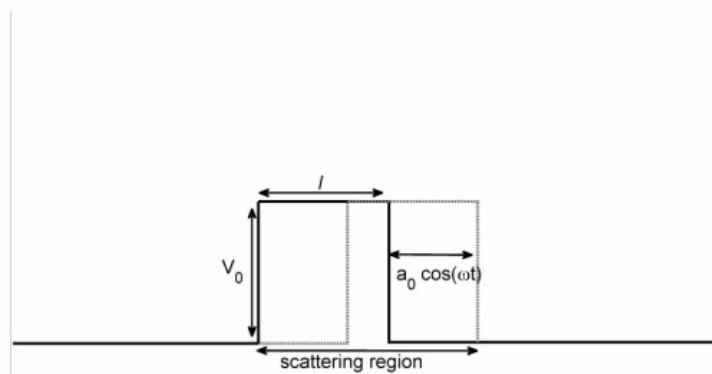$$V(x,t) = V_0 \Theta(\frac{l}{2} - |x - a_0 \cos(\omega t)|) \tag{2.1}$$

Figure 2.1: The model of the driven barrier.

This kind of potential is typically the result of a "Kramers-Henneberger" transformation of an ac-driven static potential. An informative example has been provided by Henseler et al. in [2] who have applied the transformation on a potential well though not on a potential barrier.

2.1.2   Discrete dynamics and the mapping

Although the dynamics of the system are continuous, the interaction with the barrier is point like. The forces acting on the particles are delta-shaped:

$$F(x,t) \sim \delta\left(x - a_0 \cos(\omega t) - \frac{l}{2}\right) - F\delta\left(x - a_0 \cos(\omega t) + \frac{l}{2}\right) \qquad (2.2)$$

In between collisions with one of the barrier's edges, the particles propagate ballistically. Therefore, it is sufficient to describe the dynamics in terms of a mapping between collisions.

2.1.3   Interaction with the barrier

To calculate the particle barrier interaction, we transform all coordinates into the barrier's reference frame. Even though this coordinate frame is accelerated and, therefore, not an inertial frame, momentum and energy are conserved for the interaction's infinitesimal time span.

$$x \to \tilde{x} = x - a_0 \cos(\omega t) \qquad v \to \tilde{v} = v + a_0 \omega \sin(\omega t) \qquad (2.3)$$

When colliding with the barrier from the *outside* a particle is transmitted *into* the barrier if its kinetic energy surpasses the barrier height.

$$E_{kin} = \frac{m}{2}\tilde{v}_n^2 \geqslant V_0 \qquad (2.4)$$

In this case the particle loses energy and is decelerated.

$$\tilde{v}_{n+1} = \sqrt{\frac{2}{m}(E_{kin} - V_0)} \qquad (2.5)$$

If it is not transmitted, it is reflected and its new velocity becomes simply:

$$\tilde{v}_{n+1} = -\tilde{v}_n \qquad (2.6)$$

Likewise, if a particle hits the barrier coming from its *inside*, it is always transmitted and gains energy:

$$\tilde{v}_{n+1} = \sqrt{\frac{2}{m}(E_{kin} + V_0)} \qquad (2.7)$$

Transforming these equations back to the laboratory frame yields the equations of motion:

$$v_{n+1} = v_{barrier} + \text{sign}(v_n - v_{barrier})\sqrt{(v_n - v_{barrier})^2 \pm \frac{2}{m}V_0} \qquad (2.8)$$

or if the particle is reflected:

$$v_{n+1} = 2v_{barrier} - v_n \qquad (2.9)$$

where $v_{barrier}$ is the barrier's velocity at the time of the collision and the sign $\pm$ depends on whether the particle is transmitted into the barrier $(-)$ or leaves the barrier $(+)$. These equations might seem fairly simple, but the resulting dynamics can be quite counterintuitive. A particle moving in the same direction as the barrier can for example reverse its direction of motion when leaving the barrier.

2.1.4   The time mapping

The time t_n is mapped on the time t_{n+1} of the next collision of the particle with one of the barrier's edges. Therefore t_{n+1} is the smallest time that is a solution of the equation 2.10:

$$x_{barrier}(t_{n+1}) = x_n + v_n(t_{n+1} - t_n) \tag{2.10}$$

where $x_{barrier}$ can be either edge of the barrier. This implicit equation can only be solved numerically. See section 2.3 for details.

2.2   Parametrization

The single driven barrier system has five parameters: The barrier's potential height V_0 and spatial thickness l, the driving frequency ω, the amplitude a_0 and the particle's mass m. The equations of motion (see subsection 2.1.3) however show that the number of parameters can be reduced by an appropriate scaling transformation:

$$v_{n+1} = -a_0\omega\sin(\omega t) + \mathrm{sign}\left(v_n + a_0\omega\sin(\omega t)\right)\sqrt{(v_n + a_0\omega\sin(\omega t))^2 \pm \frac{2}{m}V_0} \tag{2.11}$$

$$v_{n+1} = -2a_0\omega\sin(\omega t) - v_n \tag{2.12}$$

Scaling transformation:

$$x \rightarrow \tilde{x} = \frac{x}{a_0} \qquad t \rightarrow \tilde{t} = t\omega \tag{2.13}$$

$$\Rightarrow v \rightarrow \tilde{v} = \frac{v}{\omega a_0} \tag{2.14}$$

$$\tilde{v}_{n+1} = -\sin(\tilde{t}) + \mathrm{sign}\left(\tilde{v}_n + \sin(\tilde{t})\right)\sqrt{\left(\tilde{v}_n + \sin(\tilde{t})\right)^2 \pm \frac{V_0}{V_\omega}} \tag{2.15}$$

$$\tilde{v}_{n+1} = -2\sin(\tilde{t}) - \tilde{v}_n \tag{2.16}$$

$$\tag{2.17}$$

The only parameter left in the equations of motion is $\frac{V_0}{V_\omega}$, where $V_\omega = \frac{m}{2}a_0^2\omega^2$ is the maximum kinetic energy a particle, which is at rest in the laboratory frame, can have in the barrier's frame of reference. V_ω would be the barrier's maximal kinetic energy if its mass was equal to the particle's mass m. The second parameter, $\frac{l}{a_0}$, is the barrier's thickness measured in units of the amplitude and appears in the implicit equations (2.18) for the time mapping and is equal to the thickness of the barrier in the new coordinates:

$$\cos(\tilde{t}_{n+1}) + \frac{l}{a_0} = \tilde{x}_n + \tilde{v}_n(\tilde{t}_{n+1} - \tilde{t}_n) \tag{2.18}$$

In the following we will use the parameters $\frac{l}{a_0}$ and $\frac{V_0}{V_\omega}$. Alternatively, we could use the oscillation's amplitude and frequency as parameters. $\frac{V_0}{V_\omega}$ and $\frac{l}{a_0}$ have the advantage of being independent of each other, whereas a_0 and ω are linked to each other by equation (2.13).

2.3   Numerics

The primary challenge in the simulation of this classical system is to calculate
the next collision time, that is the next time the particle hits one of the edges
of the barrier. This requires, in general, that we solve the following type of
implicit equation

$$x_b(t_{n+1}) = x_n + v_n(t_{n+1} - t_n) \qquad (2.19)$$

where x_b is either the right edge ($x_b(t) = \cos(t) + l$) or the left edge ($x_b(t) =
\cos(t)$) of the barrier. (We are using the transformed effective parameters de-
veloped in section 2.2.) For a particle outside of the potential we only need
to find the next collision time with the side of the barrier facing the particle.
For particles inside the potential we calculate the collision times of both edges.
The physically correct solution is, of course, the smaller of these two times. If
equation (2.19) has no solutions ($t_{n+1} > t_n$) the particle does not collide with
the barrier again and escapes. The implicit equation (2.19) can be solved by
translating it into a root finding problem. (In the following, we will calculate
the collision time with the left edge.)

$$f(\Delta) := \cos(t_n + \Delta t) - x_n - v_n \Delta t = 0 \qquad (2.20)$$

The time difference Δt is required to be larger then zero. Equation (2.20)
can only be solved numerically and there are many powerful numerical tools
to find a root of a function. Our problem is that we are not searching for *any*
root, but for the *first* root of the function f. Only the first solution of equation
(2.20) corresponds to a physically meaningful collision with the barrier, all other
solutions are artificial. It is very important that we can guarantee that our
algorithm always finds the first root of f, because quasi periodic or sticky orbits
are very error sensitive. However, the problem of finding the first root of an
arbitrary differentiable function is, mathematically, *not solved*.

By using the particular properties of equation (2.20) we have been able to
develop a method that allows us to precisely and efficiently locate the correct
root of the function f in this system. This approach can also be used to solve
similar types of equations. In the following, we will explain our algorithm in
detail.

2.3.1   The van Wijngaarden-Deker-Brent Method

The Brent method is a very useful algorithm for finding the root of a continuous
function f. It combines bisection method with an inverse quadratic interpolation
to guarantee convergence. Just like the bisection method, the Wijngaarden-
Deker-Brent method expects as input a bracketing interval $[a, b]$ which contains
an odd number of roots, i.e. $f(a) \cdot f(b) < 0$. The algorithm then attempts to
apply an inverse quadratic interpolation to the pairs of points $(f(a), a)$, $(f(b), b)$
and $(f(c), c)$, where $c \in [a, b]$ is the current best estimate of the root of the
function f. The initial guess for the root in the first iteration is $c = \frac{b-a}{2}$.
An inverse quadratic interpolation is simply a quadratic interpolation taking x
as a function of $f(x)$. This quadratic method works usually well for smooth
functions, but it risks giving very bad estimates c of the root and can also
fail due to numerical limitations, such as numerical extinction errors. If the
inverse quadratic interpolation fails or the next estimate c lies outside of the

bracketing interval $[a, b]$, Brent's method applies a bisection step to the interval. This means that the interval is divided into two subintervals $[a, \frac{b-a}{2}]$ $[\frac{b-a}{2}, b]$. Since f is continuous, at least one interval contains a root of the function, i.e. $f(a) \cdot f(\frac{b-a}{2}) < 0$ or $f(b) \cdot f(\frac{b-a}{2}) < 0$. The interval which is bracketing the root is then used as the new interval $[a', b']$ in the next iteration. For well-behaved functions Brent's method converges quadratically while the bisection element guarantees at least linear convergence for problematic functions. Brent's method does not use the derivative of the function f. We could use a slightly faster algorithm that takes the derivative into accounts as well instead of Brent's method, because the derivative of equation (2.20) is very simple. We did not do this because we wanted to write a code that can be applied also to those problems in which the derivative might get quite complicated. We use the implementation of Brent's method presented in Numerical Recipes in C, Ref. [14].

The major weakness of the Wijngaarden-Deker-Brent method is that it requires that we know an interval $[a, b]$ bracketing an odd number of roots beforehand. Actually, we have to find an interval that contains only one root. If the bracketing interval includes more than one root (an odd number), the Brent method will converge to any arbitrary root, but not necessarily to the first root. In the following, we will describe how an appropriate bracketing interval can be found.

2.3.2 The grid bracketing

The standard approach to find a bracketing interval is to start with a relatively large interval $[a, b]$ that is guaranteed by geometric properties of the system to contain the first root. This interval will usually bracket an unknown number of roots, thus the Brent method, or any other similar algorithm, cannot be applied directly to the interval $[a, b]$. The interval $[a, b]$ is then divided into n small subintervals ($[a_0, b_0]$, $[a_1, b_1]$,...), where n has to be sufficiently large so that each subinterval can bracket at most *one* root. We can then find the first interval $[a_i, b_i]$ which contains a root of f by simply comparing the sign of f at the edge points of the intervals, if $f(a_i) \cdot f(b_i) < 0$ the interval $[a_i, b_i]$ contains a root. The interval $[a_i, b_i]$ can now be used as the bracketing interval for Brent's method.

The problem of this approach lies in the fact that the roots of f can, even in our simple system, lie arbitrarily close to each other. An illustrative example is plotted in Fig. 2.2. The scenario shown in Fig. 2.2 is by no means exotic, it naturally comes up whenever an extremal value of f lies very close to zero. In situations in which two roots have a separating distance d smaller then the size of the subintervals, i.e. $d < |b_i - a_i| = \frac{b-a}{n}$, the grid bracketing will fail to detect these roots, because the sign of f at the endpoints is identical, $f(a_i) \cdot f(b_i) > 0$. The probability of missing a root can be reduced by choosing very small subintervals, but only a subinterval size close to the numeric precision is sufficient to avoid all errors. (If the distance d between the roots is smaller than the numeric precision, it is not possible to detect the roots anyway.) The other problem is that this method becomes extremely slow for large n, especially if we reduce the subinterval size to detect all zero crossings of f. In practice it is not possible to set n much larger than 10^6, and even then the algorithm will still miss some roots while being painfully slow. Therefore we avoid this
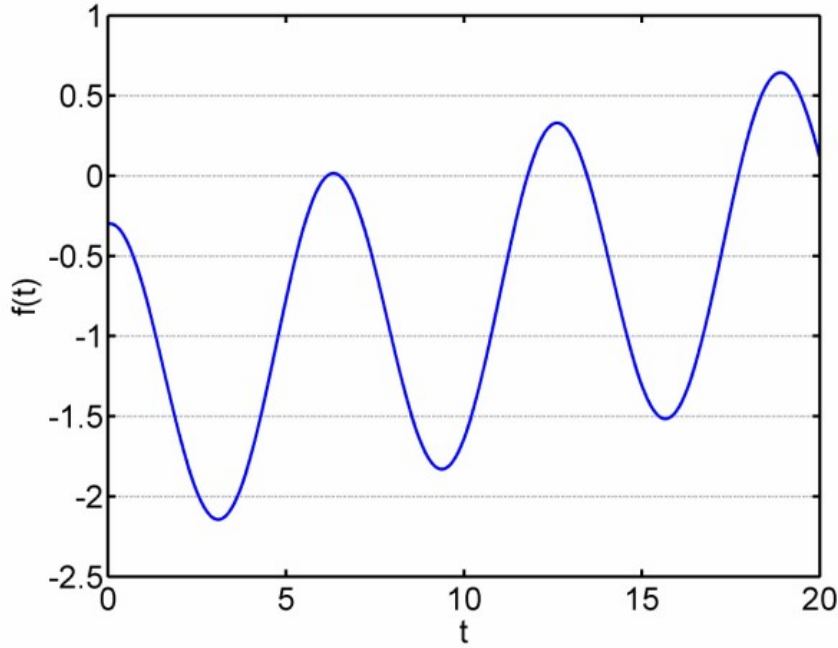
Figure 2.2: Example for the function f in equation (2.20)

method and use a completely different bracketing that deals with the problem of close roots.

2.3.3   The bracketing by extremals

In many driven classical systems, for example driven billiards, we search for the roots of a function that describes the distance between a particle and a potential barrier. Therefore it is possible to derive a minimum distance between the extremal values of the function f from the geometry of the system and the driving function. In our system here, this distance would simply be half of the period, $\frac{T}{2} = \frac{\pi}{\omega}$. This minimum distance allows us to use various powerful tools, similar to Brent's method, to locate the extremals of f. It is much easier to compute the extremals of f than to compute the roots of f, because the extremals have a typical distance to each other. We can, for example detect the extremal values by covering the interval $[a, b]$ with a very coarse grid and apply a root searching algorithm on the derivative of f. Other dedicated methods to find extremals are described in Ref. [14]. These extremals can then be used as bracketing intervals for the roots of f, because f is a continuous function and therefore all roots are bracketed by extremals. This way we can even dissolve pairs of very close roots. The extremals don't have to be calculated with maximal precision, it suffices to compute a good approximation.

In our case here it is actually trivial to find the extremals of f. The derivative of equation (2.20) is just a sinus function.

$$f' = -\sin(t_n + \Delta t) - v_n \tag{2.21}$$

The extremal value t_x can be computed setting the derivative f' to zero and using the inverse sine function:

$$t_x = \arcsin(-v_n) \tag{2.22}$$

For $v_n > 1$ this equation (2.22) does not have a solution, which means that equation (2.20) has only up to one solution and thus we can apply Brent's method directly. For $v_n \leq 1$ the solution of equation (2.22) is not unique due to the periodicity of the driving law. Therefore we have to shift the extremal value by a suitable multiple of the period T to get the bracketing of the root we are searching. With this bracketing we use Brent's algorithm to find the first solution of equation (2.19). This way, we are able to compute the collision times for the mapping in the system of the driven barrier in a very reliable and numerically efficient way.

Chapter 3

Trapped particles

In this chapter we will investigate the phase space structure of the system. We found that for some parameters the driven barrier possesses a stable periodic orbit of period 4. This means that, through the driving, the repulsive potential can trap particles in a small part of phase space. In the following, we will investigate this central periodic orbit, the quasi-periodic orbits around it, the fractal structure of sub-islands and of unstable periodic orbits, and, finally, also analyze how they depend on the system's parameters.

3.1 Poincaré surface of sections

A Poincaré section is generally used to generate a discrete (n-1)-dimensional map of an n-dimensional phase flow by mapping the orbits' intersections with a plane transversal to the flow. By mapping only intersections in one direction we gain a well-defined and characteristic map of the phase space. The phase space of the oscillating barrier has three dimensions: time, position and velocity of the particle. Because the phase flow of billiard systems is discrete by itself, we map all collisions of the particle with either side of the barrier to the Poincaré section. This is equivalent to mapping all intersections of the trajectories with the two-dimensional manifold Ω defined by the barrier's motion:

$$\Omega = \begin{pmatrix} t \\ x_b(t) \\ v \end{pmatrix} \qquad t, v \in \Re$$

Where $x_b(t)$ is the position of either of the barrier's edges. Since the driving function is assumed to be periodic it is possible to restrict the time t to the interval $[0, 2\pi]$. It is important to note that the mapping M itself only operates on the manifold defined by Ω, because it always maps a point in phase space on the point of the next collision with the barrier. The Poincaré section is made unique by plotting only particles which have been transmitted into the barrier after collision or by mapping only collisions with one chosen edge instead of all collisions. In that case the position and phase φ, defined as $\omega t \mod 2\pi$, are uniquely connected by the driving function and one of the coordinates becomes redundant. In the following, we will discuss Poincaré sections in which we plot the particle's velocity over the phase φ of the oscillating barrier.

3.2   Quasiperiodic orbits

We covered the entire phase space with a fine grid of initial conditions to guarantee that all relevant structures are being shown in our Poincaré sections. We found that it suffices to use the following type of initial conditions: We iterate an ensemble of 200 particles for up to 4000 collisions, particles that have left the scattering region are not iterated further. Their initial phase is uniformly distributed in $[0, 2\pi]$, the initial velocity is zero and the initial position is equal to the left edge of the barrier for $\varphi \in [0, \pi]$, and equal to the right edge for $\varphi \in [\pi, 2\pi]$ just outside of the potential. This choice of initial position ensures that the initial phase is also the phase of the first collision. The resulting Poincaré section is plotted in Fig. 3.1. The initial ensemble is visible as a dotted horizontal line at $v = 0$. These plots show the velocity of particles after a collision as a function of the collision's phase. The system's parameters are: $\frac{V_0}{V_\omega} = 0.32$ and $\frac{l}{a_0} = 0.4$ These parameters are typical for an experimental setup using micro- and nanostructures driven by external voltages of applied Laser fields.
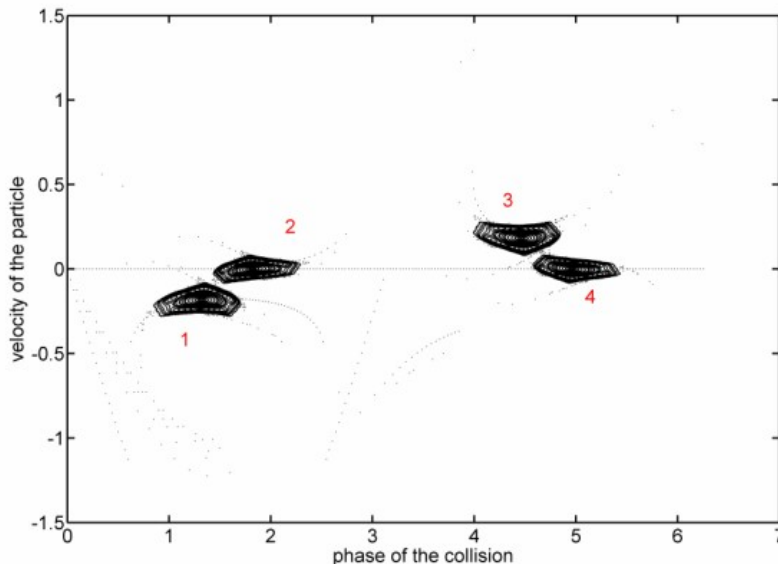

Figure 3.1: A typical Poincaré section showing trapped particles

Initial phases between [0.88, 1.69] and correspondingly [4.0, 4.81] lead to a bound motion on quasi-periodic orbits. (Fig. 3.1 shows the velocity of particles *after* the collision, therefore the initial conditions leading to bound motion are *not* simply the intersection of the initial conditions with the stable orbits.) These orbits are shown in Fig. 3.1 and belong to elliptic islands around stable fixed points of period 4 at their centers. Each line is the trajectory of exactly one trapped particle. The central fixed points correspond to one orbit of period 4 which will be analyzed in detail in section 3.3. Not all bound orbits are regular: An enlargement of the fourth island in Fig. 3.1 is plotted in Fig. 3.2. The central elliptic fixed point is surrounded by a chain of sub-islands which
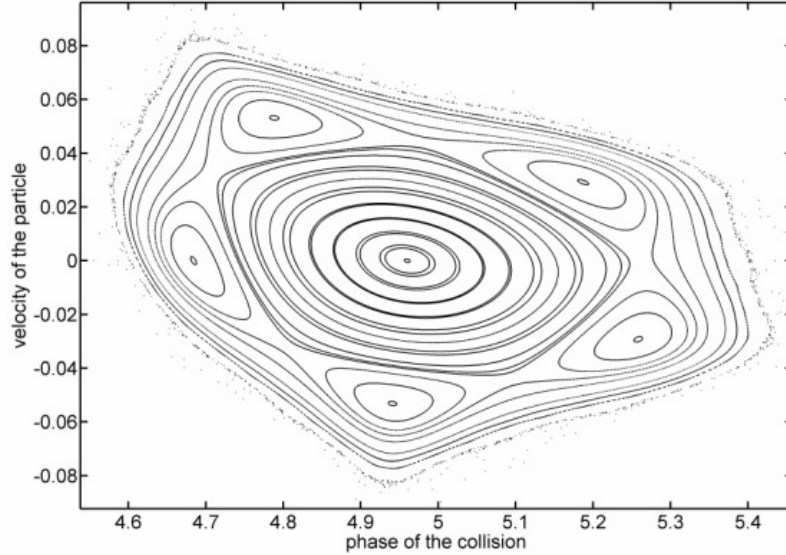
Figure 3.2: Enlargement of structure 4

is the remnant of a dissolved quasi-periodic orbit. (See section 3.6 for details.) The separatrix around these sub-islands can sustain a chaotic layer of orbits which are bound by the outermost regular orbit, since in Hamiltonian systems regular trajectories cannot cross each other in phase space. The outermost regular orbit is surrounded by a thin chaotic layer of unbound particles that leave the scattering region after many collisions. This effect is called stickiness. (See subsection 4.2.2.) The space outside the stable orbits contains only few points because this part of phase space is visited only be trajectories which leave the open system after a few collisions, whereas those on regular orbits stay in the scattering region indefinitely (We tested this numerically for up to 10^{11} collisions). The dynamics of the scattering trajectories will be investigated in section 4. The Poincaré section in Fig. 3.1 is *not* unique because it shows all collisions, both from inside and outside the barrier. The structures with mean velocity of zero and phases in [1.4, 2.3] or [4.5, 5.4], numbered 2 and 4, correspond to collisions from inside the barrier, the structures in [0.88, 1.69] and [4.59, 5.40], numbered 1 and 3, belong to collisions from outside.

The four regular islands are in fact instances of the same structure. The first and second structures are identical to the third and fourth with their phases increased by π and the sign of their velocity inverted. This reflects the symmetric properties of the driving function $a_0 \cos(\omega t)$: $\cos(\pi - \varphi) = \cos(\pi + \varphi)$ and $\cos(\pi/2 - \varphi) = -\cos(\pi/2 + \varphi)$

The dynamics of all particles on bound orbits are identical:

Structure 1: Starting left of the barrier, the particle collides with the left edge and is transmitted into the barrier. The barrier's momentum transfer accelerates the particles in negative direction.

Structure 2: The barrier overtakes the particle inside of it until it collides with the

barrier's right edge. Here the momentum transfer decelerates the particle, resulting in the second structure.

Structure 3: After the barrier has reached its minimum position and turning point at $\varphi = \pi$, it moves in positive direction and the particle collides with the right edge. The momentum transfer accelerates the particle in positive direction.

Structure 4: The barrier again overtakes the particle inside until it collides with the barrier's left edge, where it leaves the potential and is decelerated into the last structure. Afterwards the barrier reaches its maximum position and the cycle starts again.

It is important to note that for most sets of parameters the bound particles' velocity is lower then the barrier's maximum velocity. An x-t-plot of a trapped particle with initial phase $\varphi = 5.1$ can be seen in Fig. 3.3. The particle is plotted in red and the two edges of the barrier are plotted in blue. This plot shows both modes of the motion: the periodic hopping between the four structures and an overlaid harmonic oscillation. This sinusoidal motion is represented as closed orbit in the Poincaré section. The frequency of this harmonic oscillation, measured by a Fourier transformation, is equal to the frequency by which the particles rotate on the quasi-periodic orbit around the elliptic fixed points in the Poincaré section. The rotation is clockwise in the islands 3 and 4 and it is anticlockwise in the islands 1 and 2.
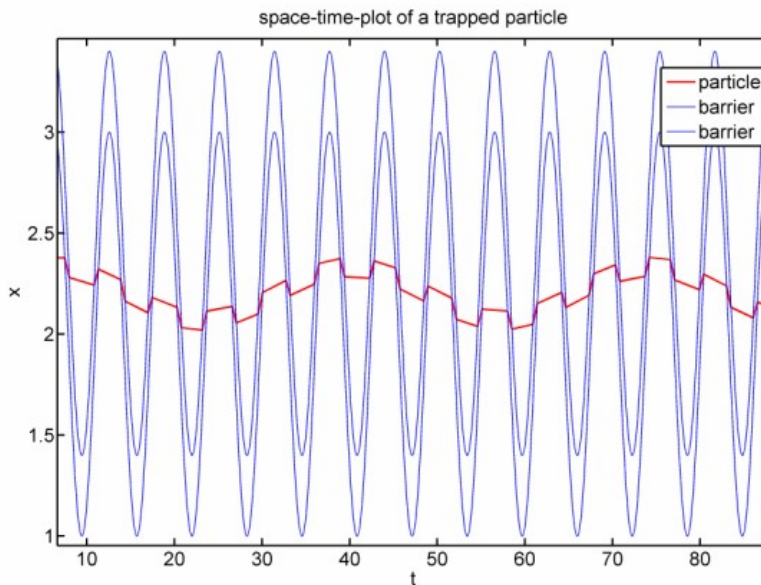

Figure 3.3: Motion of a trapped particle. The red line represents the particle, the two blue lines represent the edges of the barrier.

3.3   Central elliptic fixed points

It is possible to calculate the position of the central elliptic fixed points, here we will do it for island number 1. As a plot of the trajectory in Fig. 3.4 shows, the particle's velocity is zero when it is outside the barrier. ($v_0 = v_2 = 0$) The collision points are symmetric around $\frac{\pi}{2}$ in their phases φ_1 and φ_2 and around the equilibrium position in their positions x_1 and x_2.
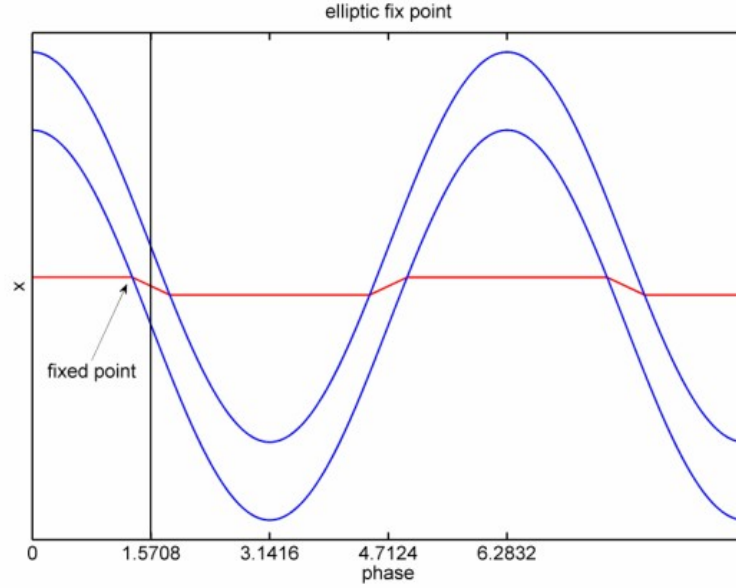

Figure 3.4: Trajectory of the central fixed point

Thus the velocity after the first collision has to be:

$$v_1 = \frac{\Delta x}{\Delta t} = -\frac{x_b(\varphi_1) - \frac{l}{2}}{(\frac{\pi}{2} - \varphi_1)/\omega} \qquad x_b(\varphi_1) = a_0 \cos(\varphi_1) \qquad (3.1)$$

, where x_b is the position of the left edge of the barrier. This velocity can be calculated from equation (2.8):

$$v_1 = v_b(\varphi_1) + \text{sign}\left(v_0 - v_b(\varphi_1)\right)\sqrt{\left(v_0 - v_b(\varphi_1)\right)^2 - \frac{2}{m}V_0} \qquad (3.2)$$

The initial velocity v_0 is zero and $v_b = -a_0\omega\sin(\varphi)$. The result is an implicit equation for φ_1:

$$f(\varphi_1) := -\left(\frac{\cos(\varphi_1) - \frac{l}{2a_0}}{\frac{\pi}{2} - \varphi_1}\right)^2 + 2\sin(\varphi_1)\frac{\cos(\varphi_1) - \frac{l}{2a_0}}{\frac{\pi}{2} - \varphi_1} = \frac{V_0}{\frac{m}{2}a_0^2\omega^2} = \frac{V_0}{V_\omega} \quad (3.3)$$

Where V_ω is the maximum kinetic energy a particle, which is at rest in the laboratory frame, can have in the barrier's frame of reference. This implicit equation determines the phase of the first elliptic point. The left side of the equation is plotted for different values of $\frac{l}{a_0}$ in Fig. 3.5.
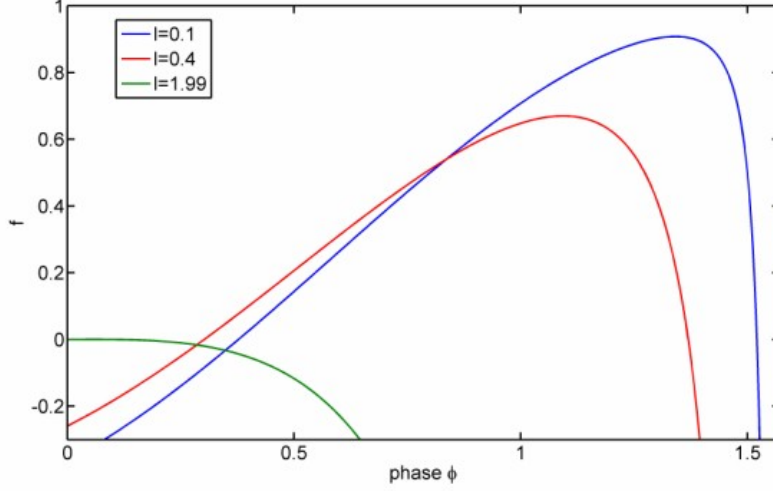
Figure 3.5: Function f, defined in equ. (3.3), for different values of l

For values of $\frac{l}{a_0}\epsilon[0,2]$, the equation $f(\varphi) = \frac{V_0}{V_\omega}$ has two solutions in the interval $[0, \frac{\pi}{2}]$. The physically relevant solution lies to the right of the function's maximum. The plots show that the implicit equation (3.3) has no solutions for $\frac{V_0}{V_\omega} > f_{max}$, where f_{max} is the function's maximum value. This means that the barrier's potential is too strong to allow for stable orbits. The function has no positive values for $\frac{l}{a_0} \geq 2$ and the second root is greater than $\frac{\pi}{2}$ for $\frac{l}{a_0} = 0$. The elliptic orbits disappear in both cases. Figure 3.6 shows the maximal value of $f(\varphi)$ as a function of $\frac{l}{a_0}$. Only pairs of parameters $(\frac{V_0}{V_\omega}, \frac{l}{a_0})$ *below* the curve allow for regular motion. For sets of parameters $(\frac{V_0}{V_\omega}, \frac{l}{a_0})$ above the curve in Fig. 3.6 the phase space contains no bound orbits. To be precise, the central periodic orbit does not become unstable for other parameters. It really ceases to exist!

The maximal values of $\frac{V_0}{V_\omega} = 1$ and $\frac{l}{a_0} = 2$ can be easily understood: V_ω is the maximum kinetic energy particle can have in the barrier's frame of reference if it is at rest in the laboratory frame. If V_0 is greater than V_ω, then particles with velocity of zero will never be transmitted into the barrier. Since all stable orbits cross the $v = 0$ axis, this would destroy all stable orbits. For $l > 2a_0$, v_1 in equation (3.1) would have to be negative, which is forbidden by equation (3.2).

The phases of the other fixed points can be calculated from the position of the first by using the symmetry properties of the driving function: $\cos(\pi - \varphi) = \cos(\pi + \varphi)$ and $\cos(\pi/2 - \varphi) = -\cos(\pi/2 + \varphi)$

$$\varphi_2 = \pi - \varphi_1$$
$$\varphi_3 = \pi + \varphi_1$$
$$\varphi_4 = 2\pi - \varphi_1$$

The phase φ of the first fixed point is plotted as a function of $\frac{2V_0}{V_\omega}$ for different values of $\frac{l}{a_0}$ in Fig. 3.3. The numerical simulations reproduce this analytic
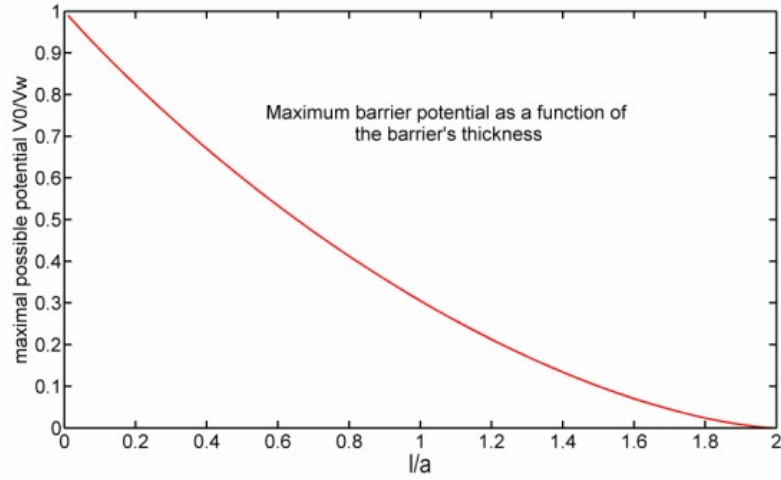
Figure 3.6: The parameters allowing periodic orbits. Only pairs of parameters below the this curve allow for stable orbits.
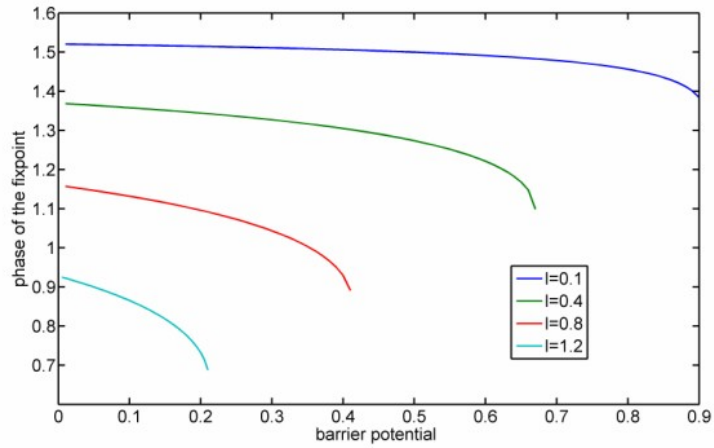
prediction very well.

Figure 3.7: Phase of the fixed point for different parameters

3.4 Parameter dependence of the phase space structure

In section 3.2 we mentioned that not all bound orbits are regular. As an example for this, we plot the Poincaré section for $\frac{V_0}{V_\omega} = 0.308$ and $\frac{l}{a_0} = 0.4$ in Fig. 3.8 and an enlargement of the separatrix around the sub-islands. At these parameters the separatrix has dissolved into a thin chaotic layer. In the enlargement one

can also see the complicated fractal structure at the edges of the stable orbits.

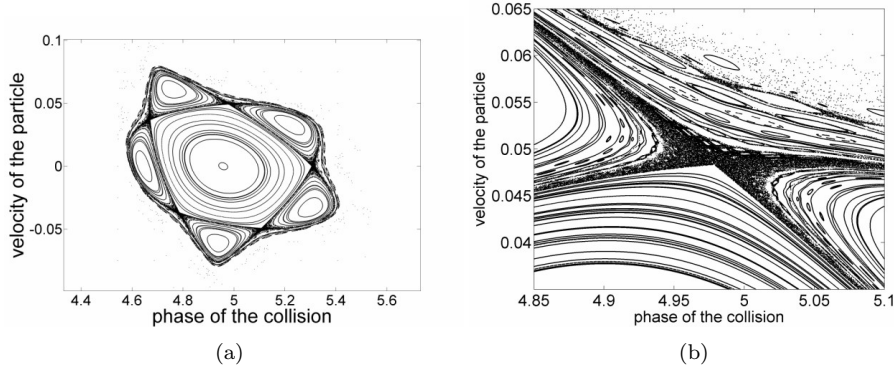(a)   (b)

Figure 3.8: A chaotic layer inside the stable island

The shape and size of the stable island in the Poincaré sections change with the parameters. The five elliptic sub-island in Fig. 3.2 are typical for the phase space structure: The central fixed point and the quasi-periodic orbits are surrounded by a chaotic layer with a fractal structure of stable and unstable periodic orbits. (See section 3.6 and 3.7.) Additionally, there exist one or more sets of stable periodic orbits that form large and distinguished sub-islands, inside the main island, as shown in Fig. 3.2, or outside of it. Keeping $\frac{l}{a} = 0.1$ constant while increasing $\frac{V_0}{V_\omega}$, the sequence of primary sub-islands follows a simple pattern: With increasing $\frac{V_0}{V_\omega}$, the periodic orbits of period n move from the outer edge of the stable island towards the central fixed point. This means that the dissolved orbit, from which the chain of sub-islands was formed shrinks and ultimately disappears. Simultaneously, a new set of periodic orbits forms at the edge of the stable region. The period of this new orbit is $2(n-1)$ for odd and $\frac{n}{2} - 1$ for even n, e.g. the sequence is $16, 7, 12, 5, 8, 3$. The starting point is the limit of very small $\frac{V_0}{V_\omega}$, where the sub-islands form almost a continuum that can not be resolved numerically in Fig. 3.10(a).

This sequence continues until the last periodic orbits have disappeared and the stable island takes a triangular form in Fig. 3.9(e). At these parameters the volume of the stable region has a minimum, as shown in Fig. 3.12. After this minimum the sequence is inverted as new sub-islands form in the border layer and move inside the stable island. It is very difficult to investigate this process further because the scale on which $\frac{l}{a_0}$ has to be changed becomes extremely small and because the stable region itself begins to shrink away. The development of the substructures is shown for a constant $\frac{l}{a} = 0.1$ and increasing $\frac{V_0}{V_\omega}$ in Fig. 3.9. It should be noted that the shape of the sub-islands also changes with the parameters according to this sequence but on a much smaller scale of the parameters.

Fig. 3.10 and Fig. 3.11 show two series of Poincaré sections taken at $\frac{l}{a} = 0.1$ and $\frac{l}{a} = 0.4$. $\frac{V_0}{V_\omega}$ was chosen so that the structures of the first and second series correspond to each other. This shows that the choice of $\frac{l}{a}$ changes only the angle of the central fixed point and the scaling of $\frac{V_0}{V_\omega}$ but does not create novel dynamics that could not be accessed by varying $\frac{V_0}{V_\omega}$.
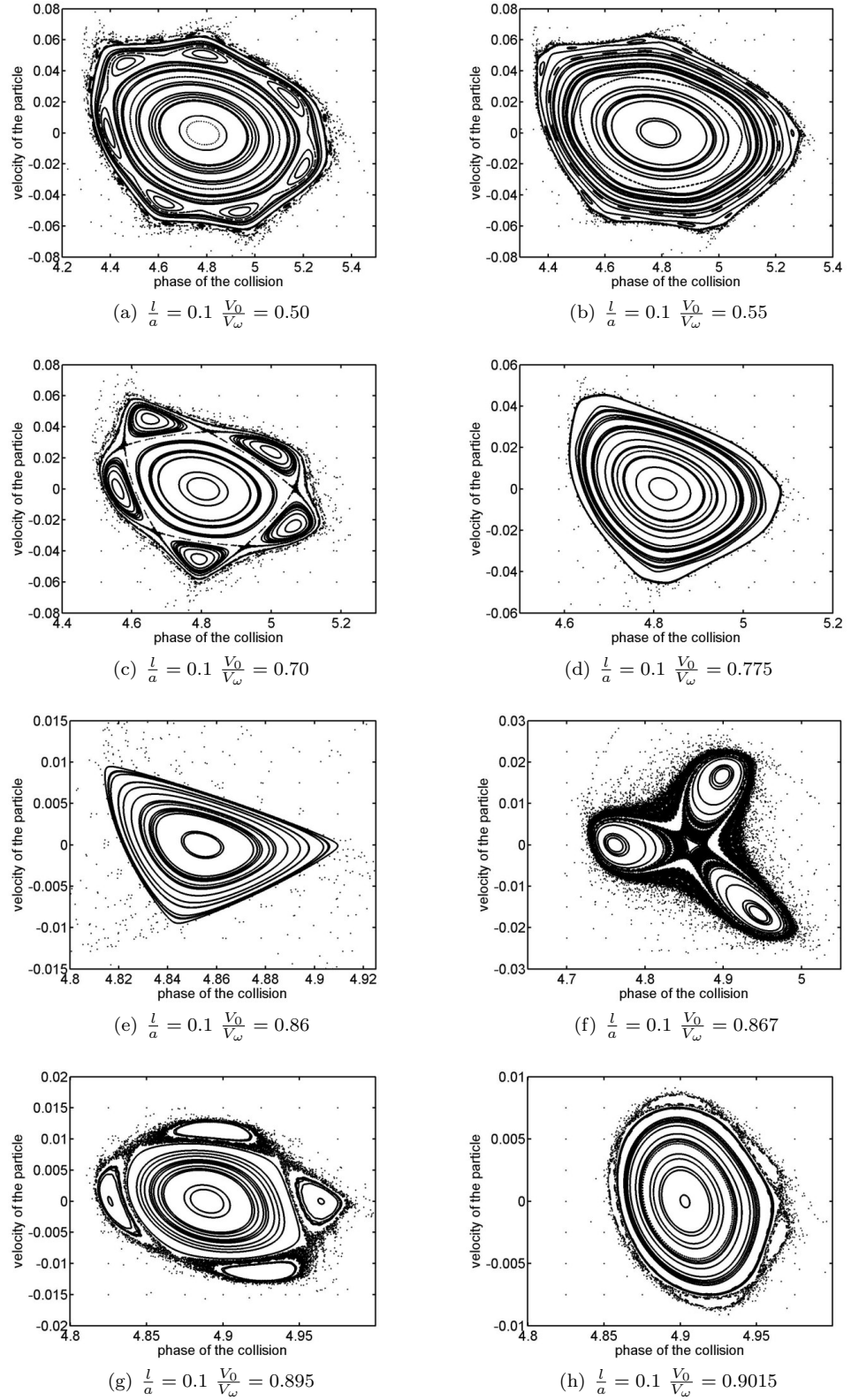
(a) $\frac{l}{a} = 0.1$ $\frac{V_0}{V_\omega} = 0.50$

(b) $\frac{l}{a} = 0.1$ $\frac{V_0}{V_\omega} = 0.55$

(c) $\frac{l}{a} = 0.1$ $\frac{V_0}{V_\omega} = 0.70$

(d) $\frac{l}{a} = 0.1$ $\frac{V_0}{V_\omega} = 0.775$

(e) $\frac{l}{a} = 0.1$ $\frac{V_0}{V_\omega} = 0.86$

(f) $\frac{l}{a} = 0.1$ $\frac{V_0}{V_\omega} = 0.867$

(g) $\frac{l}{a} = 0.1$ $\frac{V_0}{V_\omega} = 0.895$

(h) $\frac{l}{a} = 0.1$ $\frac{V_0}{V_\omega} = 0.9015$

Figure 3.9:

(a) $\frac{l}{a} = 0.1$ $\frac{V_0}{V_\omega} = 0.001$

(b) $\frac{l}{a} = 0.1$ $\frac{V_0}{V_\omega} = 0.1$

(c) $\frac{l}{a} = 0.1$ $\frac{V_0}{V_\omega} = 0.2$

(d) $\frac{l}{a} = 0.1$ $\frac{V_0}{V_\omega} = 0.324$

(e) $\frac{l}{a} = 0.1$ $\frac{V_0}{V_\omega} = 0.50$

(f) $\frac{l}{a} = 0.1$ $\frac{V_0}{V_\omega} = 0.70$

(g) $\frac{l}{a} = 0.1$ $\frac{V_0}{V_\omega} = 0.83$

(h) $\frac{l}{a} = 0.1$ $\frac{V_0}{V_\omega} = 0.907$

Figure 3.10:

(a) $\frac{l}{a} = 0.4$ $\frac{V_0}{V_\omega} = 0.001$

(b) $\frac{l}{a} = 0.4$ $\frac{V_0}{V_\omega} = 0.015$

(c) $\frac{l}{a} = 0.4$ $\frac{V_0}{V_\omega} = 0.05$

(d) $\frac{l}{a} = 0.4$ $\frac{V_0}{V_\omega} = 0.095$

(e) $\frac{l}{a} = 0.4$ $\frac{V_0}{V_\omega} = 0.160$

(f) $\frac{l}{a} = 0.4$ $\frac{V_0}{V_\omega} = 0.319$

(g) $\frac{l}{a} = 0.4$ $\frac{V_0}{V_\omega} = 0.5$
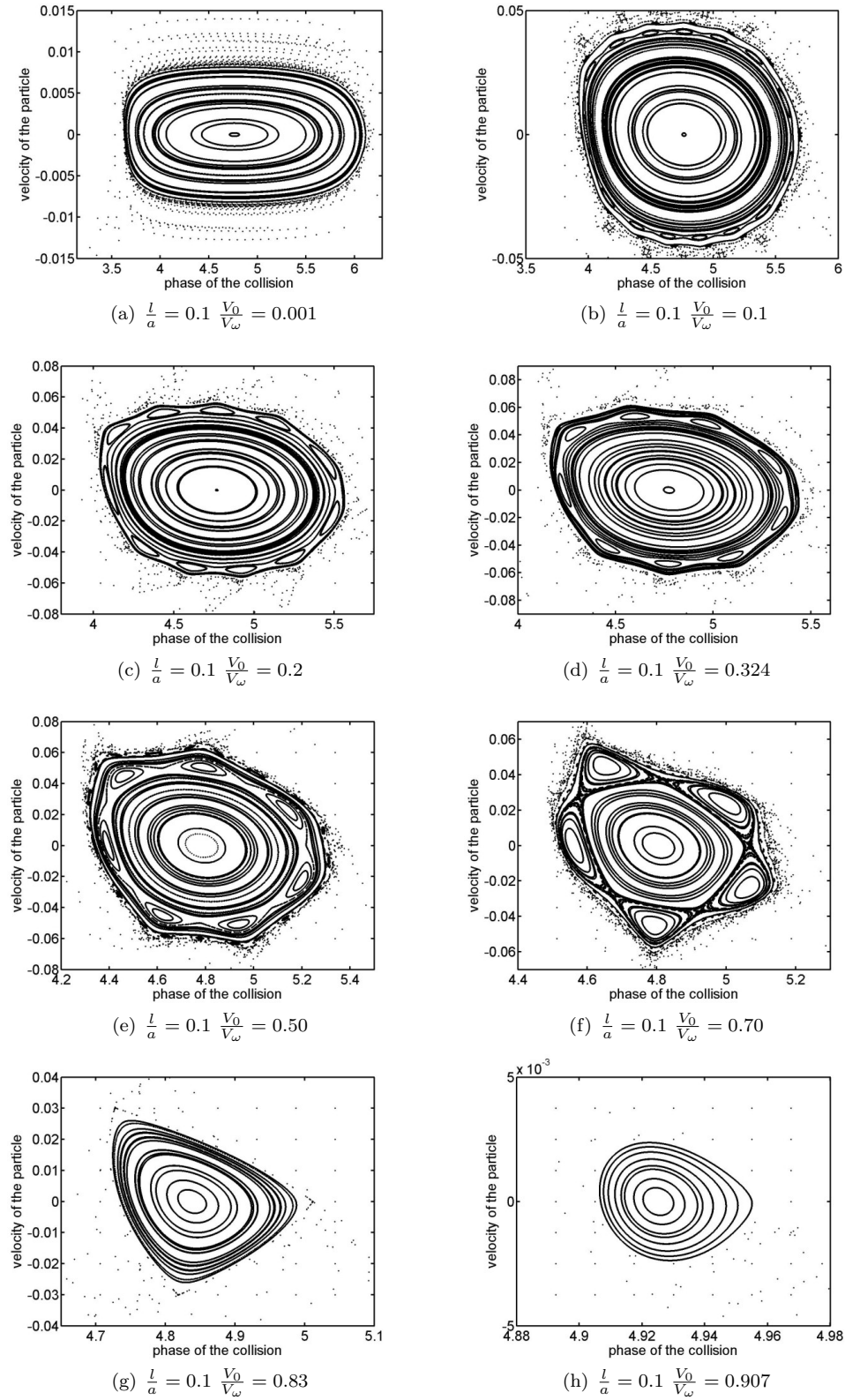
(h) $\frac{l}{a} = 0.4$ $\frac{V_0}{V_\omega} = 0.669$
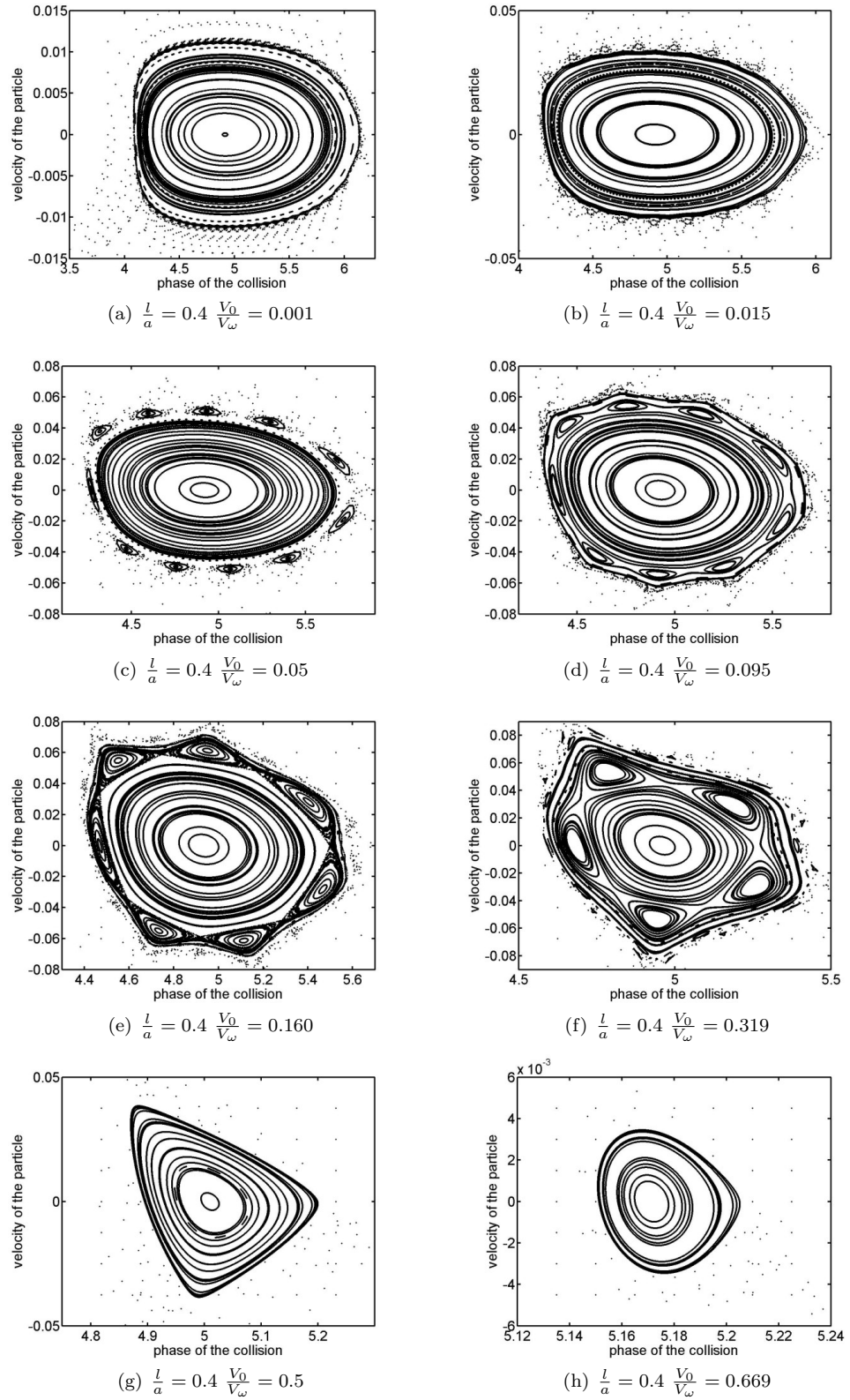
Figure 3.11:

3.5   Volume of the stable region
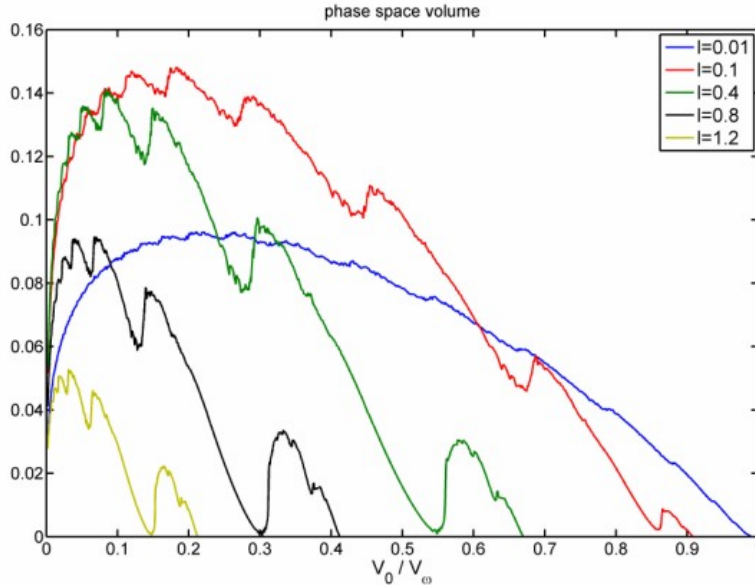
Figure 3.12: Phase space volume of the stable island for different parameters

We calculate numerically the surface covered by the bound orbits as a function of the parameters by dividing the phase space of the Poincaré sections into a fine grid of 10^6 small squares. All squares containing data points of the Poincaré section are added to the calculated surface. We checked this method for its stability by doubling the number of data points and compared the resulting surface. The resulting volume is shown in Fig. 3.12 as a function of the barrier's height $\frac{V_0}{V_\omega}$ for different values of the barrier's width $\frac{l}{a_0}$. The functions show a number of maxima at which a chain of sub-islands breaks away from the central fixed point. As in section 3.4 the barrier's width $\frac{l}{a_0}$ only changes the scale of the functions' dependence on $\frac{V_0}{V_\omega}$ but does not lead to unique dynamics. In the limit of very small $\frac{l}{a_0}$, the entire sequence of sub-structures is shifted to $\frac{V_0}{V_\omega} = 1$.
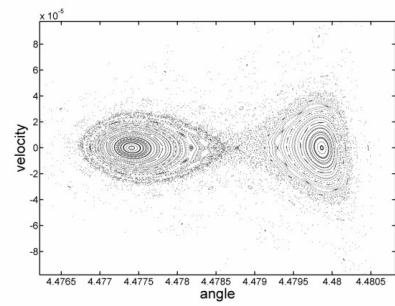
3.6   Fractal structure

The central elliptic points are surrounded by quasi-periodic and periodic orbits. When the system's parameters are changed these orbits can become unstable and they dissolve into chains of elliptic and hyperbolic fixed points, in accordance to the KAM theorem. These fixed points are again surrounded by quasi-periodic orbits which form sub-islands. Those sub-orbits dissolve into substructures themselves. This pattern exists on all scales of the phase space, forming a fractal structure. The following plots in Fig. 3.13 illustrate this for $\frac{V_0}{v_\omega} = 1.625$ and $\frac{l}{a_0} = 0.1$. The first plot shows the entire stable structure. The
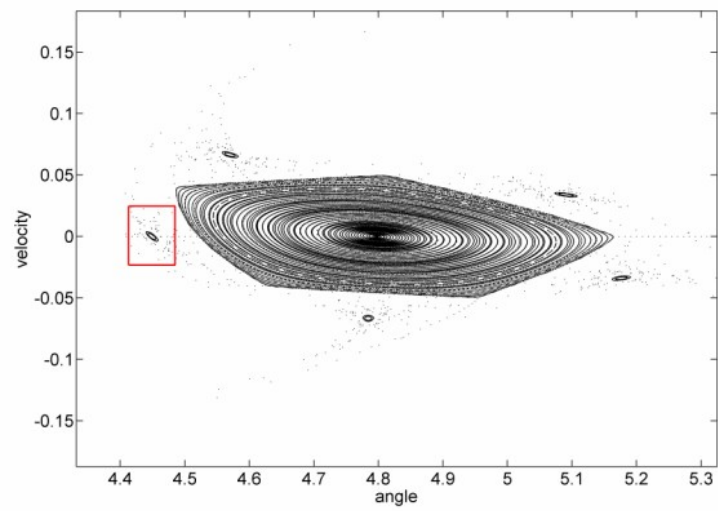
(a)
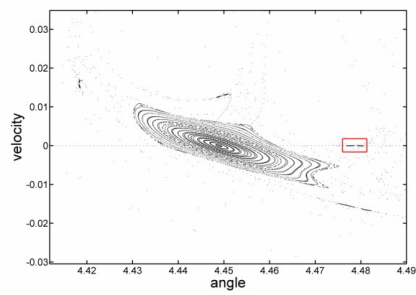
(b)

(c)

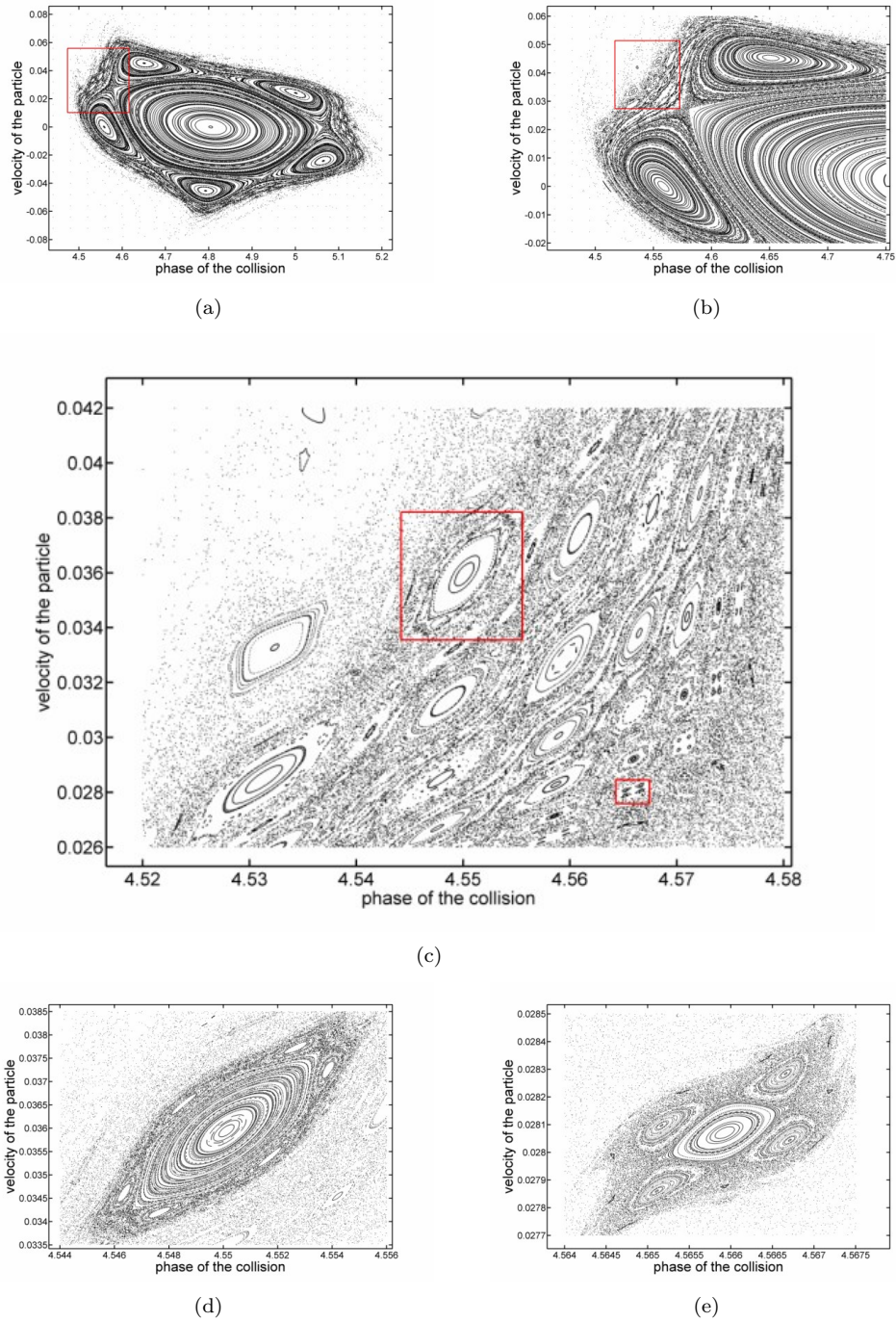Figure 3.13: Fractal structure of a sub-island

(a)

(b)

(c)

(d)

(e)

Figure 3.14: Fractal structure in the frontier of the stable island

following images are enlargements of the space marked by the red square in the preceding figure. Technically, this figures are not simple magnifications. They are actually new Poincaré sections with identical parameters. We placed the initial ensemble into the marked red squares to produce the desired resolution in this area.

The elliptic point at the center of the substructures belongs to a *periodic* orbit. This means that the trajectory closes after a finite number of collisions. The period can be read directly from the Poincaré section by taking the period visible in the plot by four. The period of the secondary fixed point in Fig.3.13 is 20. Fig. 3.14 shows an enlargement of the border region between the regular orbits and the chaotic layer for $\frac{V_0}{V_\omega} = 0.32$ and $\frac{l}{a_0} = 0.4$.

3.7 Fixed points of higher period

In section 3.3 we calculated the position of the central elliptic fixed point. This point is in fact not a fixed point of the mapping M but rather a periodic point of period 4, i.e. a fixed point of M^4. In section 3.4 we showed that this elliptic point is surrounded by sets of sub-islands. These sub-islands have stable periodic points at their center. The existence of these fixed points of higher period is a direct consequence of the Poincaré-Birkhoff theorem. As the parameters change, orbits become unstable and dissolve into chains of fixed points that are alternatingly stable (elliptic) and unstable (hyperbolic). The stable fixed points are visible in the Poincaré sections because they are surrounded by an island of bound orbits whereas the unstable fixed points would only be detected if one of the initial conditions used to generate the plot was exactly identical to such a point. The periodic orbits, which are the fixed points of the mapping and become visible as elliptic or hyperbolic points in the Poincaré section, form a fractal structure that has been analyzed in section 3.6. To understand this structure it is important to locate the fixed points of higher periods. Many chaotic processes are determined by the structure of the stable and especially the unstable periodic orbits (UPO).

In Ref. [1] and Ref. [15] Schmelcher and Diakonos have developed a method to detect the unstable periodic orbits of chaotic systems. Given a N-dimensional discrete chaotic dynamical system U defined by

$$U : \vec{r}_{i+1} = \vec{f}(\vec{r}_i) \tag{3.4}$$

they used a linear transformation to construct a new system S_k defined as

$$S_k : \vec{r}_{i+1} = \vec{r}_i + \mathbf{\Lambda}_k(\vec{f}^p(\vec{r}_i) - \vec{r}_i) \tag{3.5}$$

where $\mathbf{\Lambda}_k$ is an invertible $N \times N$ constant matrix and p is the period of the fixed point. Evidently, S_k and $\vec{f}^p$ have the same fixed points. The matrix $\mathbf{\Lambda}_k$ has to be chosen in a way that the unstable fixed points of $\vec{f}^k$ become stable under S_k. Since U will in general posses a set of different types of unstable periodic orbits one has to find a corresponding set of matrices $\mathbf{\Lambda}_k$ that does not depend on the period p. It has been shown that such a set of matrices always exists and that the correct choice is

$$\mathbf{\Lambda}_k = \lambda \mathbf{C}_k \tag{3.6}$$

where the $\mathbf{C}_k$ are orthogonal and correspond to reflections along the coordinate axes. Thus all entries of $\mathbf{C}_k$ are $C_{ij} \in \{0, \pm 1\}$ and each row and column contains only one element which is different form zero. There exists a total number of $N!2^N$ of such matrices. However it can be shown that a much smaller number of $\mathbf{C}_k$ is sufficient to find all periodic orbits because some of the matrices are redundant. The factor λ has to be small enough that the eigenvalues of the matrix $\mathbf{1} + \lambda \mathbf{C}_k(\mathbf{T}_U - \mathbf{1})$ have absolute values smaller than 1, where $\mathbf{T}_U$ is the stability matrix of the system U.

(a)   (b)
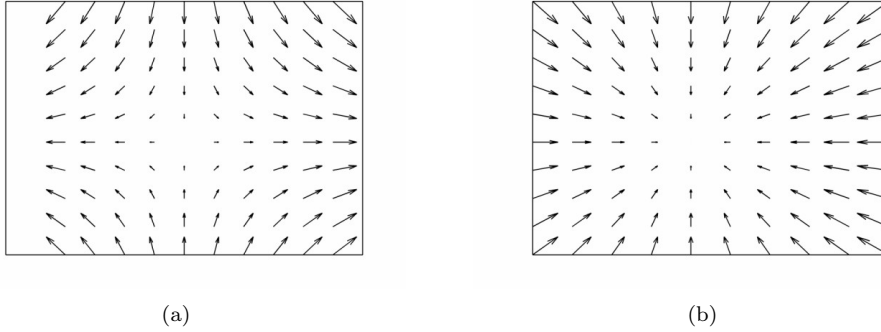
Figure 3.15: The vector field around an UPO before and after applying $\mathbf{C}_k$

This method has a nice geometrical interpretation: $\vec{f}^p(\vec{r}_i) - \vec{r}_i$ defines the vector field of the map's flow. In the neighborhood of a hyperbolic fixed point this vector field would typically look like in Fig. 3.15(a) for dimension N=2. The matrix $\mathbf{C}$ to stabilize this flow is

$$\mathbf{C} = \begin{pmatrix} -1 & 0 \\ 0 & 1 \end{pmatrix}$$

and the resulting phase flow is shown in Fig. 3.15(b). Thus the mapping S_k can simply be interpreted as following the vector field transformed by the reflection $\mathbf{C}_k$ with a step size of λ. The advantages of this method are twofold:

- The stabilization of the fixed points is global, therefore even initial conditions starting from far away will converge.

- The used matrix $\mathbf{C}_k$ offers the possibility to distinguish between the different types of fixed points.

The disadvantage of this method is its only linear convergence. Therefore, it makes sense to combine the transformed map with a standard root finding method, the Newton-Raphson algorithm. The fixed point equation $\vec{r}_i = \vec{f}^p(\vec{r}_i)$ can be transformed into a root finding problem:

$$\vec{g}(\vec{r}_i) := \vec{f}^p(\vec{r}_i) - \vec{r}_i = 0 \tag{3.7}$$

The Newton-Raphson iteration is defined by:

$$\vec{r}_{i+1} = \vec{r}_i - \mathbf{J}(\vec{r}_i)^{-1} \cdot \vec{g}(\vec{r}_i) \tag{3.8}$$

where **J** is the Jacobi matrix of $\vec{g}(\vec{r_i})$. The convergence of the Newton-Raphson algorithm is quadratic, but its convergence radius is limited and can be extremely small. We use the transformed map to find the approximate position of periodic orbits and then the Newton-Raphson algorithm with this approximate position as starting point to find the exact position.

In the system of the driven barrier we search for periodic orbits in the Poincaré sections. To make the section unique the mapping is constrained to collisions with the left edge of the barrier. This way each point in the (v, φ)-plane is uniquely connected to a point in the (x, v, t) phase space. Furthermore we constrict the Poincaré section to phases greater than π, since the structures of the stable orbits are anyway symmetric due to the driving law. These restrictions reduce the Poincaré section to the fourth island in Fig. 3.1. To find the periodic orbits we cover the (v, φ)-plane with a grid of 10^4 initial conditions. The parameter λ is chosen between $5 \cdot 10^{-3}$ and smaller values for higher periods. The used transformation matrices are:

$$\mathbf{C}_1 = \begin{pmatrix} 1 & 0 \\ 0 & 1 \end{pmatrix} \qquad \mathbf{C}_2 = \begin{pmatrix} -1 & 0 \\ 0 & 1 \end{pmatrix} \qquad \mathbf{C}_3 = \begin{pmatrix} 1 & 0 \\ 0 & -1 \end{pmatrix} \tag{3.9}$$

$$\mathbf{C}_4 = \begin{pmatrix} 0 & -1 \\ -1 & 0 \end{pmatrix} \qquad \mathbf{C}_5 = \begin{pmatrix} 0 & 1 \\ 1 & 0 \end{pmatrix} \tag{3.10}$$

It can be shown that it is possible to use a smaller set of matrices. We calculate the Jacobian matrix for the Newton-Raphson method numerically by using a two-point formula to determine the partial derivatives. This way we search for periodic orbits of period one up to 16. (This is the period in the reduced Poincaré section. The actual period is four times this period.) The results are shown in Fig. 3.16, Fig. 3.17, Fig. 3.18, Fig. 3.19, Fig. 3.20 and Fig. 3.21 for different parameters of the system. The periodic orbits of period 1 to 16 are shown as blue crosses for stable fixed points and red crosses for unstable fixed points. The corresponding Poincaré sections are also plotted in the same figures in black. As expected, the layer of sub-islands around the central island contains many families of periodic orbits which form the skeleton of the fractal structure. Most of the periodic orbits we find are unstable, but there are usually also some stable periodic orbits amongst them which belong to elliptic sub-islands. (The sub-islands are not necessarily visible in the plots, because we use only relatively few initial conditions to produce these Poincaré sections.) Fig. 3.22 shows an enlargement of Fig. 3.16 and illustrates this point. In fact, we plot in Fig. 3.22 periodic orbits up to a period of 40 and it is clear from this figure that there are plenty more periodic orbits of higher periods in this region. The number and density of periodic orbits generally rises exponentially with their period. In section 3.3 we calculated that the central periodic orbit of period 4 exists only for some range of parameters. Here we find that there also exist no other periodic orbits outside of this range.

The green lines in the figures 3.16, 3.17 and 3.21 are families of stable periodic orbits. They belong to a dense set of periodic orbits of period 15 in Fig. 3.16, 11 in Fig. 3.17 and again 15 in Fig. 3.21. The existence of such sets is also a direct consequence of the KAM theorem: Because each regular orbit is determined by the conservation of a first integral of motion **I**, such a conserved quantity must also exist for the stable periodic orbits. Since these orbits are situated in an entirely regular neighborhood, which the stable periodic orbits forming the elliptic sub-island do not, they are densely embedded
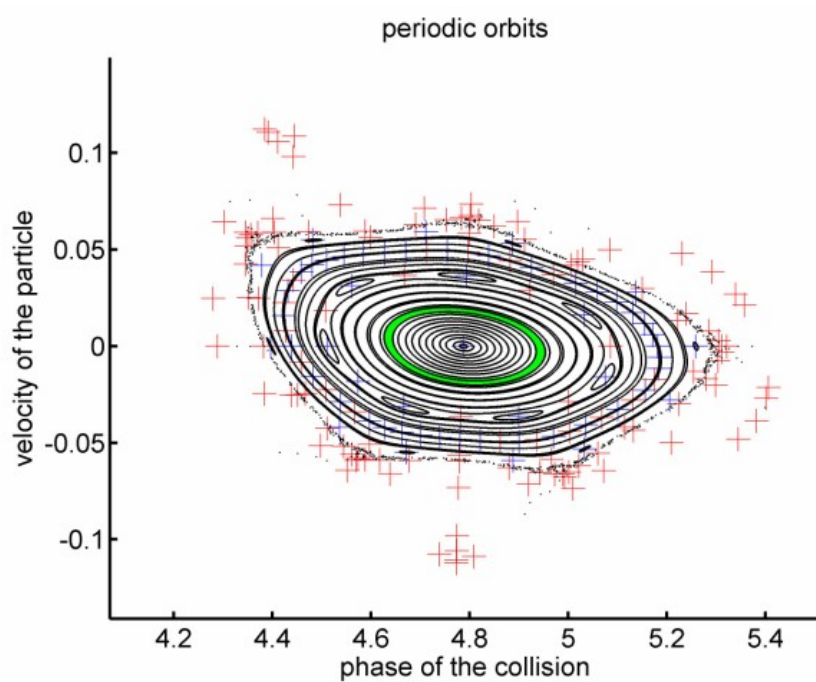
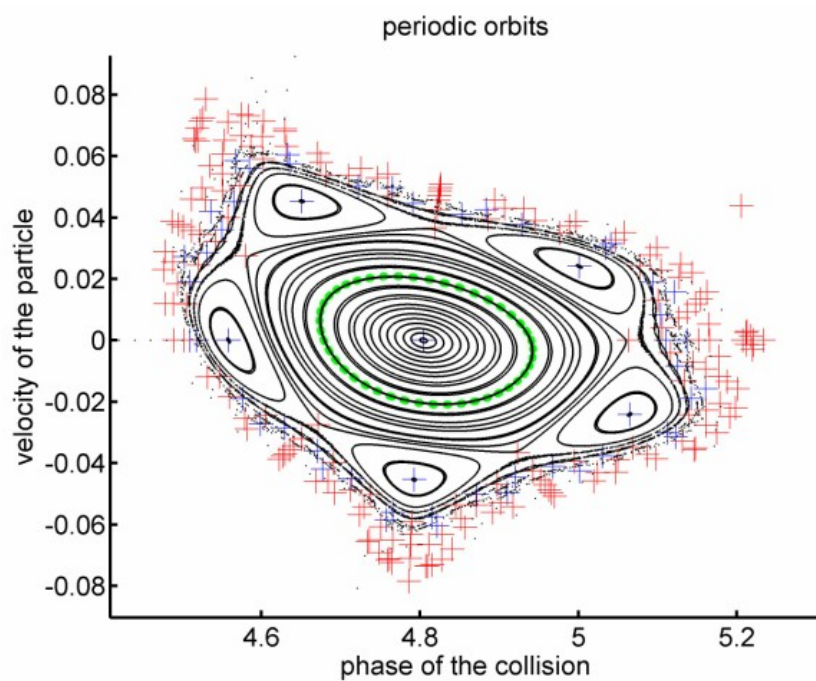Figure 3.16: Poincaré section and UPOs for $\frac{V_0}{V_\omega} = 0.55$ $\frac{l}{a_0} = 0.1$

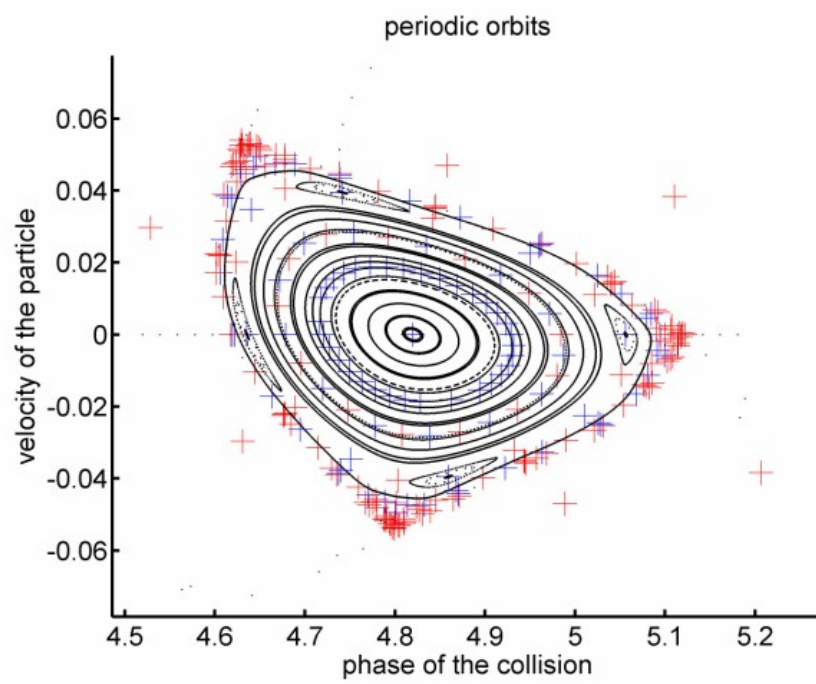Figure 3.17: Poincaré section and UPOs for $\frac{V_0}{V_\omega} = 0.7$ $\frac{l}{a_0} = 0.1$

Figure 3.18: Poincaré section and UPOs for $\frac{V_0}{V_\omega} = 0.775$ $\frac{l}{a_0} = 0.1$
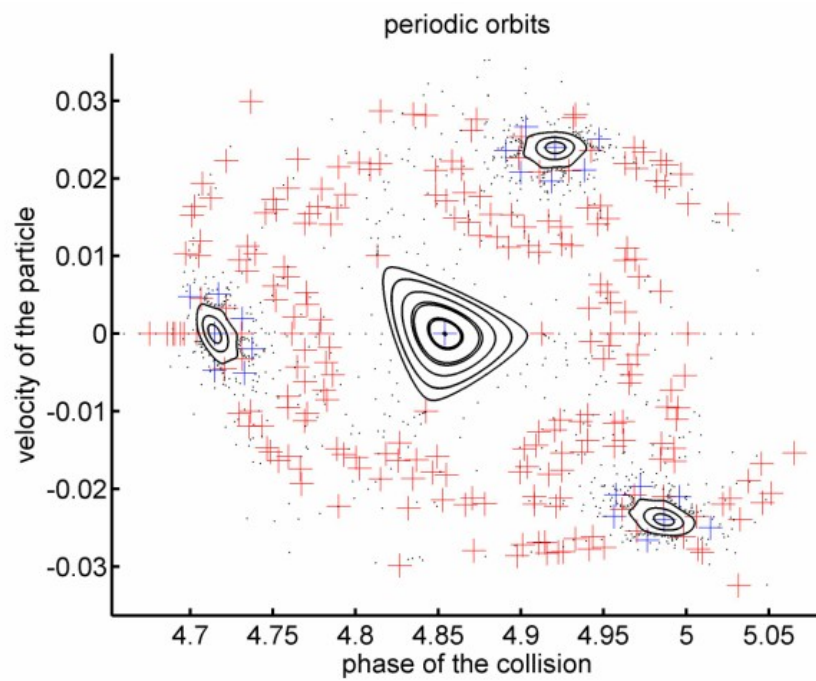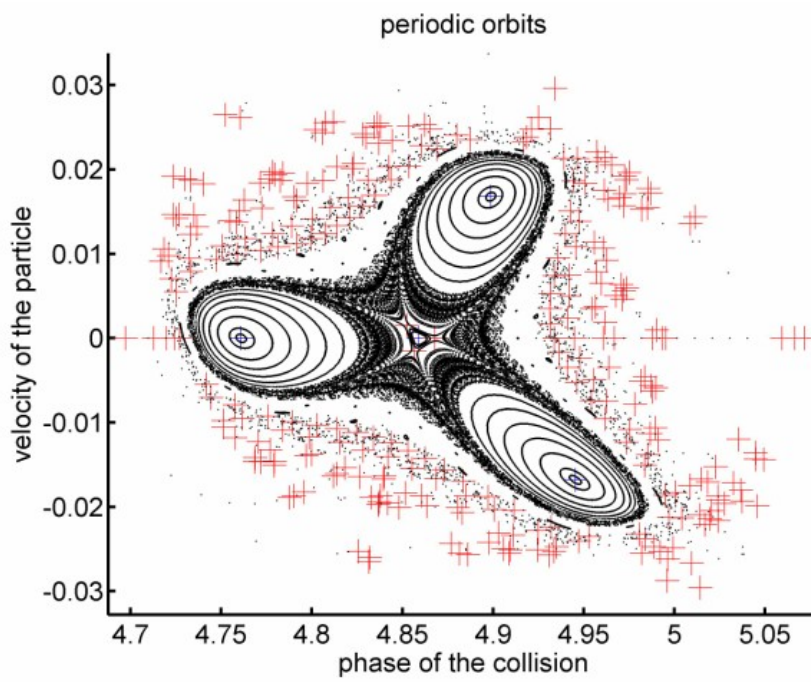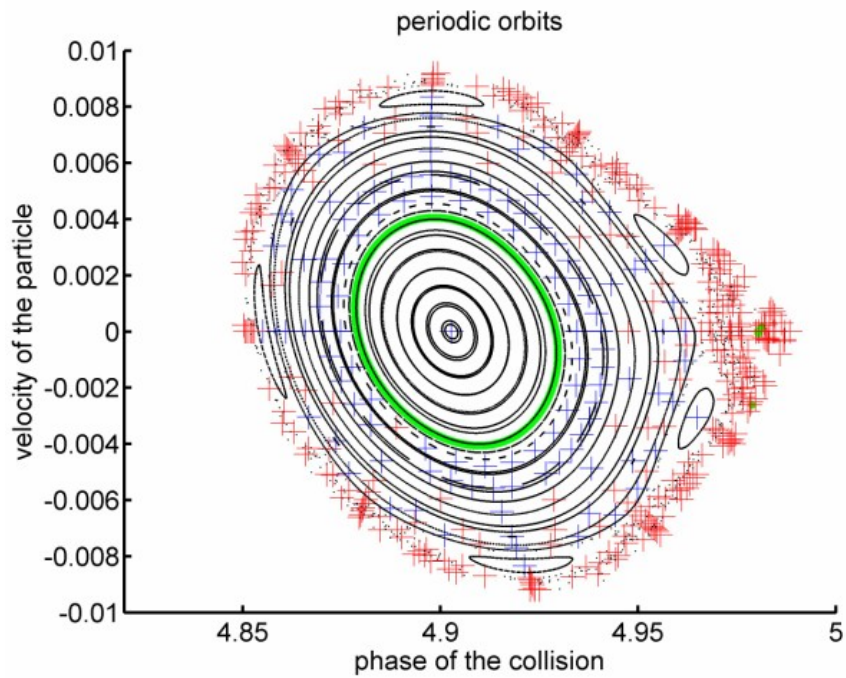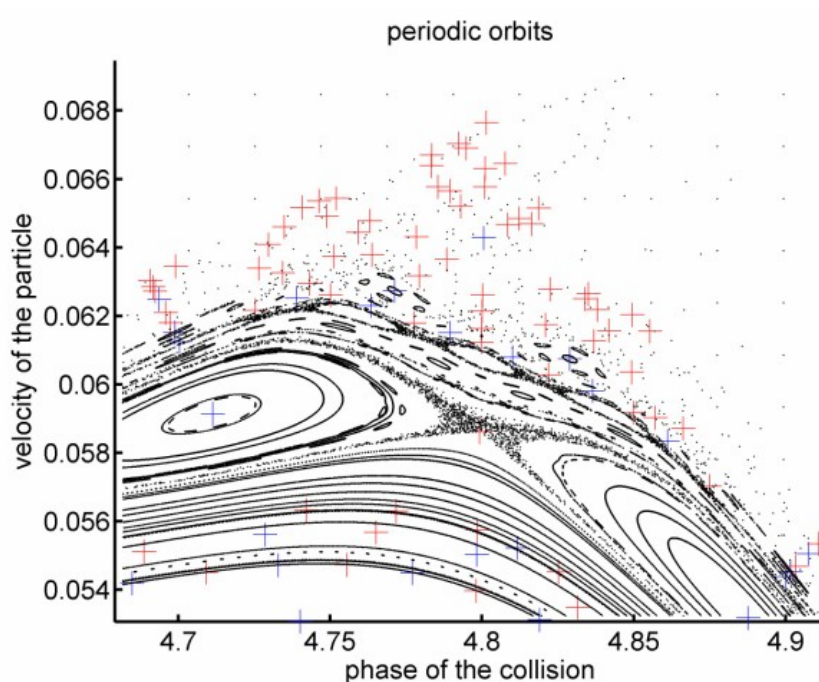

Figure 3.19: Poincaré section and UPOs for $\frac{V_0}{V_\omega} = 0.86$ $\frac{l}{a_0} = 0.1$

Figure 3.20: Poincaré section and UPOs for $\frac{V_0}{V_\omega} = 0.867$ $\frac{l}{a_0} = 0.1$

Figure 3.21: Poincaré section and UPOs for $\frac{V_0}{V_\omega} = 0.9014$ $\frac{l}{a_0} = 0.1$

Figure 3.22: Poincaré section and UPOs for $\frac{V_0}{V_\omega} = 0.53$ $\frac{l}{a_0} = 0.1$

between stable quasi-periodic orbits with infinitesimally different values of the conserved quantity $\mathbf{I} + \delta\mathbf{I}$ on one side and $\mathbf{I} - \delta\mathbf{I}$ on the other. Because the periodic orbit itself is stable, there must be an entire torus of periodic orbits with conserved quantity $\mathbf{I}$ between the quasi-periodic orbits. Therefore, each starting point of the algorithm converges to an arbitrary point in this curve. To test this interpretation I repeated the analysis for $\frac{V_0}{V_\omega} = 0.7$ and $\frac{l}{a_0} = 0.1$ with 10^6 initial conditions instead of 10^4 and the algorithm found 973214 different stable periodic orbits on this line.

3.8 Linearisation of the mapping

For many purposes it is useful to have an analytic approximation of the mapping defined in subsection 2.1.2. This can be done in the neighborhood of a periodic orbit by calculating the Jacobian matrix for the variables of the Poincaré section. Since the mapping anyway operates only on the Poincaré surface defined in section 3.1 we only linearize the mapping around these points. This simplifies the calculation because it reduces the dimension of the mapping to two, the velocity v and the phase of the collision $\varphi = t \mod 2\pi$. In the following I will use the normalized coordinates defined in section 2.2. Quasi-periodic orbits and orbits close to them are never reflected by the barrier and thus the mapping for the velocity is:

$$v_{n+1} = v_{barrier} + \text{sign}(v_n - v_{barrier})\sqrt{(v_n - v_{barrier})^2 \pm \frac{V_0}{V_\omega}} \qquad (3.11)$$

The phase is determined by an implicit equation

$$x_{n+1} = x_n + v_n(\varphi_{n+1} - \varphi_n) \tag{3.12}$$

where the position x_i is always equal to the barrier's position, $x_b(\varphi_i) = \cos(\varphi_i)$ or $x_b(\varphi_i) = \cos(\varphi_i) + \frac{l}{a_0}$, depending on which edge the particle collides with, and $v_b = -\sin(\varphi)$ is the barrier's velocity. The second phase φ_{n+1} is assumed to be always greater then the first phase φ_n. (Else, the term $\varphi_{n+1} - \varphi_n$ has to be replaced by $\varphi_{n+1} - \varphi_n + 2\pi$.) The sign under the square root in equation (3.11) is negative when the particle enters the barrier and it is positive when it leaves the barrier. The Jacobian matrix is defined as:

$$\mathbf{J} = \begin{pmatrix} \frac{\partial \varphi_{n+1}}{\partial \varphi_n} & \frac{\partial \varphi_{n+1}}{\partial v_n} \\ \frac{\partial v_{n+1}}{\partial \varphi_n} & \frac{\partial v_{n+1}}{\partial v_n} \end{pmatrix} \tag{3.13}$$

The partial derivatives of φ_{n+1} can be calculated from equation (3.12) by using the theorem for implicit functions:

$$f = x_{n+1} - x_n - v_n(\varphi_{n+1} - \varphi_n) = 0 \tag{3.14}$$

$$\Rightarrow \frac{\partial \varphi_{n+1}}{\partial \varphi_n} = -\frac{\frac{\partial f}{\partial \varphi_n}}{\frac{\partial f}{\partial \varphi_{n+1}}} \tag{3.15}$$

$$= \frac{\sin(\varphi_n) + v_n}{\sin(\varphi_{n+1}) + v_n} \tag{3.16}$$

$$\Rightarrow \frac{\partial \varphi_{n+1}}{\partial v_n} = -\frac{\frac{\partial f}{\partial v_n}}{\frac{\partial f}{\partial \varphi_{n+1}}} \tag{3.17}$$

$$= \frac{\varphi_n - \varphi_{n+1}}{\sin(\varphi_{n+1}) + v_n} \tag{3.18}$$

To calculate the derivatives of v_{n+1} we make use of the fact that $\varphi_{n+1}(\varphi_n, v_n)$ is a function of φ_n and v_n itself.

$$\frac{\partial v_{n+1}}{\partial \varphi_n} = \frac{\partial \varphi_{n+1}}{\partial \varphi_n} \cos(\varphi_{n+1}) \left(\text{sign}(v_n + \sin(\varphi_{n+1})) \frac{v_n + \sin(\varphi_{n+1})}{\sqrt{(v_n + \sin(\varphi_{n+1}))^2 \pm \frac{V_0}{V_\omega}}} - 1 \right) \tag{3.19}$$

$$\frac{\partial v_{n+1}}{\partial v_n} = -\cos(\varphi_{n+1}) \frac{\partial \varphi_{n+1}}{\partial v_n} + \text{sign}(v_n + \sin(\varphi_{n+1}))$$
$$\cdot \frac{(v_n + \sin(\varphi_{n+1})) \left(1 + \cos(\varphi_{n+1}) \frac{\partial \varphi_{n+1}}{\partial v_n} \right)}{\sqrt{(v_n + \sin(\varphi_{n+1}))^2 \pm \frac{V_0}{V_\omega}}} \tag{3.20}$$

To find the linearisation of a periodic orbit of period p we simply calculate the Jacobian matrix of each step and multiply the resulting matrices. We also calculated the Jacobian matrix numerically and found the result in very good agreement with the analytical calculation. The linearisation is interesting for us because it allows conclusions about the stability properties of a periodic orbit. The eigenvalues of stable periodic orbits have absolute value of one and are

complex conjugate to each other. The eigenvalues of unstable periodic orbits are always real and only their product has to be one, because the mapping is area preserving and, therefore, the determinant of the Jacobian matrix is equal to 1. The eigenvectors of unstable periodic orbits point in the direction of the stable and unstable manifolds of the fixed point. We will use this property in section 3.9.

3.9 Flow of unstable periodic orbits

Each unstable periodic orbit (UPO) possesses stable and unstable manifolds in phase space which govern the flow into and out of the fixed point. In the 2D Poincaré section these manifolds become simple asymptotic curves. The stable manifolds are very important for the scattering on the driven barrier because the scattering process becomes chaotic at the intersections of the stable manifold and the manifold of initial conditions. (See section 4.2.) In order to calculate the flow of an unstable periodic orbit we take a small initial segment of length 10^{-8} along the eigenvectors of the UPO and iterate an ensemble of 10^6 initial conditions in this segment forward in time along the unstable asymptotic curves or backward in time along the stable asymptotic curves. To iterate a particle backwards in time we have to invert the mapping, which can in general be rather difficult in driven systems. In this system it is quite simple, though, because we only need to invert the velocities $v \to v' = -v$, which inverts the propagation of the particles, and change the direction of time in the driving law of the oscillating barrier. The time mapping defined in equation (2.10) then becomes:

$$a_0 \cos\left(\omega(t_n - t)\right) = x_n + v'_n \cdot t = x_n - v_n \cdot t \qquad (3.21)$$

The time of the next collision $t_{n+1} = t_n - t$ is now smaller then the starting time t_n. The interaction with the barrier at the collision point is automatically inverted by changing the sign of the velocity $v \to v' = -v$ because the interaction itself is time independent. This is clear because we used the conservation of energy to derive the interaction mapping in subsection 2.1.3. Changing the direction of time in the driving law and using negative time steps is numerically problematic though, because our algorithm is strictly built for a forward iteration. In this special case, however, this is not much of an issue since the driving law is harmonic and therefore symmetric:

$$\cos\left(\omega(t_n - t)\right) = \cos(2\pi + \omega(t - t_n)) \qquad (3.22)$$

This symmetry property reduces the change of sign to a simple phase shift:

$$t_n \to t_n + \Delta t = t_n - 2t_n = -t_n \qquad (3.23)$$

This additive phase shift of $\Delta t = -2t_n$ has to be undone after the backward iteration to compare the inverted trajectory with the original.

When the manifolds of different UPOs cross each other at heteroclinic intersections the flow of particles splits and becomes chaotic because the number of intersections diverges. Since we can only place our initial ensemble with a limited accuracy on the asymptotic curves and since the number of UPOs also diverges this effect is amplified. It is therefore in most cases not possible to follow the flow of a single specific UPO. Rather, these simulations produce a
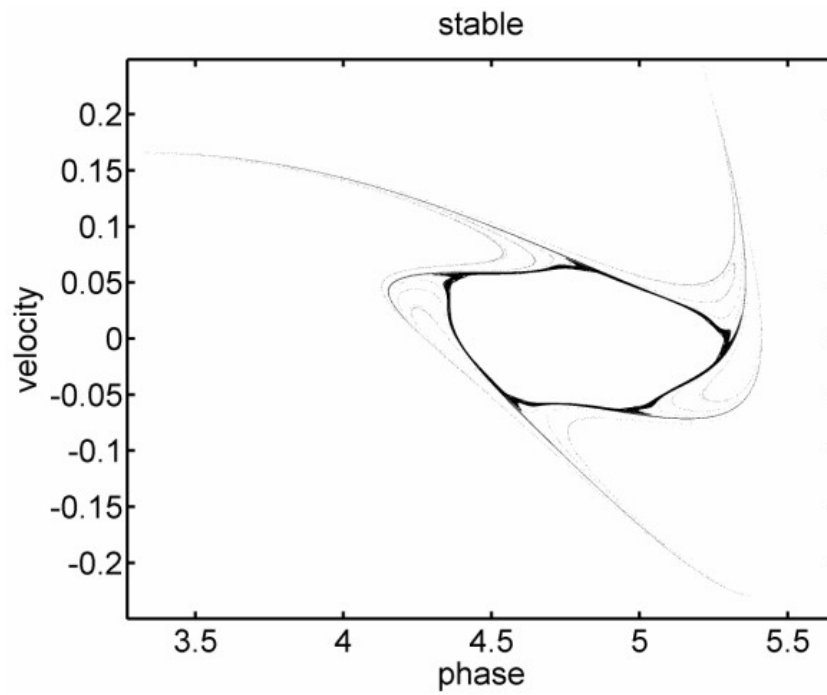
stable

Figure 3.23: Stable manifolds for $\frac{V_0}{V_\omega} = 0.55$ $\frac{l}{a_0} = 0.1$
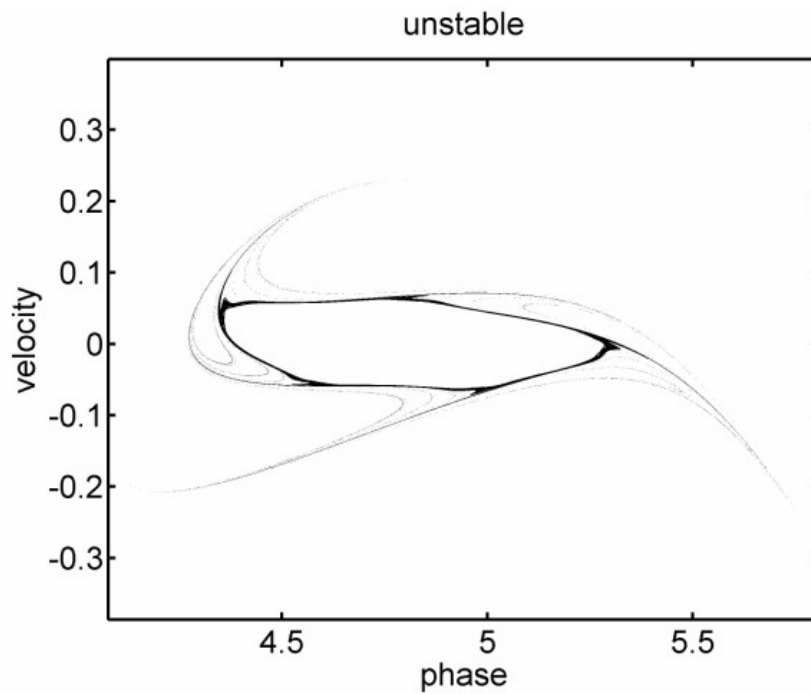
unstable

Figure 3.24: Unstable manifolds for $\frac{V_0}{V_\omega} = 0.55$ $\frac{l}{a_0} = 0.1$

global picture of the flow of the system of UPOs. We plotted the stable and unstable flow for $\frac{V_0}{V_\omega} = 0.55$ and $\frac{l}{a_0} = 0.1$ in Fig. 3.23 and 3.24 (the corresponding Poincaré section and UPOs are plotted in Fig. 3.16) and for $\frac{V_0}{V_\omega} = 0.70$ and $\frac{l}{a_0} = 0.1$ in Fig. 3.25 and 3.26 (the corresponding Poincaré section and UPOs are plotted in Fig. 3.17). The starting points of the iteration correspond to an UPO of period 5 (20) at $\varphi = 4.346$ and $v = 0.059$ in Fig. 3.23 and Fig. 3.24 and to an UPO of period (12) at $\varphi = 4.530$ and $v = 0.079$ in Fig. 3.25 and Fig. 3.26 (In fact, the periods are not 5 and 3 but 20 and 12 when we take into account that we have 4 identical structures in phase space that are all visited equally by the periodic orbits. In the following we will use the period which becomes visible in our plots. Please note that the actual period is 4 times that period.)
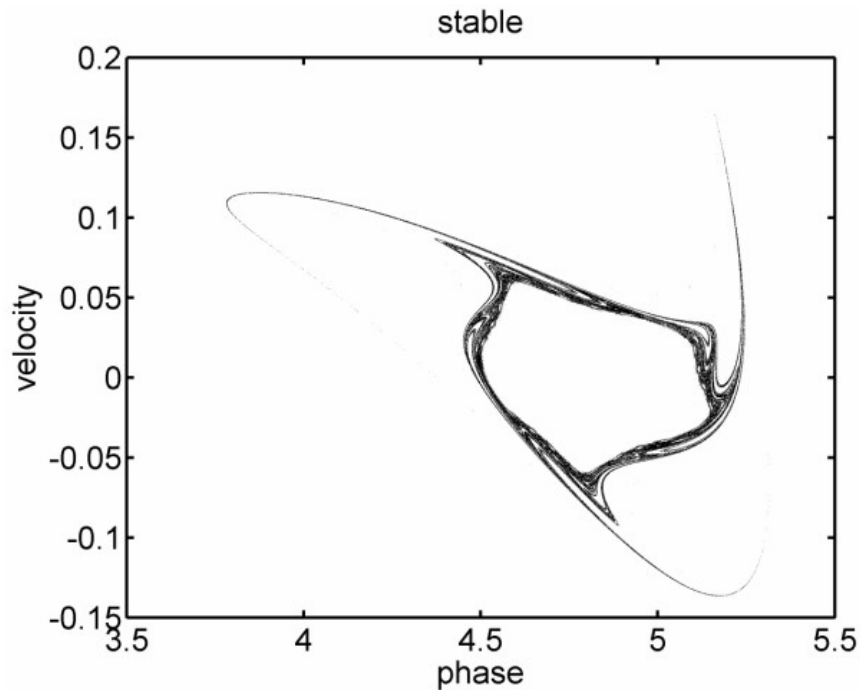
Figure 3.25: Stable manifolds for $\frac{V_0}{V_\omega} = 0.70$ $\frac{l}{a_0} = 0.1$

Fig. 3.27 shows an enlargement of the stable manifold of Fig. 3.25. As one can see, the flow forms complicated patterns in the border region of the stable island. This gives a glimpse of the complicated dynamics that the UPOs create in the chaotic region. Both stable and unstable manifolds reach far out of the border region into the chaotic sea in what looks in these plots as spiral arms, which consist of an infinite number of stable or unstable curves. The direction of curvature of these spirals is different because particles all "rotate" clockwise around the central fixed point and particles on the stable manifold move towards the center whereas particles on the unstable manifold move away from the center. These outer manifolds belong to unstable periodic orbits of period 5 in Fig. 3.23 and 3.24 and period 3 in Fig. 3.25 and 3.26. We found that the flow of *all* UPOs enters or leaves the neighborhood on these asymptotic curves. This means that far from the stable island the flow is dominated by just
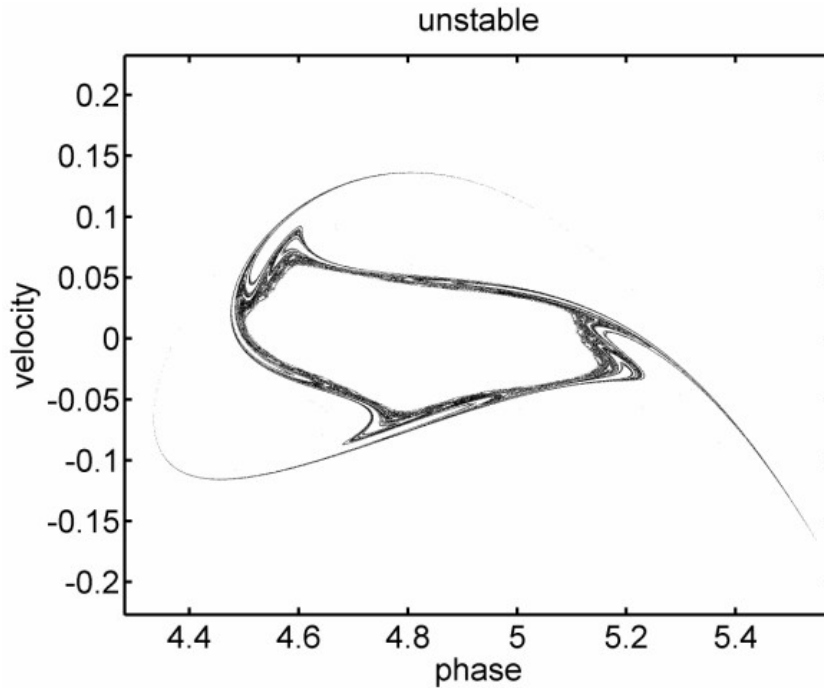
unstable

Figure 3.26: Unstable manifolds for $\frac{V_0}{V_\omega} = 0.70 \; \frac{l}{a_0} = 0.1$

one family of UPOs.

In section 3.4 we showed that the creation and destruction of sub-islands follows a typical sequence: As $\frac{V_0}{V_\omega}$ is decreased sub-islands move from the inside of the elliptic island to the outside and dissolve. When such a sub-island dissolves it leaves it's central UPO behind. Additionally, the sub-islands are surrounded by sub-sub-islands which also produce UPOs. Their respective periods are multiples of the period of the sub-island. In this way the dissolved sub-island produces an infinite set of UPOs which lies at the outer edge of the stable island. Only the flow of this set extends into the chaotic sea. In the cases we have shown here the sequence is as following:

Starting from $\frac{V_0}{V_\omega} = 0.86$ in Fig. 3.19, where we can see sub-islands of period 3, we reduce the potential to $\frac{V_0}{V_\omega} = 0.70$ in Fig. 3.17 where this sub-island has dissolved but still dominates the flow shown in Fig. 3.25 and 3.26. When we decrease the potential further to $\frac{V_0}{V_\omega} = 0.55$ the sub-islands of period 5 in Fig. 3.17 dissolves and now determines the flow plotted in Fig. 3.23 and 3.24.
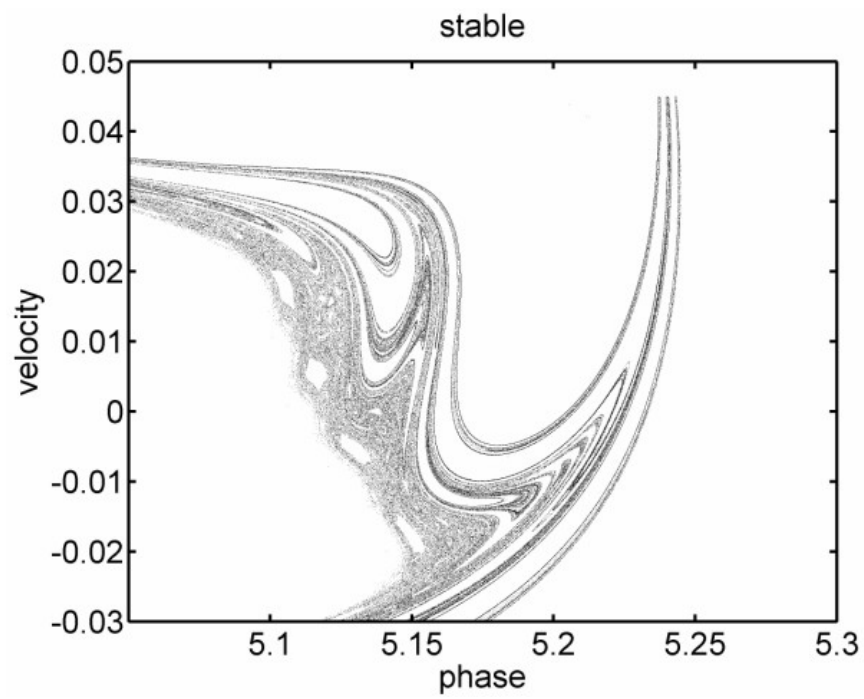
Figure 3.27: Enlargement of the stable manifolds for $\frac{V_0}{V_\omega} = 0.70$ $\frac{l}{a_0} = 0.1$

Chapter 4

Scattering

In chapter 3 we have investigated the quasi-periodic and periodic orbits of the system by using initial conditions inside the scattering zone. The other way of exploring the system's dynamics is to scatter particles on the barrier. By using particles starting far away from the barrier with a certain velocity we probe the transition zone around the stable island. The regular orbits themselves are not accessible by this approach, because the initial conditions outside the scattering region are not connected to the island of stability in phase space. Since trajectories don't intersect in phase space, the outermost invariant KAM curves form a barrier for particles outside this curve. The complex fractal structures of dissolved orbits and sub-islands surrounding the stable structure, however, are accessible from the outside. We examine in detail the dwelltime, defined as the time the particles are in the scattering region, and the change of the velocity of the particles. We also determine the particles' number of collisions and whether they are being transmitted through the scattering region or reflected back.

To simulate the scattering at the barrier we use a suitable ensemble of initial conditions and iterate the mapping until all particles have left the scattering region. Since the accessible phase space is entirely open all particles must eventually leave the scattering region. (The scattering region is defined as the space that is covered by the barrier's oscillation.) As initial conditions we take an ensemble uniformly distributed positive velocities. The initial position x_0 of all particles is far outside the scattering region at negative values and distributed in a way that the phases of the particles' first collisions is uniformly distributed in $[0, 2\pi]$. It makes sense to use the initial velocity and the phase of the first collision as parameters of the scattering because this allows easy comparisons to the Poincaré sections of chapter 3, where we use similar coordinates. Using the phase of the first collision as a coordinate has one disadvantage: At low initial velocities it is not possible to hit the barrier in all phases. A particle cannot, for example, hit the barrier at a phase at which the barrier moves away from it at a higher velocity. Thus, the following plots have an area marked as inaccessible. This means that the corresponding set of parameters (v_{in}, φ_c) is not accessible by initial conditions outside the scattering region.

Depending on the parameters and initial conditions we find that the single driven barrier exhibits regular scattering and chaotic scattering.

4.1   Regular Scattering

Fig. 4.1 shows the change of velocity of an incoming particle, defined as $|v_{in}| - |v_{out}|$, where v_{in} is the initial velocity and v_{out} is the final velocity, as a function of the initial velocity and the phase of the first collision. The parameters of the barrier are $\frac{2V_0}{m\omega^2 a_0^2} = 0.32$ and $\frac{l}{a_0} = 0.4$. (In detail: $a_0 = 1$, $\omega = 1$, $m = 1$, $l = 0.4$ and $V_0 = 0.16$.) We use a total of 10^6 initial conditions to generate this plot.
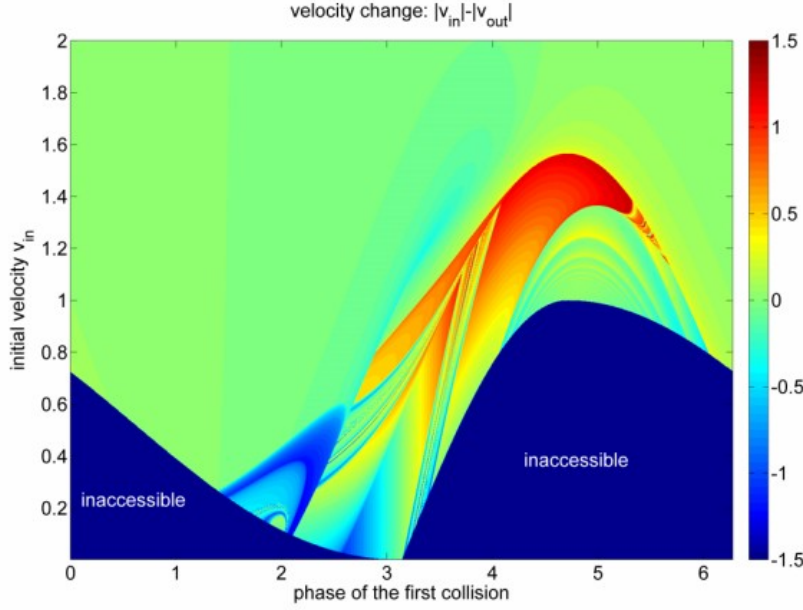
Figure 4.1: Scattering function for $\frac{l}{a_0} = 0.4$, $\frac{V_0}{V_\omega} = 0.32$. The colors represent the velocity change of the particle.

As this plot shows, the velocity of fast particles is hardly changed by the interaction with the barrier. This is exactly what has to be expected because fast particles will be transmitted into the barrier after the first collision and leave the scattering region after exactly two collisions, one with the left and one with the right edge of the barrier. The particle's velocity v_{n+2} after the collision with the right edge of the barrier can be calculated from its initial velocity v_n and the velocity v_{n+1} after the collision with the left edge:

$$v_{n+1} = v_b(t_{n+1}) + \sqrt{(v_n - v_b(t_{n+1}))^2 - \frac{2}{m}V_0} \tag{4.1}$$

$$v_{n+2} = v_b(t_{n+2}) + \sqrt{(v_{n+1} - v_b(t_{n+2}))^2 + \frac{2}{m}V_0} \tag{4.2}$$

$$= v_b(t_{n+2}) + \sqrt{\left(v_b(t_{n+1}) - v_b(t_{n+2}) + \sqrt{(v_n - v_b(t_{n+1}))^2 - \frac{2}{m}V_0}\right)^2 + \frac{2}{m}V_0} \tag{4.3}$$

If the particle is fast enough one can approximate $v_b(t_{n+1}) - v_b(t_{n+2}) \approx 0$. Thus
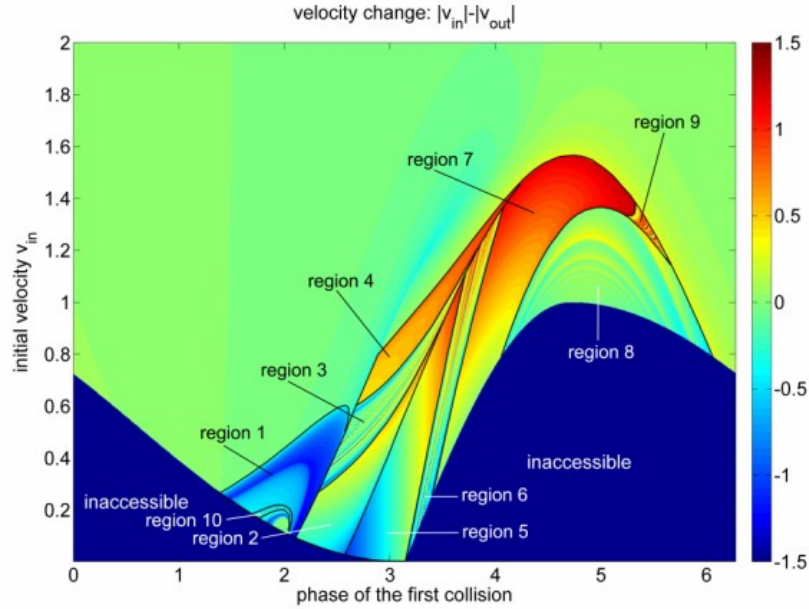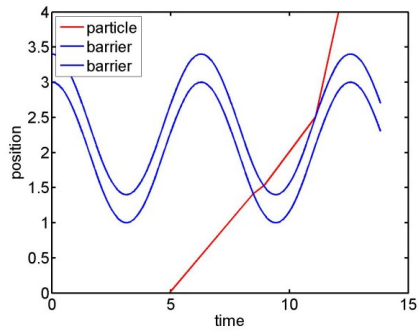
the equation above reduces to:

$$v_{n+2} \approx v_n$$

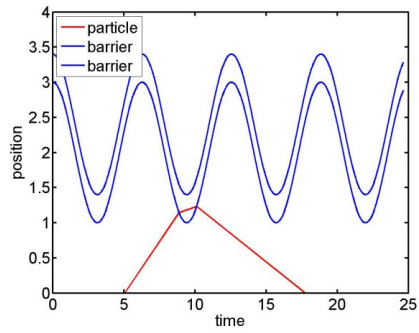Figure 4.2: Scattering function for $\frac{l}{a_0} = 0.4$, $\frac{V_0}{V_\omega} = 0.32$

The dynamics of slow particles are a lot more complicated: The parameter space between the inaccessible area and the high velocity part shows an elaborate structure that can be divided into characteristic regions, which are marked in Fig. 4.2. With the exception of the regions 3, 6, 9 and 10 the velocity change is a smooth function of the parameters within each region an it is discontinuous at their edges. This is called regular scattering. The fine structure of strokes in the regions 3, 6, 9 and 10 on the other hand is a signature of chaotic scattering. Chaotic scattering means that the scattering function has an infinite set of singularities forming a fractal structure. In section 4.2 we will show that in these regions the incoming trajectories enter the KAM structure of the phase space. These particles experience many collisions with the barrier, which is called stickiness, and as a consequence of the high collision number the dynamics of the sticky particles depends critically on the initial conditions. This way the fractal structure of the phase space creates a fractal structure in the scattering functions.

To explain the details of the scattering process we show a representative trajectory for each region of the scattering function in Fig. 4.3 and Fig. 4.4. In the following, we will describe the interaction with the barrier and compare it with the transmission function which is plotted in Fig. 4.5.
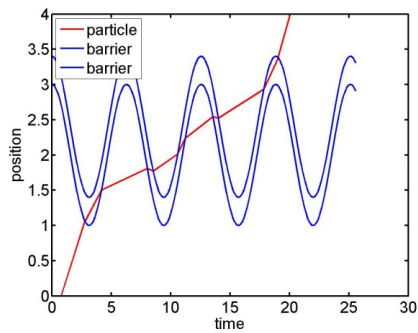
region 1: Fig. 4.3(a) Particles with initial conditions in the first region are similar to fast particles in that they are transmitted through the barrier.
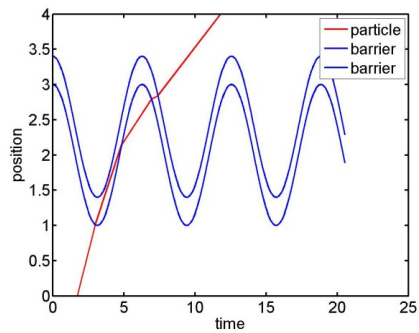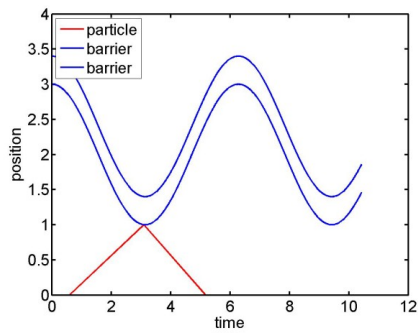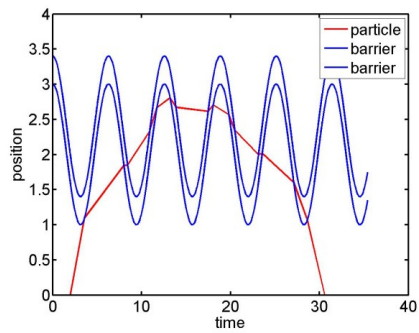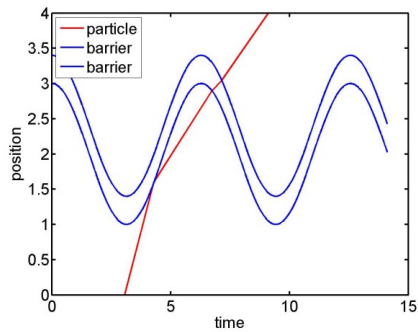
(a) region 1

(b) region 2

(c) region 3

(d) region 4

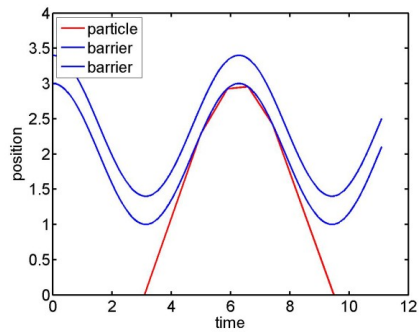(e) region 5

(f) region 6

(g) region 7

(h) region 8

Figure 4.3: Typical trajectories for each region

(a) region 9
(b) region 10

Figure 4.4: Typical trajectories for each region

The difference is that these particles are slow enough so that the barrier hits them again while they leave the scattering region. This third collision accelerates the particles.

region 2: Fig. 4.3(b) Particles in region 2 hit the barrier near its minimum position. They are transmitted into the barrier at the first collision but then are overtaken by the returning barrier and collide with the *same* edge of the barrier. This sequence of collisions gives the particles a negative velocity and they leave the scattering region in negative coordinate direction. Thus these particles are reflected back.

region 3: Fig. 4.3(c) Similar to the trajectories in region 2, these particles are transmitted into the barrier and then leave it on the same side again as the barrier overtakes them. However, their velocity after this collision becomes small and the particles collide with the barrier again. After this third collision the particles can exhibit any number of further collisions. This effect is called "stickiness" and leads to chaotic scattering. Therefore the scattering function is not smooth in this region. (See subsection 4.2.2)

region 4: Fig. 4.3(d) The dynamics in region 4 is similar to that in region 3 except that the particles are so fast after the first two collisions that they are transmitted through the barrier afterwards.

region 5: Fig. 4.3(e) These particles are simply reflected back by the barrier at the first collision.

region 6: Fig. 4.3(f) As in region 5, the particles in this region are reflected at their first collision. This first collision decelerates them and just like in region 3 the particles then experience many more collisions and exhibit "stickiness".

region 7: Fig. 4.3(g) After being reflected by the barrier at the first collision these particles are fast enough to be transmitted through the barrier at the next collision.

region 8: Fig. 4.3(h) The trajectories in this region form an arch following
   closely the shape of the barrier. This is called a "whispering gallery" orbit
   in static systems.

region 9: Fig. 4.4(a) The dynamics in this region is almost identical to the
   one in region 6.

region 10: Fig. 4.4(b) As in region 1, the particles are transmitted through
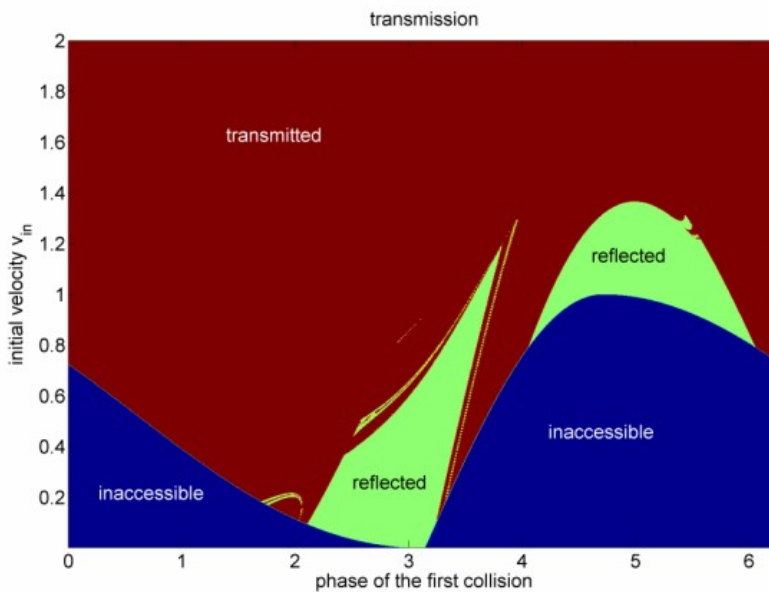   the barrier but then enter the border region of the stable orbits in phase
   space.

Figure 4.5: Transmission function for $\frac{l}{a_0} = 0.4$, $\frac{V_0}{V_\omega} = 0.32$

Another way of investigating the scattering process is to take a look at 2D
scattering functions. Fig. 4.6 shows a slice of Fig. 4.2 at $v_{in} = 1$. Some
representative initial conditions φ_0 have been marked as examples and their
trajectories have been examined further in Fig. 4.8. These plots not only illus-
trate the scattering process, but also explain the discontinuities of the scattering
function at the edges of the regular regions which are also visible in Fig. 4.6.
For example, at the collision phase of $\varphi_c = 3.335$ the acceleration of the particle
changes from $\Delta v = -0.15$ to $\Delta v = 0.9$ at $\varphi_c = 3.336$. Here, the dynamics
depends critically on the initial conditions. Fig. 4.8(d) and Fig. 4.8(e) show
this dependence directly: A minimal change in the slope or starting point of the
trajectory in Fig. 4.8(d) will lead to a second collision with the barrier's left
edge as in Fig. 4.8(e) and create completely different dynamics.

Around $\varphi_c = 3.561$ and $\varphi_c = 3.766$ the shape of the curve in Fig. 4.6 becomes
fractal (We will show in section 4.2 that this structure is indeed fractal). From
Fig. 4.8(g) one can see that at this initial phase the incoming trajectory has
many collisions with the barrier. Fig. 4.7 shows an enlargement by a factor of

10^4 of the fractal part of Fig. 4.6. This fractal structure can now be understood better: Each collision can depend critically on the initial conditions like in Fig. 4.8(d). For particles that collides many times with the barrier, each collision can produce an additional singularity. These discontinuities simply overlap and form a singularity. However, to form a singularity, particles must thus have an *arbitrary* large number of collisions. We will show this in section 4.2.
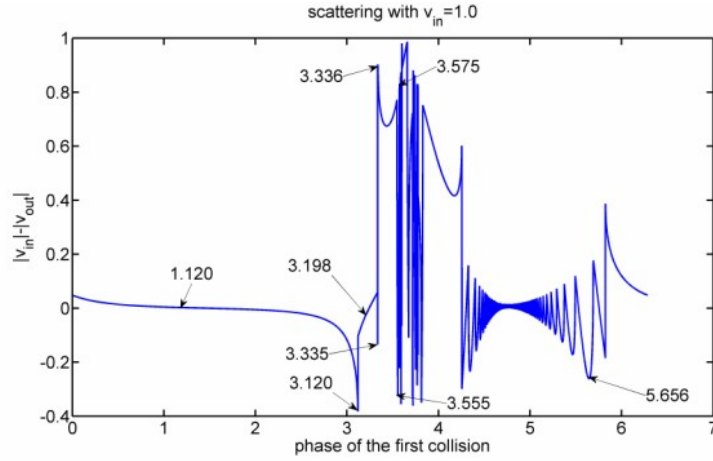

Figure 4.6: A cut through the scattering function in Fig. 4.1
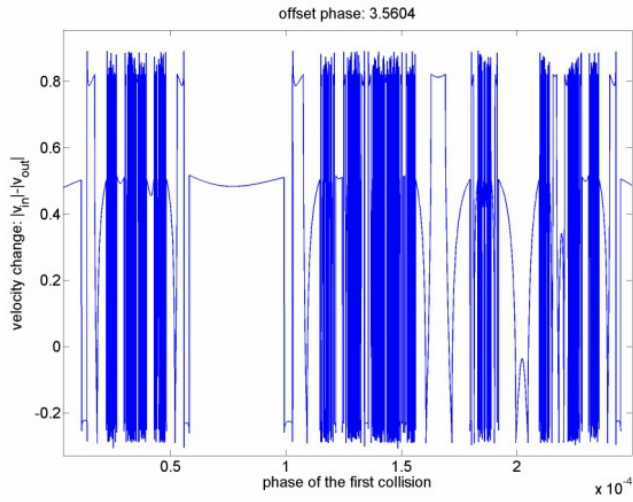
Figure 4.7: Enlargement of the cut in Fig. 4.6
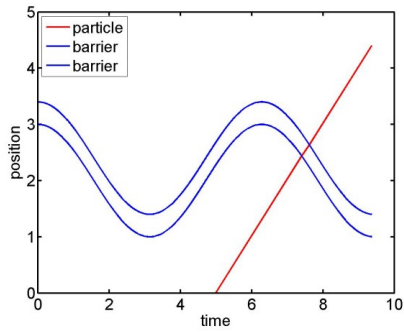
(a) $\varphi_0 = 1.120$
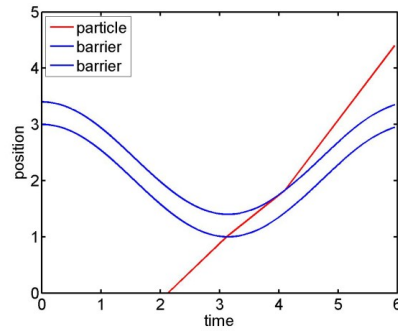
(b) $\varphi_0 = 3.120$
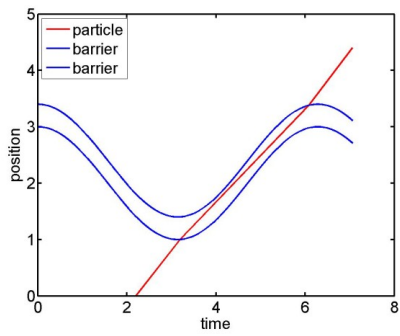
(c) $\varphi_0 = 3.198$
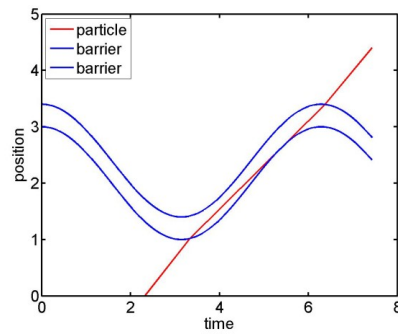
(d) $\varphi_0 = 3.335$
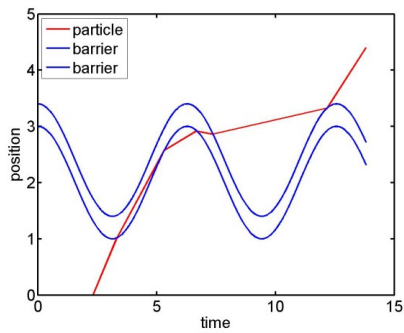
(e) $\varphi_0 = 3.336$
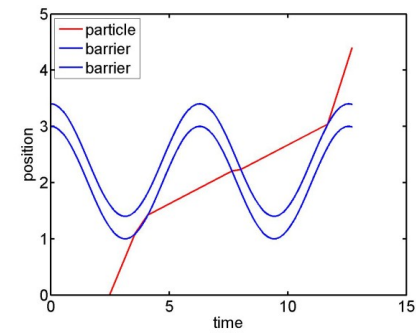
(f) $\varphi_0 = 3.555$
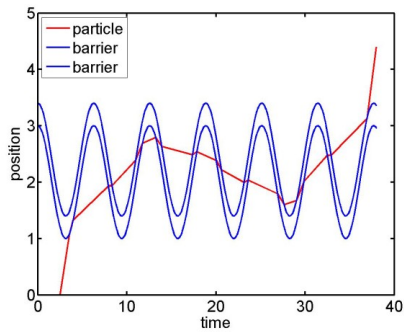
(g) $\varphi_0 = 3.575$
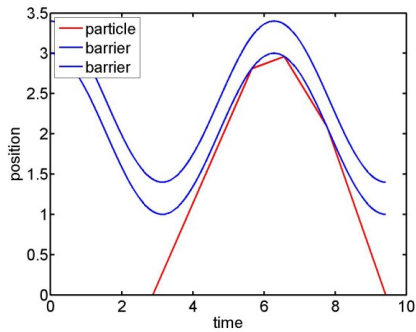
(h) $\varphi_0 = 5.656$

Figure 4.8: Typical trajectories

4.2 Chaotic scattering

In this chapter we will examine the chaotic scattering process in the regions 3, 6, 9 and 10. At first, we would like to give a brief definition of the terms chaotic scattering and the related term of a singularity of the scattering function:

***Def.:* singularity:** A value x_s is called a singularity of the scattering function f if for every $\varepsilon > 0$ and a fixed $K > 0$ there exists (at least) a pair of initial conditions $x_1, x_2 \in [x_s, x_s + \varepsilon] \vee x_1, x_2 \in [x_s - \varepsilon, x_s]$ such that $|f(x_1) - f(x_2)| > K$. This means that a plot of the scattering function always shows unresolved regions in any arbitrarily small interval around x_s because f fluctuates with an amplitude of at least K. It means that the scattering function is infinitely sensitive to the initial conditions around the singularity. An example is $\sin(\frac{1}{x})$ at $x_s = 0$.

***Def.:* chaotic scattering:** A scattering process is called chaotic if the set of singularities of it's scattering function is a fractal. Other definitions are stricter and require the set of singularities to be a Cantor set.

The scattering function in this work is of course the velocity change $|v_{incoming}| - |v_{out}|$. It has been shown in many systems that the singularities coincide with initial conditions that have an infinite time delay. This means the dwelltime, or, more general, the time the trajectories spend in the scattering region, diverges at the singularities. This is also the case in this system. (See subsection 4.2.1.)
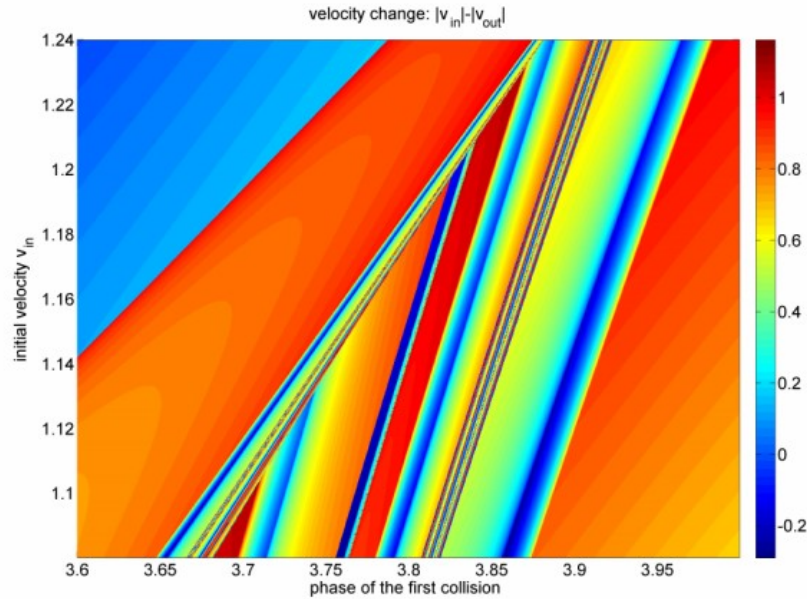

Figure 4.9: region 3 and 6

In the figures 4.9, 4.10 and 4.11 we plot enlargements of Fig. 4.1 showing the regions where the scattering becomes chaotic. These figures exhibit the typical signature of chaotic scattering in this system: The line-shaped discontinuities
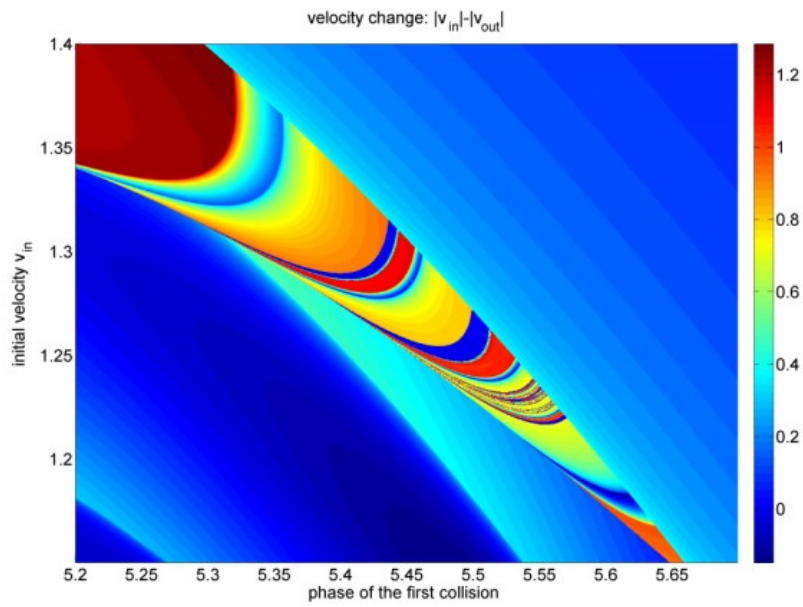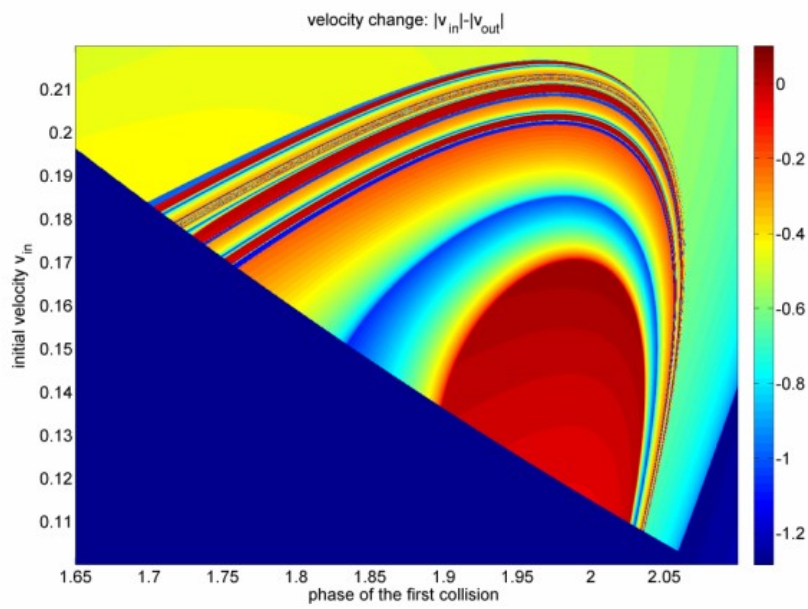
Figure 4.10: region 9

Figure 4.11: region 10

accumulate towards singularities. These singularities form thick unresolved layers, which are interspersed with smooth regular regions. (The parameters of the barrier are still $\frac{2V_0}{m\omega^2 a_0^2} = 0.32$ and $\frac{l}{a_0} = 0.4$.)
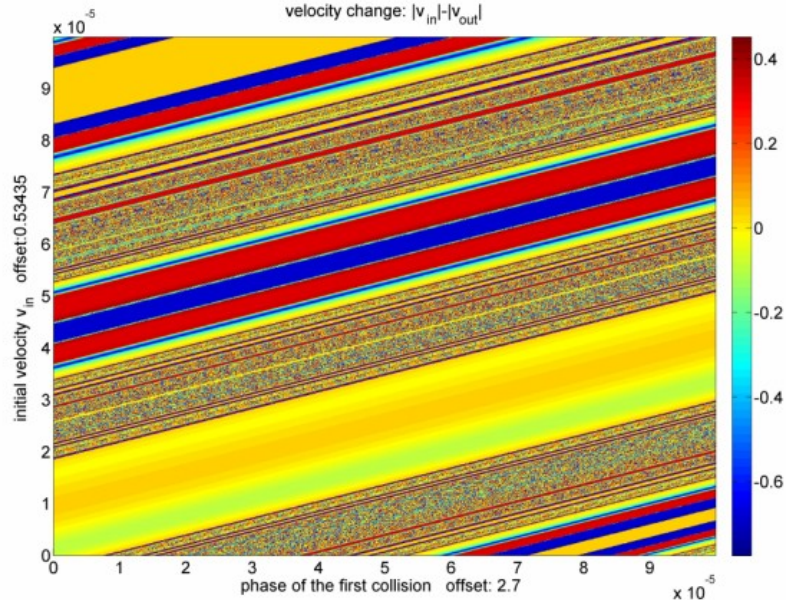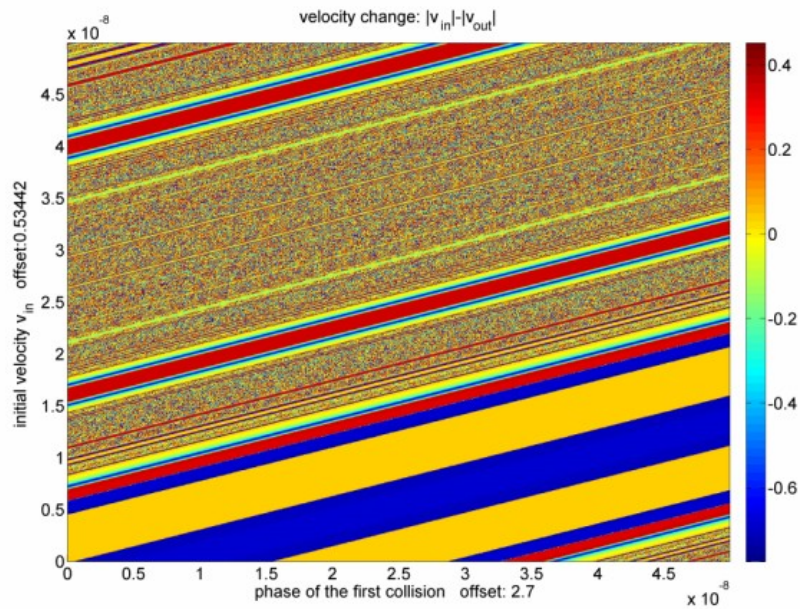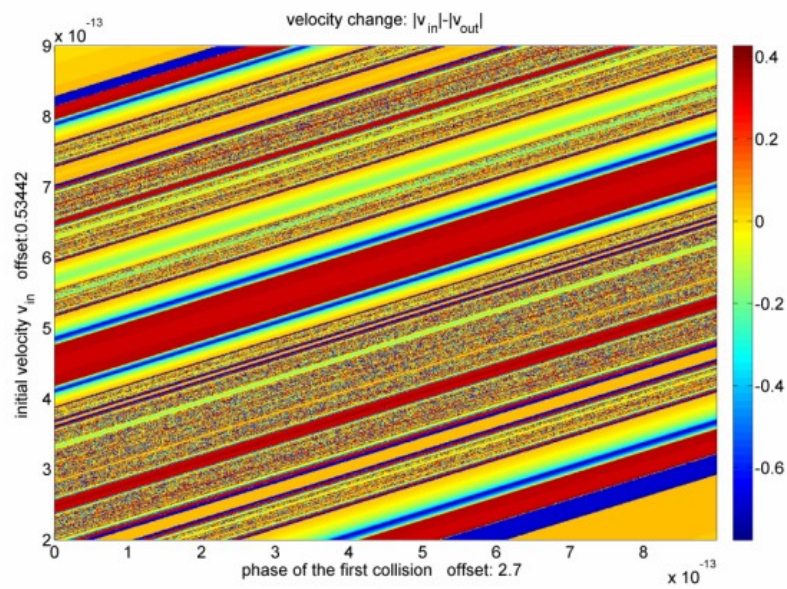

Figure 4.12: Enlargement of Fig. 4.9 by 10^5

To underline that this scattering process is indeed chaotic we enlarge the scattering function further and increased the resolution up to the numerical limit of 10^{-16} at a representative set of points. Fig. 4.12, Fig. 4.13 and Fig. 4.14 show some enlargements of region 6 at different scales. The structure of chaotic scattering continues on all accessible scales and the singularities form a fractal. Additionally, we found that the chaotic parts of the scattering function are prevalent on smaller scales, i.e. smooth parts become rare on small scales, which is typical for nonhyperbolic chaotic scattering. (Hyperbolic scattering is defined by the absence of stable KAM structures.) These plots also show that the fractal structure has to be visible in 2D scattering functions (such as $\triangle v(\varphi_c)$ for a constant v_{in}) as well. (We will use this property in subsection 4.2.3.)

4.2.1 Dwelltime

The dwelltime is defined as the time passed between the first and last collision of a particle with the barrier. This is *not* the time of flight between source, target and detector measured in experiments. We use this definition because it does not lead to artificially large dwelltimes for particles with a small outgoing velocity. It is known that in most systems that exhibit chaotic scattering singularities in the scattering function have a divergent dwelltime. This can be easily understood since the scattering function is infinitely sensitive to the initial conditions at singularities which can only be the case if the interaction time in continuous systems or the number of interactions in discrete systems between

Figure 4.13: Enlargement of Fig. 4.9 by 10^8

Figure 4.14: Enlargement of Fig. 4.9 by 10^{13}

target and particle diverges as well. Say we choose an initial condition (v_{in}, φ_c) resulting in a long time delay and, for example, 1000 collisions before leaving the scattering region. Then a very small perturbation would change the dwelltime by a small percentage leading to say 1001 collisions. But this additional collision will completely change the outgoing velocity and thus the scattering function. (This explanation has been employed by Edward Ott in Ref. [16].) As the mapping in this system is discrete, only the number of collisions at the singularities has to diverge. However, we found that the dwelltime of all singularities involved in chaotic scattering diverges as well. The number of collisions per time unit is actually a constant for all trapped particles at four collisions per period of the driving, exactly like particles on quasi periodic orbits. There also exist isolated singularities at which either only the number of collisions or only the dwelltime diverges. These kinds of singularities do not form a fractal and will be examined in section 4.3.
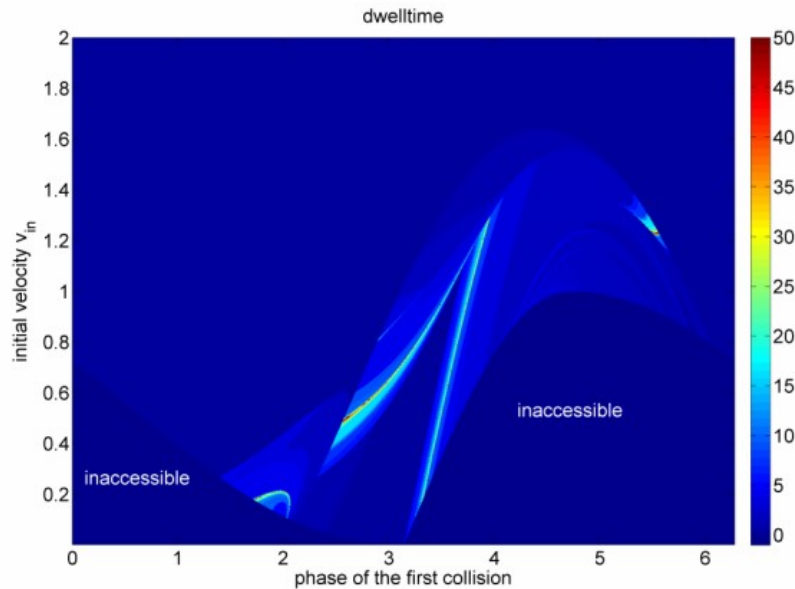

Figure 4.15: Dwelltime for $\frac{l}{a_0} = 0.4$, $\frac{V_0}{V_\omega} = 0.32$

In Fig. 4.15 we plot the dwelltime corresponding to Fig. 4.1. As expected the dwelltime is very small for all regions of normal scattering while it is significantly larger in the chaotic regions.

The figures Fig. 4.16, Fig. 4.17 and Fig. 4.18 show the dwelltime distributions corresponding to the magnified scattering functions of Fig. 4.12, Fig. 4.13 and Fig. 4.14. Evidently, the dwelltime becomes large in all chaotic regions. Another result visible in Fig. 4.16, Fig. 4.17 and Fig. 4.18 is that the maximal dwelltime of the singularities *and* the dwelltime of the smooth areas between them becomes larger on small scales. In fact the figures Fig. 4.16, Fig. 4.17 and Fig. 4.18 underestimate the maximal dwelltime of the singularities, because we have to cap the color map at a relatively low value to produce useful plots. This is not a problem in 2D plots of the dwelltime such as Fig. 4.19 where we show
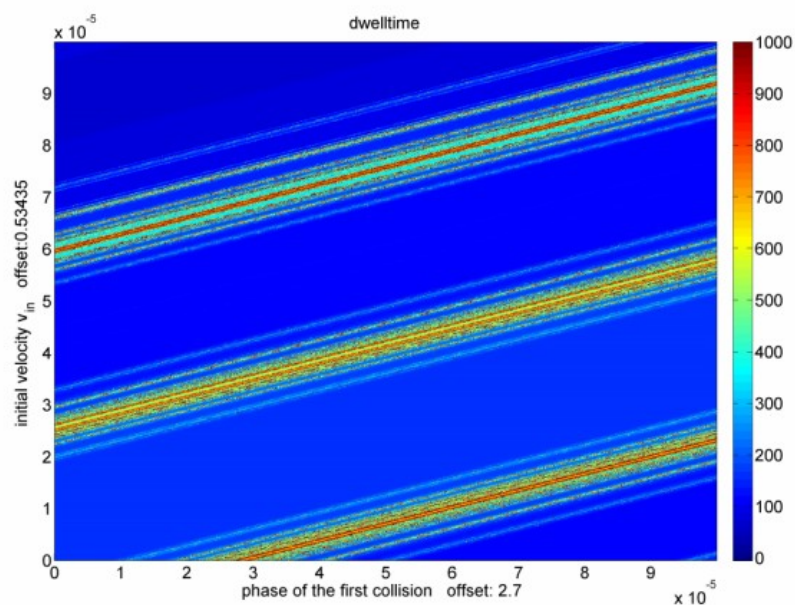
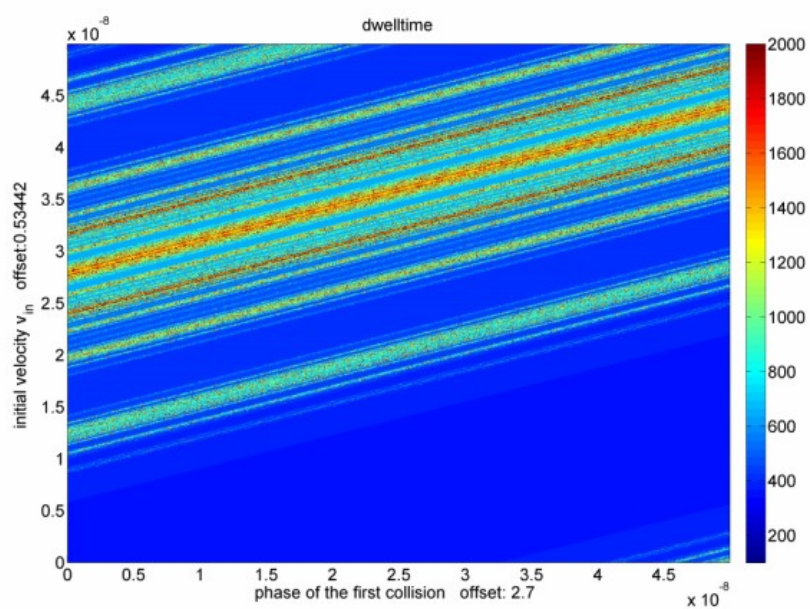Figure 4.16: Dwelltime of Fig. 4.12

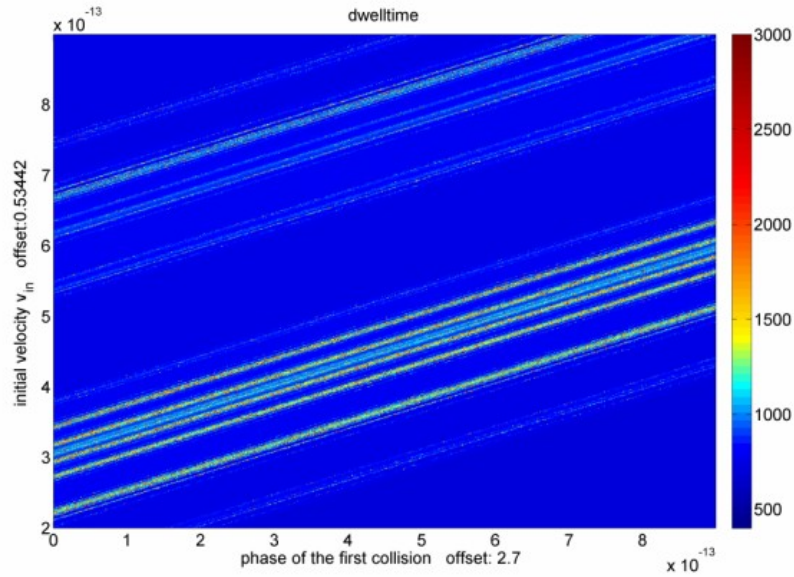

Figure 4.17: Dwelltime of Fig. 4.13

Figure 4.18: Dwelltime of Fig. 4.14

the dwelltime in the fractal part of the scattering function shown in Fig. 4.7. The same results, of course, are also valid for the number of collisions.

4.2.2 Stickiness and trapped particles

In subsection 4.2.1 we found that the dwelltime of the singularities in chaotic parts of the scattering function diverges. This means that incoming particles can become trapped by the repulsive potential for arbitrarily long times. Divergent dwelltimes are already a sound explanation for the singularities in the scattering function: As the number of collisions diverges the discontinuities of each collision process superimpose with each other and the scattering function becomes infinitely sensitive to the initial conditions. In this subsection we will show that the transition zone around the KAM tori in phase space is the cause of the divergent dwelltimes and the fractal structure of the singularities. The phenomenon of divergent dwelltimes in nonlinear systems is well known as stickiness. In this case a divergent dwelltime means that incoming particles have a nonzero probability $P(t_d)$ to stay in the scattering region for arbitrarily large dwelltimes t_d.

Almost all Hamiltonian dynamical systems show a coexistence of regular and chaotic motion. When a chaotic trajectory approaches the regular regions it can become stuck at the border between the chaotic and the regular regions. Such a trajectory traces the regular orbit it is sticking to and thus behaves almost regular itself. This is often called a laminar phase whereas the normal chaotic motion is called turbulent. The alternation between normal chaotic behavior and almost regular laminar phases is called intermittency. Stickiness leads to long time correlations and unusual transport properties such as anomalous diffusion. It does not affect the ergodicity of the chaotic component of phase space
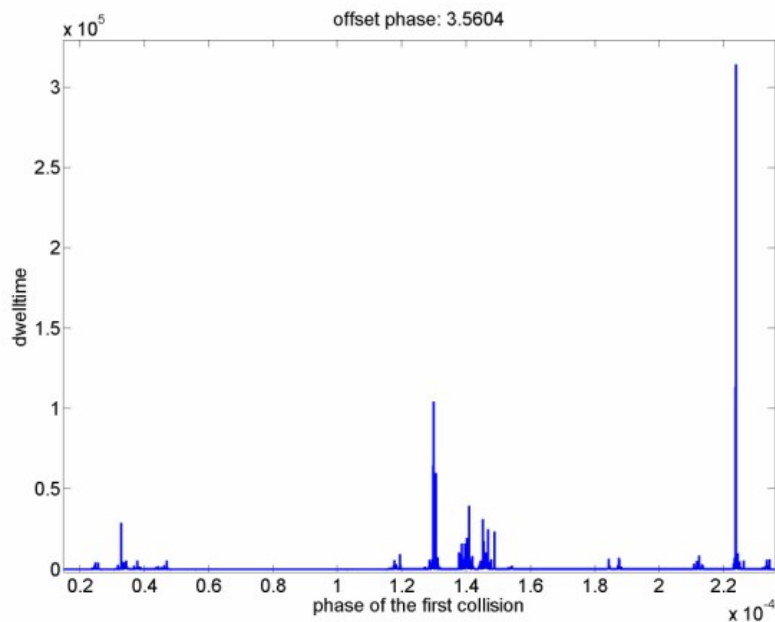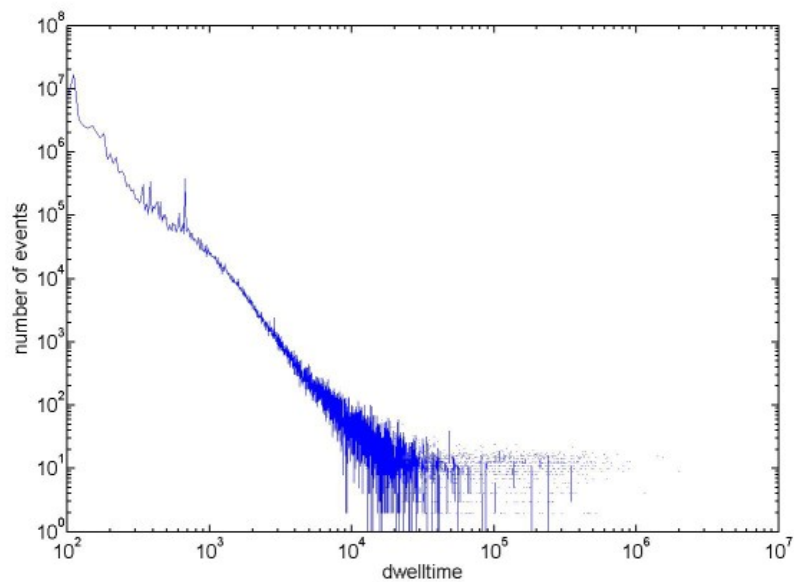
Figure 4.19: Dwelltime of Fig. 4.7

Figure 4.20: Distribution of dwelltimes

since chaotic trajectories do not spend more time in the sticky region then in other parts of phase space of equal volume. However, stickiness leads to long *successive* times spent in the sticky region. Stickiness is characterized by an algebraic sticking time distribution $P(t_d) \sim t_d^{-\gamma}$, whereas in a purely chaotic system $P(t_d)$ is approximately an exponential function. (See Ref. [17]) The distribution of dwelltimes of $n = 10^{10}$ random initial conditions in a small chaotic part of phase space is plotted in Fig. 4.20. As you can see the function follows approximately a power law. The probability of finding a dwelltime larger than $t_d = 1000$ for initial conditions chosen at random from the full range of $\varphi_0 \in [0, 2\pi]$ and $v_{in} \in [0, 2]$ is very small at around $p = 10^{-6}$. The exponent γ of the sticking time distribution depends on the type of stickiness and the investigated system. There are two broad types of stickiness in Hamiltonian systems:

Stickiness around an island of stability: This type of stickiness is due to the cantori of stable sub-islands surrounding the stable island. These provide a partial barrier for the transport of chaotic orbits through them. The flux through a cantorus can (in some systems) be calculated by using the scaling properties of the fractal structure. This leads to the Markov-tree model of stickiness and allows a calculation of the exponent γ. It is the prevalent type of stickiness in this system and it is the origin of the algebraic sticking time distribution. I've already shown in chapter 3 that the stable islands are surrounded by a fractal structure of sub-islands. It is not possible to plot the cantori themselves but their existence is proven by the KAM-theorem.

Stickiness at marginally unstable periodic orbits: The other source of stickiness are unstable periodic orbits (UPO) or rather marginally unstable periodic orbits. Trajectories close to the stable manifold of an UPO follow this manifold and approach the periodic orbit. Eventually, these trajectories deviate from the UPO again, following the unstable manifold, but if the eigenvalue λ of the UPO is only slightly larger than 1, which is the case for marginally unstable periodic orbits, the trajectory will stay close to the UPO for very long times. The existence of families of UPOs has been proven for the driven barrier in section 3.7 and their directions of flow have been investigated in section 3.9. This second type of stickiness is the typical origin of chaotic scattering. All points on the intersection of the stable manifolds with the manifold of initial conditions lead to infinite dwelltimes and are thus singularities of the scattering function. When this intersection is a fractal the scattering process becomes chaotic.

In most systems both types of stickiness play a role. The stickiness at asymptotic curves has been investigated by G.Contopoulos and M. Harsoula in Ref. [18]. The authors found stickiness effects far from the stable islands on the stable manifolds of unstable periodic orbits in the standard map. This second type of stickiness is directly linked to the first type because particles stuck on the stable manifold of an UPO can follow it into a sticky region of the first type where they can become trapped by the KAM-cantori.

We now want to examine the stickiness in our system in detail. The algebraic dwelltime distribution in Fig. 4.20 indicates that the long dwelltimes we have seen are due to cantori around the stable island. However, the stable island
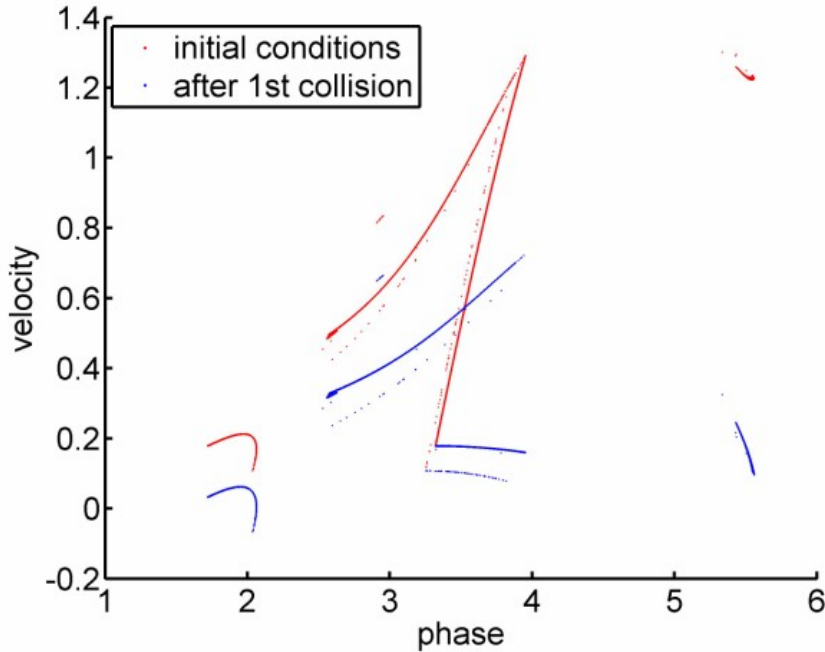
Figure 4.21: Initial conditions leading to stickiness

is situated deep within the inaccessible zone for all parameters $(\frac{V_0}{V_\omega}, \frac{l}{a_0})$ of the system; not even the belt of unstable periodic orbits is accessible directly. This suggest that the stable manifolds, which reach out of the inaccessible zone, play an important role. In Fig. 4.21 we have plotted in red all initial conditions leading to dwelltimes larger than 1000 for $\frac{V_0}{V_\omega} = 0.32$ and $\frac{l}{a_0} = 0.4$. (This corresponds to Fig. 4.1.) To compare this with the phase space in Poincaré sections we have to remember that we plot the velocity *after* a collision over the phase of the collisions in the Poincaré sections, whereas the initial conditions shown in red are the *incoming* velocity and the phase of the collisions. Thus we plot the ensemble after the first collision in blue in Fig. 4.21.

The corresponding Poincaré section and the UPOs of period one to 21 (84 in the full nonrestricted Poincaré section) are plotted in Fig. 4.22 (How this plot is created is described in section 3.7). A Poincaré section of the entire phase space is plotted in Fig. 3.1. The stable manifolds corresponding to these UPOs are plotted in black in Fig. 4.23. (See section 3.9 for details on the manifolds of UPOs.) Of the stable manifolds, Fig. 4.23 shows only the collision with the left edge of the barrier. The initial conditions leading to stickiness from Fig. 4.21 are also shown as red circles. As one can see, the initial conditions leading to very large dwelltimes are *exactly* the intersection of the initial conditions with the stable manifolds.

This proves that the stable manifolds are responsible for catching the incoming particles and leading them to the stable island. Once the particles have reached the transition zone around the outermost regular orbit they become trapped there by systems of cantori. To illustrate this we iterate the initial
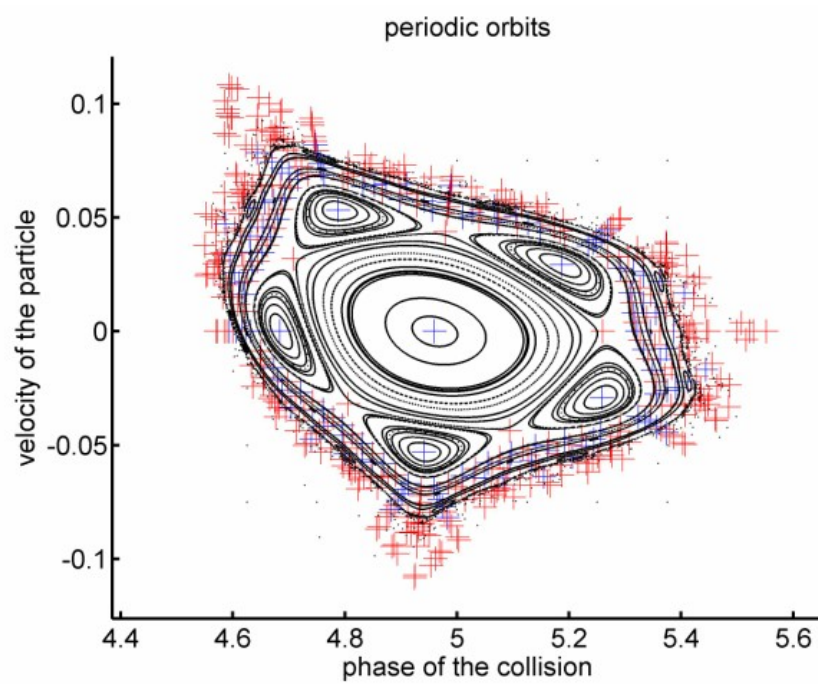
Figure 4.22: Poincaré section and UPOs for $\frac{V_0}{V_\omega} = 0.32$ $\frac{l}{a_0} = 0.4$
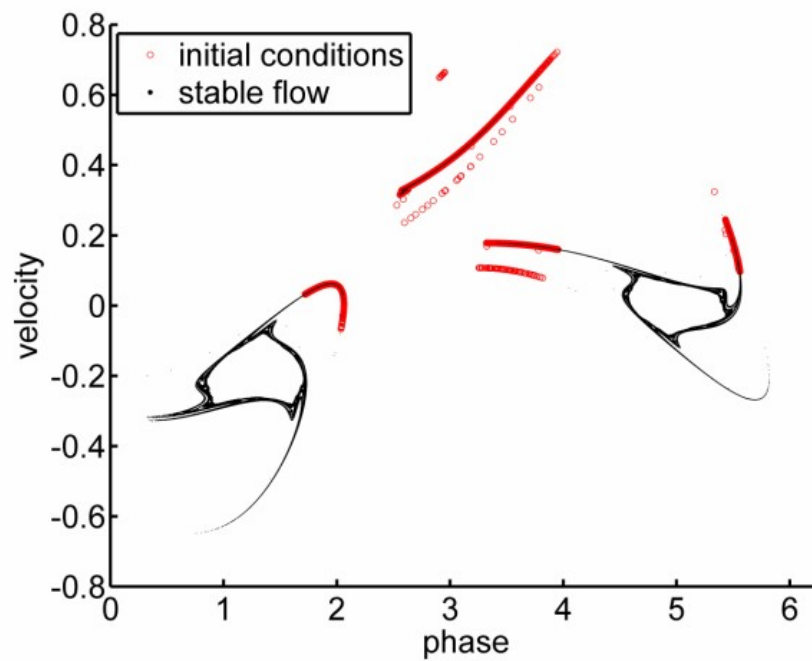

Figure 4.23: The stable manifolds and the initial conditions leading to stickiness

conditions of Fig. 4.21 for 300 collisions and plot the resulting Poincaré section in Fig. 4.24(a). The sticky particles follow the stable manifolds into the border region of the stable island. Time-position plots of the trajectories in this region show that the sticky particles trace the outermost regular orbit. The next 300 collisions of the ensemble are plotted in Fig. 4.24(b). This figure reveals that some of the sticky particles have left the stable island on the unstable manifolds of the UPOs.

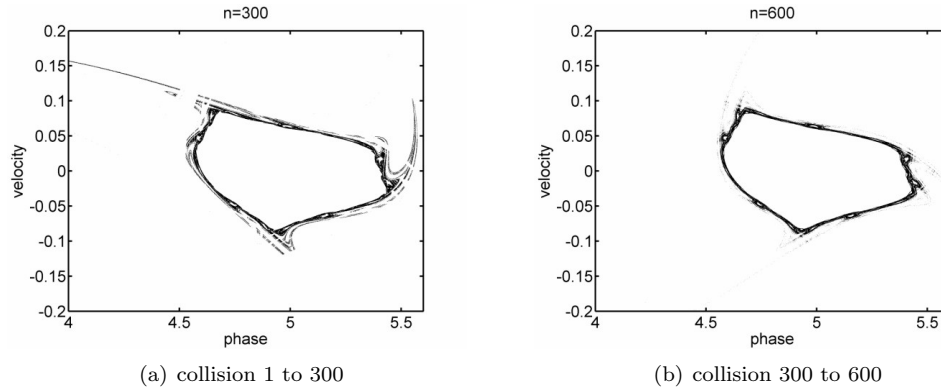(a) collision 1 to 300   (b) collision 300 to 600

Figure 4.24: Poincaré section of the trapped particles

4.2.3   Uncertainty dimension

Another way of characterizing the scattering process is to determine the fractal dimension of the scattering function. Since it is numerically tedious to calculate the box-counting dimension we determine the uncertainty dimension of the 2D-scattering function as described in Ref. [19]. To calculate the box-counting dimension of a 3-dimensional curve we would have to cover the space with a fine grid of cubes of edge length r and then count the number of boxes $N(r)$ being covered by the scattering function. This is done for different cube sizes r until we can approximate the limit of the box-counting dimension:

$$d_b = \lim_{r \to 0} \log \left(\frac{N(r)}{1/r} \right) \tag{4.4}$$

The problem of the box-counting method is that in nonhyperbolic systems this limit converges only very slowly and the total number of required cubes grows like $N_c(r) \sim \frac{1}{r^3}$. Thus the numerical complexity becomes unsurmountable. The uncertainty dimension is much easier to determine, not least because it is defined for the 2D scattering functions such as Fig. 4.6: For a fixed value of the "uncertainty" ε we randomly choose a set of initial conditions $\varphi_0 \in [\varphi_1, \varphi_2]$ (where φ_0 is the phase of the first collision) and calculate the number of points N_{φ_0} which satisfy $|f(\varphi_0) - f(\varphi_0 + \varepsilon)| > K$, where K is a typical scale of the scattering function. These N_{φ_0} points are called uncertain because at these φ_0 the scattering function cannot be resolved by a resolution of ε. The number of uncertain points N_{φ_0} is divided by the total number of points used to obtain

the uncertain fraction $f_u(\varepsilon) = \frac{N_{\varphi_0}}{N_{total}}$. The uncertainty dimension is defined as:

$$d = 1 - \lim_{\varepsilon \to 0} \left[\frac{\ln(f_u(\varepsilon))}{\ln(\varepsilon)} \right] \tag{4.5}$$

As described in Ref. [19], this dimension depends on the chosen interval $[\varphi_1, \varphi_2]$ from which the initial conditions are taken if the scattering is nonhyperbolic. The reason for this is that the fractal structure of singularities is denser on smaller scales and, therefore, the uncertainty dimension rises.
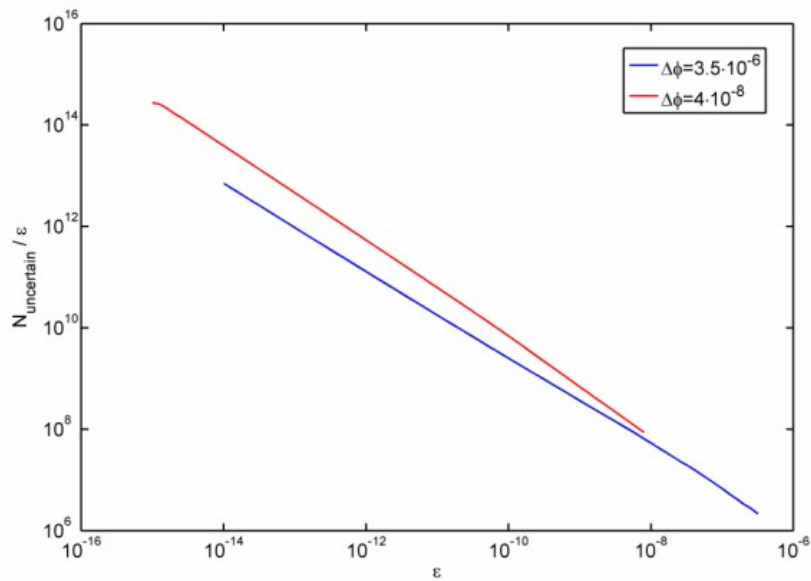

Figure 4.25: Uncertainty dimension on different scales

To determine d in the cut of the scattering function plotted in Fig. 4.7 we used a total number of $5 \cdot 10^6$ random initial conditions φ_0 in the interval $[\varphi_1, \varphi_1 + \Delta\varphi]$ for $\varphi_1 = 3.560579855$ and calculated $f_u(\varepsilon)$ for $\varepsilon \in [10^{-15}, 10^{-7}]$ and plotted $\frac{f_u(\varepsilon)}{\varepsilon}$ as a function of $\frac{1}{\varepsilon}$ on a log-log scale in Fig. 4.25 for $\Delta\varphi = 3.5 \cdot 10^{-6}$ and $\Delta\varphi = 4 \cdot 10^{-8}$. We changed K in a range of $K = 0.1$ to $K = 1.0$ and found no dependence of the uncertainty dimension on K. The initial velocity is fixed at $v_{in} = 1.0$. As predicted in Ref. [19] the calculated uncertainty dimension becomes larger on smaller scales $\Delta\varphi$. A fit of $f_u(\varepsilon)$ in Fig. 4.25 yields $d = 0.86$ for $\Delta\varphi = 3.5 \cdot 10^{-6}$ and $d = 0.95$ for $\Delta\varphi = 4 \cdot 10^{-8}$. In [19] the authors argue that in nonhyperbolic scattering the uncertainty dimension has to be exactly $d = 1$. (The scattering process at hand is clearly nonhyperbolic; the algebraic dwelltime distribution in Fig. 4.20, the scale dependence of the density of singularities and the existence of KAM tori proves this.) From our numerical simulations we conclude that in the limit of very small interval lengths $\Delta\varphi$ the uncertainty dimension should approach this predicted limit of $d = 1$.

4.3   Other singularities

We already mentioned the existence of singularities for which only the dwelltime or the collision number diverges in section 4.2.1. The origin of these singularities is not stickiness but different processes. In the driven barrier these singularities are isolated and do not create nontrivial dynamics. However, in Ref. [20] and Ref. [21] it has been shown that these processes can create a form of chaotic behavior that has been called dilute chaos.
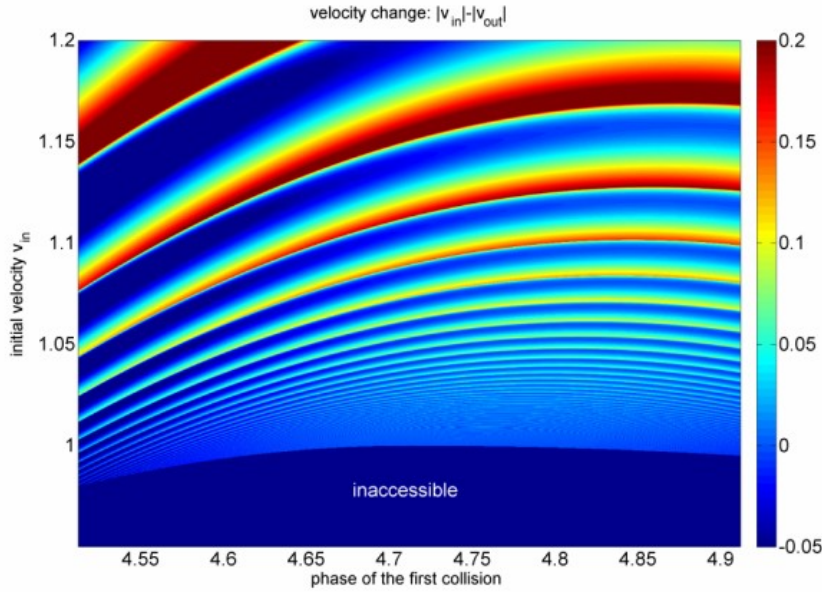

Figure 4.26: Scattering function around the whispering gallery

The first such singularity is at $v_{in} = 1.0$ and $\varphi_0 = \frac{3\pi}{2}$ in Fig. 4.1 and is called "whispering gallery" in analogous static systems. (Parameters: $\frac{V_0}{V_\omega} = 0.33$ and $\frac{l}{a_0} = 0.4$.) At this point the number of collisions diverges whereas the dwelltime plotted in Fig. 4.15 is small, at exactly $t_d = \frac{T}{2} = \pi$, where T is the period of the driving function. Fig. 4.26 shows an enlargement of the singularity. The system of arcs around the singularity, which is itself only visible as a tiny dot in Fig. 4.26, continues on all scales and each arc has one more collision than it's outer arc.

Fig. 4.27 shows a typical t-x-plot of a trajectory near the singularity. The particle collides with the barrier near it's zero crossing at $\varphi = \frac{3\pi}{2}$ with a velocity infinitesimally larger than the barrier's velocity of $v_{in} = 1.0$. The particle is reflected and slightly decelerated in such a way that it quickly collides with the barrier again, which decelerates due to it's own harmonic time law. This behavior is universal for all time-dependant chaotic systems with a concave time law.

The second type of singularity, for which only the dwelltime diverges, is a so called low velocity peak (LVP), plotted in Fig. 4.28. This type of singularity only appears for different parameters, in this case $\frac{V_0}{V_\omega} = 1$ and $\frac{l}{a_0} = 2.5$. The
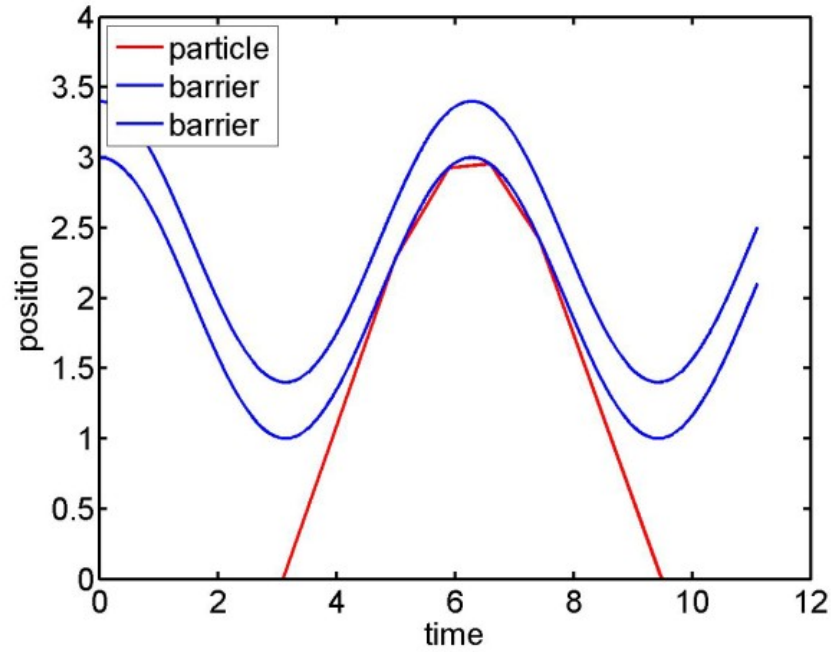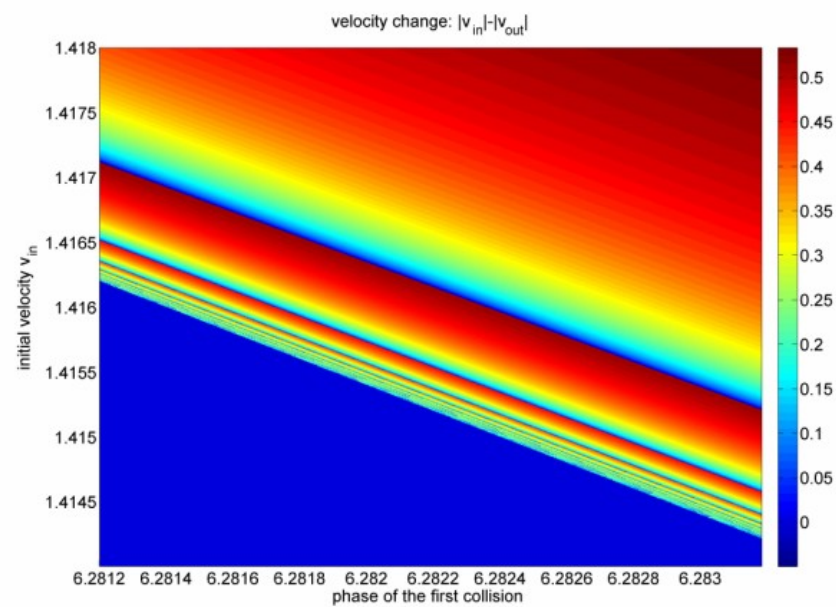
Figure 4.27: Trajectory of the whispering gallery

Figure 4.28: Scattering function around a LVP

coordinates of the singularity are $\varphi_0 = 1\pi$ and $v_{in} = \sqrt{\frac{V_0}{V_\omega}} = 1$. At this phase the barrier has reached its maximum position and has a velocity of zero. When a particle hits the barrier at this phase with a velocity that is just large enough to be transmitted, i.e. $v_{in} = \sqrt{\frac{V_0}{V_\omega} + \epsilon}$, its velocity becomes $v_2 = \sqrt{\epsilon}$ according to equation 2.5. Thus the velocity of the incoming particle can become arbitrarily small after the first collision.
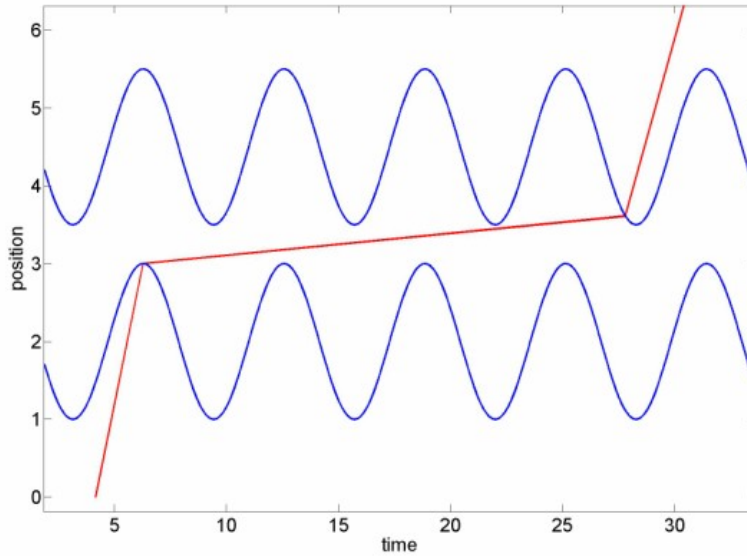

Figure 4.29: Trajectory of a LVP

A typical trajectory near the singularity is plotted in Fig. 4.29. Because the barrier's width l is greater than twice the amplitude a_0, the particle travels for a long time $t = \frac{l - 2a_0}{v_2}$ inside the barrier. Therefore the dwelltime diverges for $\epsilon \to 0$ while the number of collisions is exactly 2. This kind of trajectory can only appear of the width of the barrier l is larger then twice the amplitude a_0.

Papachristou et al. investigated in Ref. [20] and Ref. [21] a system of oscillating hard discs. This system possesses unstable periodic orbits near the low velocity peaks. The influence of the low velocity peaks on the heteroclinic intersections of the unstable periodic orbits creates completely new chaotic dynamics in that system. Here, the low velocity peaks appear only isolated.

4.4 Parameter dependence of the scattering process

In section 4.2 we found that the origin of the chaotic scattering we observed was the KAM island in phase space. We've also shown in section 3.3 that the stable orbits disappear for parameters $(\frac{V_0}{V_\omega}, \frac{l}{a_0})$ outside the area marked in Fig. 3.6. The unstable periodic orbits also exist only in this part of parameter space, as

shown in section 3.7. From this we conclude that chaotic scattering only appears for the parameters $(\frac{V_0}{V_\omega}, \frac{l}{a_0})$ below the curve in Fig. 3.6. To test this assumption we covered the parameter space in the range of $\frac{l}{a_0} \in [0, 3]$ and $\frac{V_0}{V_\omega}$ $in[0, 3]$ with a grid of 100 points and simulated the scattering process at each of them. We found that, indeed, the scattering process is only chaotic for parameters which permit stable orbits. The isolated singularity called "whispering gallery" in section 4.3 exists for all parameters whereas the low velocity peaks can exist only for $\frac{l}{a_0} > 2$ and $\frac{V_0}{V_\omega} > 1$.

4.5 Transmission of a particle packet

Vorobeichik et al. have analyzed the tunneling through a periodically driven square potential barrier in Ref. [11]. (See also Ref. [9] and [12].) They found that the transmission coefficient as a function of the particle energy has resonances below the minimal tunneling energy of the static system when the interaction time and the barrier period are of similar order of magnitude. For typical system parameters this is the case for high driving frequencies. For a Gaussian-shaped barrier these resonances disappear in the limit of $\omega \to \infty$ and the transmission function becomes smooth again, as shown in Ref. [9]. Fig. 4.30 is taken from Ref. [11] and shows the results of the calculation.
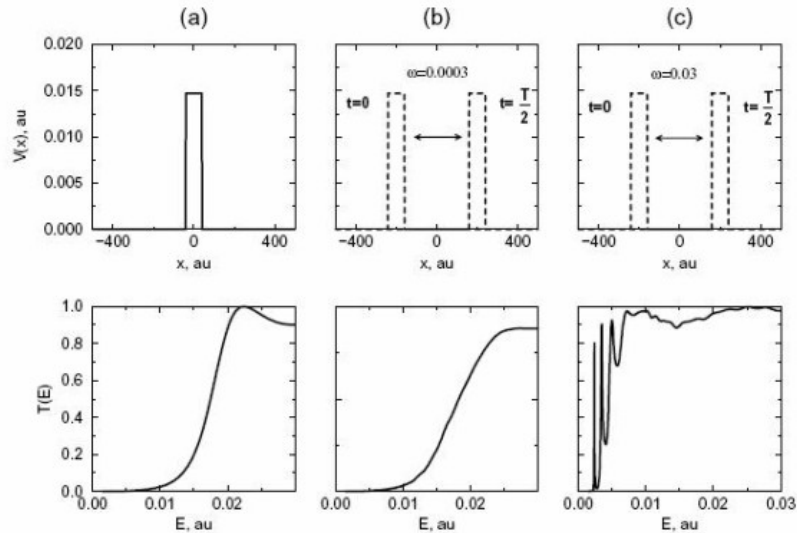

Figure 4.30: Transmission function for different frequencies in the quantum system (Copied from Ref. [11])

The authors could explain the resonances by approximating the oscillating barrier in the high frequency regime with an effective potential. This is the time average of the oscillating barrier:

$$V_{eff}(x) = \frac{1}{T} \int_0^T V(x,t)dt \qquad (4.6)$$

The integration of equation 2.1 yields:

$$V_{eff}(x) = \frac{V_0}{\pi} \begin{cases} \arccos\left(\frac{x-l/2}{a_0}\right) \arccos\left(\frac{x+l/2}{a_0}\right), & \text{if } -(a_0 - \frac{l}{2}) \leq x \leq a_0 - \frac{l}{2}; \\ \arccos\left(\frac{x-l/2}{a_0}\right), & a_0 - \frac{l}{2} \leq x \leq a_0 + \frac{l}{2}; \\ \arccos\left(-\frac{x+l/2}{a_0}\right), & -(a_0 + \frac{l}{2}) \leq x \leq -a_0 + \frac{l}{2}; \\ 0, & \text{else.} \end{cases}$$

$$(4.7)$$

For high driving frequencies this function is a good approximation of the oscillating potential in the quantum system. As Fig. 4.31 illustrates, V_{eff} is a double-barrier potential with a maximum height of $V_{max} = 4.3 \cdot 10^{-3}$. The potential well between the potential's peaks allows resonant states inside of it. Vorobeichik et al. have shown that the pronounced resonances in the transmission are exactly in resonance with these bound states. This means that an incoming particle has a maximal transmission probability if it can tunnel through the first barrier of V_{eff} into a resonant state, from where it can then tunnel through the second barrier of V_{eff}. This kind of transmission enhancement is also known from interferometry.
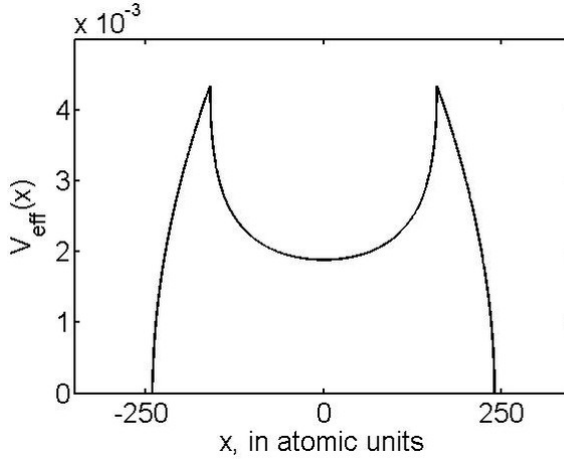

Figure 4.31: The effective time averaged potential

Since the system analyzed in [11] is identical to the system analyzed here it makes sense to compare the results in the quantum regime presented above with a classical simulation. To do this we use the same parameters for the barrier: $a_0 = 200$, $l = 80$, $m = 0.1$, $V_0 = 0.0147$ and the oscillation frequency ω as in the three cases above: $\omega = 0$, $\omega = 3 \cdot 10^{-4}$ and $\omega = 3 \cdot 10^{-2}$. The corresponding effective parameters would be $\frac{l}{a_0} = 0.4$ and $\frac{V_0}{V_\omega} \to \infty$, $\frac{V_0}{V_\omega} = 81.6$ and $\frac{V_0}{V_\omega} = 0.0082$. To simulate the transmission of a packet of trajectories we distribute an initial ensemble of 5000 particles according to a Gaussian function in position and velocity. The transmission coefficient shows not only a dependence on the mean velocity of the ensemble, it also depends on the shape and width of the initial ensemble, and to some extend of the initial phase as explained in Ref. [9]. We use a minimal uncertainty wave packet (i.e. $\sigma_x \sigma_p = \frac{1}{2}$) which is broad in

position space and narrow in momentum space. This kind of initial conditions is not entirely unproblematic, as we will explain in detail in subsection 4.5.1. An ensemble of classical particles has an entirely different dispersion relation from a quantum wave packet. Therefore, we artificially force the ensemble to keep its shape in position space until it collides with the target.

Fig. 4.32 shows the results for our classical simulation. The transmission through the static wall is obviously a step function, since the classical dynamics does not allow tunneling through the barrier. For small driving frequencies the step function is slightly bent. This reflects the fact that the driving allows transmission of particles at energies below V_0 at phases in which the barrier has a high negative velocity. Surprisingly, the classical simulation coincides to an amazing degree with the results of the quantum mechanical analysis in the high frequency limit (Fig. 4.32(c)). Even the dependence on the initial phase of the ensemble is neatly replicated. This was unexpected because the model of the effective potential V_{eff} completely collapses in the classical regime. The scattering of classical particles on the static potential V_{eff} would simply reproduce a step function, since the classical mechanics just don't allow any tunneling into resonant states. It is important to note that the effective potential is generally ill suited to describe the dynamics of trapped particles in the classical regime. Although the effective potential could be used to explain the existence of trapped particles for high frequencies, we also find trapped particles for low frequencies, i.e. when the driving frequency and the oscillation frequency of the trapped particles are of similar order of magnitude. The trapping is not caused by an effective potential for high driving frequencies but by a synchronization of the motion of particle and barrier.

However, the explanation for the transmission resonances in the classical case is quite similar to the quantum case. The average number of collisions of the particles in the packet is plotted in Fig. 4.32(d) for $\omega = 0.03$. The maxima of the number of collisions coincide with the resonances of the transmission coefficient. This means that at these initial energies the bunch of particles enters the fractal region of phase space and becomes sticky (see section 4.2.2). That process massively enhances the transmission. Thus the quasi-periodic orbits are the classical analogon to the resonance states in the effective potential. (We have to mention that a lot of fiddly fine tuning of the initial conditions was necessary to exactly reproduce the resonances of Ref. [11]. You typically only get one, perhaps two, fuzzy resonances, if you don't chose the widths of the Gaussian distribution properly.)

Now that we have comprehensively studied the scattering processes in chapter 4, we are equipped with the tools to understand the analogy to the corresponding quantum dynamics. The full scattering function for $\omega = 0.03$ is plotted in Fig. 4.33 and an enlargement of the relevant part is shown in Fig. 4.34. The transmission function is shown in Fig. 4.35. Please note that these are the scattering functions for a *single* particle, not for a wave packet. These scattering functions show more chaotic regions than the scattering functions we have shown before, like Fig. 4.1, because at $\frac{l}{a_0} = 0.4$, $\frac{V_0}{V_\omega} = 0.0081$ the elliptic island is quite large and the stable manifold is created by an unstable periodic orbit of period 88, thus the stable manifold reaches out of the inaccessible zone on 22 spiral arms, some of which cause the chaotic scattering visible in Fig. 4.34.

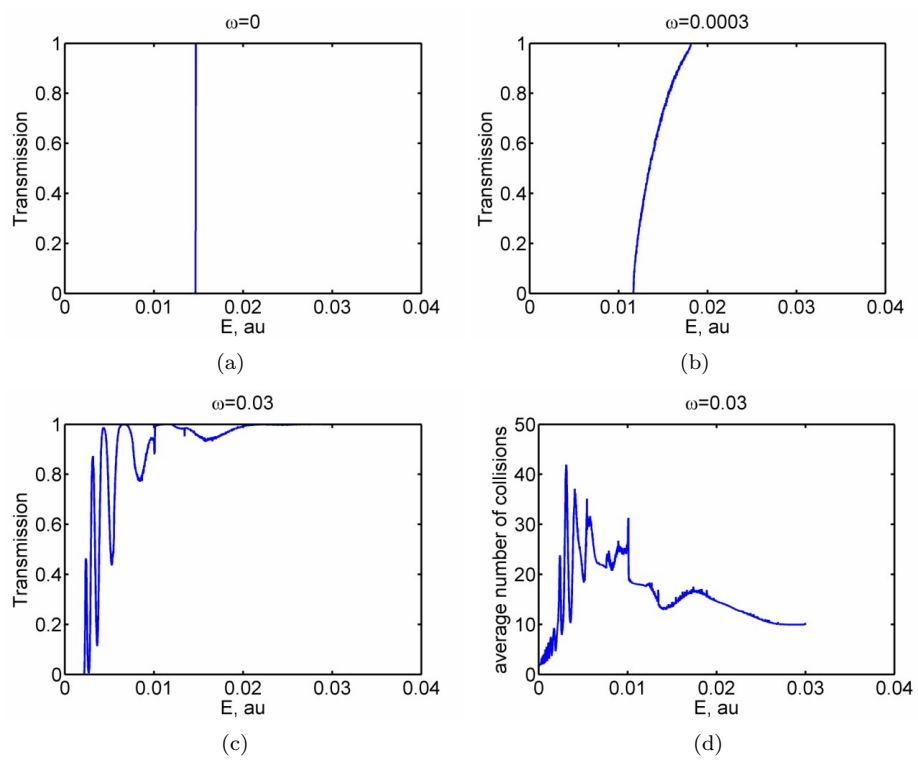It is not straightforward to interpret the relation between the transmission

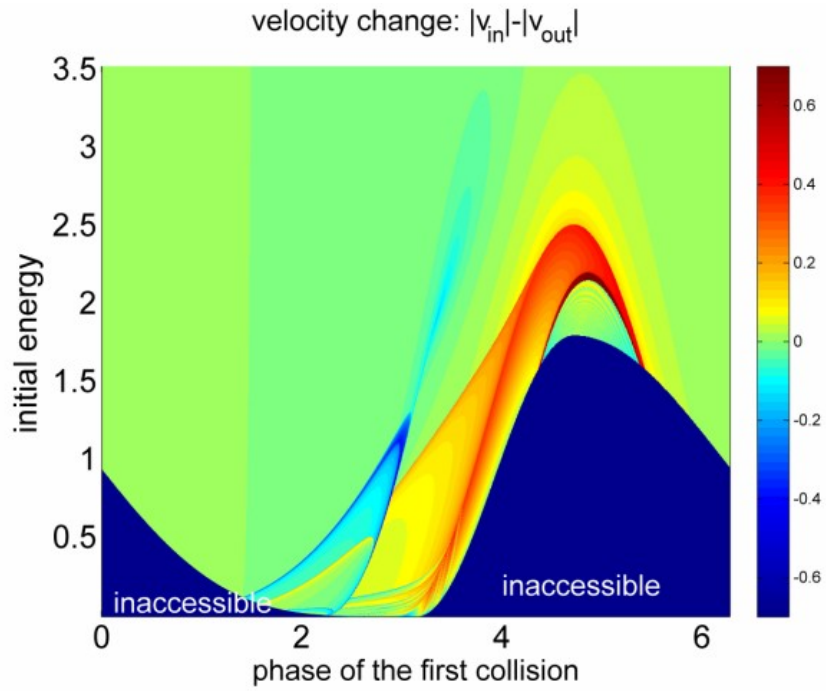Figure 4.32: Transmission function for different frequencies in the classical system

Figure 4.33: Scattering function for $\frac{V_0}{V_\omega} = 0.0082$ and $\frac{l}{a_0} = 0.4$
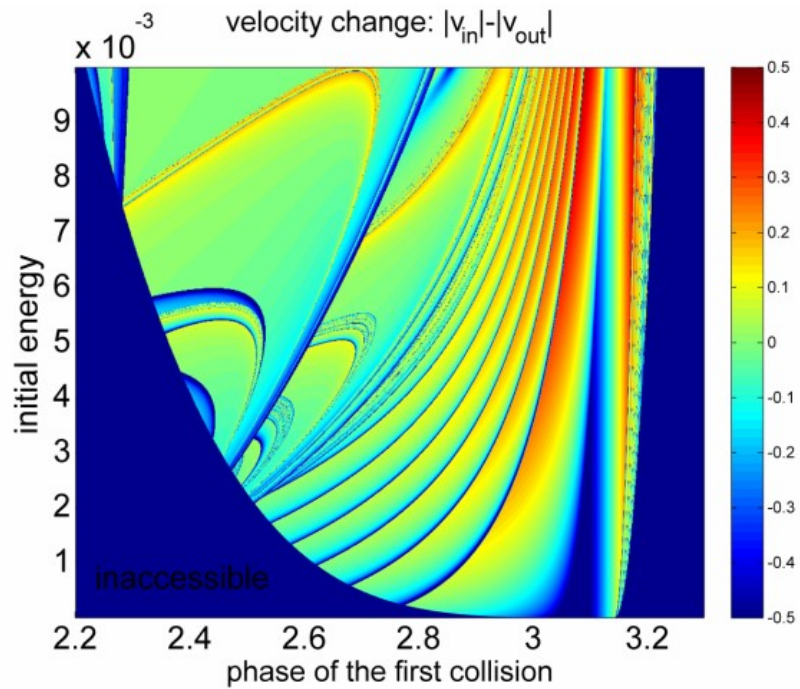

Figure 4.34: Enlargement of the scattering function in Fig. 4.33
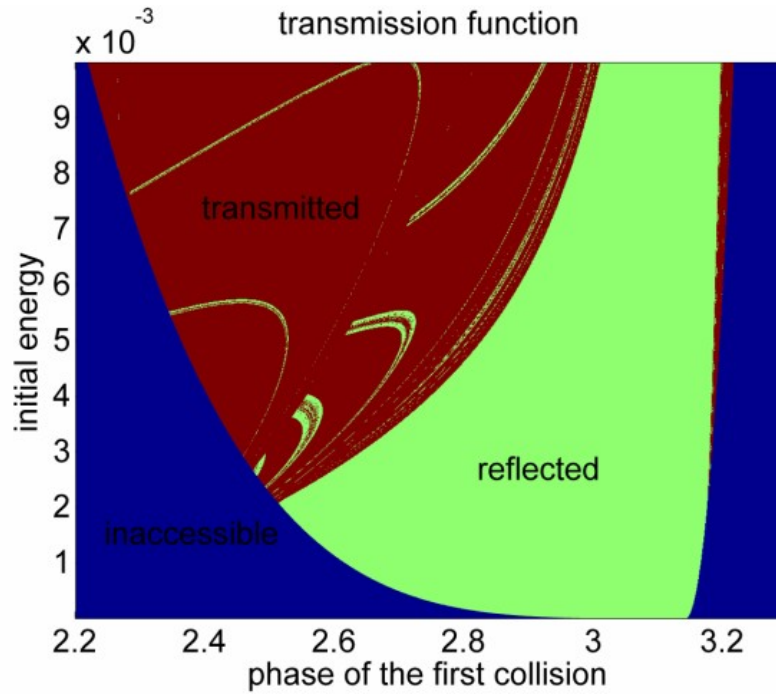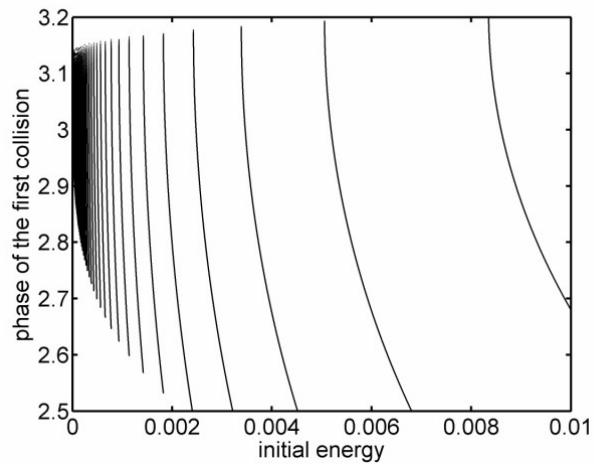
Figure 4.35: Transmission function for a single particle

Figure 4.36: Phase of the first collision as a function of the initial energy for a fixed initial phase and $\omega = 0.03$.
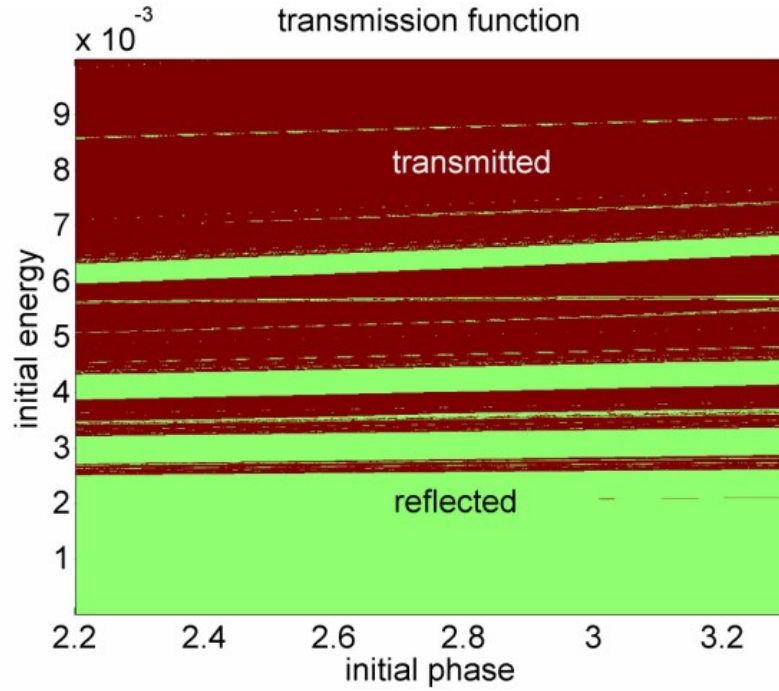
Figure 4.37: Transmission function for a single particle as a function of the initial energy and the *initial* phase for $\omega = 0.03$.

function of Fig. 4.35 and the resonances in Fig. 4.32(c). Fig. 4.35 does not show any resonances of the transmission as a function of the initial energy, at least not of the form seen in Fig. 4.32(c). This is not because Fig. 4.35 is the transmission function for just a single particle. The broadening effect of using a wave packet of particles actually changes the qualitative behavior very little. The real hiccup of Fig. 4.35 is that is shows the transmission as a function of the phase of the first collision and not as a function of the initial phase. Using the phase of the first collision as coordinate is very useful to understand the influence of the phase space structure on the scattering functions. But here, the initial phase of the incoming particle is the more appropriate coordinate, because this is the coordinate that is kept constant in the 2D plots of Fig. 4.32 and Fig. 4.30. The phase of the first collision, however, depends not only on the initial phase, it also depends on the velocity of the particles. In fact, the phase of the first collision depends critically on the initial velocity. This is because, in all these simulations, we deal with quite slow particles. The velocity of the particles at the first resonance is $v_{in} = 0.2$ whereas the barrier moves at a maximal velocity of $v_{max} = 6$. Therefore all collisions take place at a phase of around $\varphi = \pi$ when the barrier is in the minimum position. A slight change in the initial velocity thus changes the phase of the first collision drastically. This is shown in Fig. 4.36 in which we plot the phase of the first collision as a function of the initial energy for a fixed and arbitrary initial phase. The phase of the first collision, as a function of the initial energy, has a singularity at $E_{in} = 0$, which means that it oscillates infinitely fast for $E_{in} \rightarrow 0$. (This is the kind of function

you would also see for the scattering function around a low velocity peak, see section 4.3.) Thus, when E_{in} is varied, the phase of the first collision quickly oscillates, between the region in the middle of Fig. 4.35, where the particle is reflected, to the chaotic part on the left side in Fig. 4.35, where the particle is transmitted. A better way to visualize this process is to simply plot the transmission function over the *initial* phase in Fig. 4.37. This plot reproduces nicely the energy resonances of Fig. 4.32(c) and the weak dependence on the initial phase. But now we understand, that these resonances are not resonances of in the *interaction* of the particle and the barrier, as in the quantum regime. These resonances are produced simply by the propagation *to* the barrier, where the different collision phases lead to peaks in the transmission probability. This deeper insight largely devaluates the analogy between the quantum and the classical system.
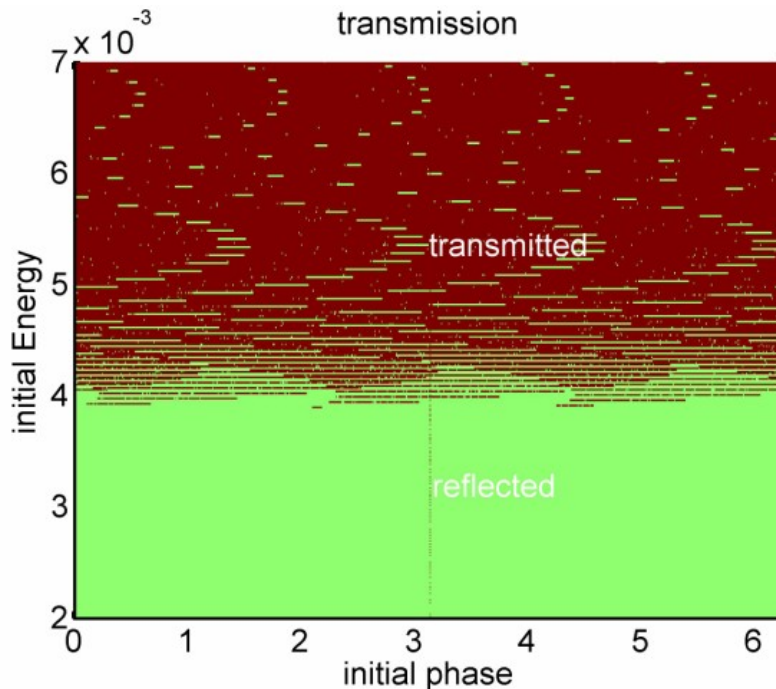

Figure 4.38: Transmission function for a single particle as a function of the initial energy and the *initial* phase for $\omega = 1$.

The transmission function for a very high driving frequency of $\omega = 1$ is plotted in Fig. 4.38. The structure of resonances still exists for high driving frequencies, but it is too fine to be resolved by an ensemble with a Gaussian momentum distribution of nonzero width.

4.5.1   The "classical wave packet" and its problems

Constructing an ensemble of classical particles in a way that the distribution of position and velocity mimic a quantum mechanical wave packet is fairly easy. However, it can also be very misleading! The problem of an ensemble of classical

particles is that it ultimately consists of individual and independent particles. Therefore the dispersion of such a "classical wave packet" has little resemblance to the dispersion in quantum mechanics. Given an ensemble with a mean velocity of $\overline{v}$ and velocity distribution width of σ_v the width of the distribution in position space will grow with the time t as

$$\sigma_x(t) \approx 2t \cdot \sigma_v + \sigma_x(t_0) \tag{4.8}$$

where $\sigma_x(t_0)$ is the initial position which is equal to $\sigma_x(t_0) = \frac{1}{\sigma_v}$ for a minimal uncertainty wave packet. Thus the position width of this packet will grow linearly in time, which is very unlike a quantum mechanical wave packet. To make matters worse, the initial position $\overline{x}_0$ of the ensemble cannot lie arbitrarily close to the scattering target (i.e. the barrier) because initially the distance of $\overline{x}_0$ and the target must be larger then $\sigma_x(t_0)$ to avoid an overlap between the initial ensemble and the target. Therefore the particles have at least a mean propagation time to the collision point of:

$$t_1 = \frac{\sigma_x(t_0)}{\overline{v}} = \frac{1}{\overline{v} \cdot \sigma_v} \tag{4.9}$$

The width of the position distribution at this time must therefore be at least:

$$\sigma_x(t_1) \approx \frac{2}{\overline{v}} + \sigma_x(t_0) \tag{4.10}$$

Since the relevant and interesting effects all occur at very small incident energies the position width of the ensemble will be very large (and much larger then $\sigma_x(t_0)$) when the packet collides with the target. Thus an initially well formed Gaussian-shaped distribution completely smears out.
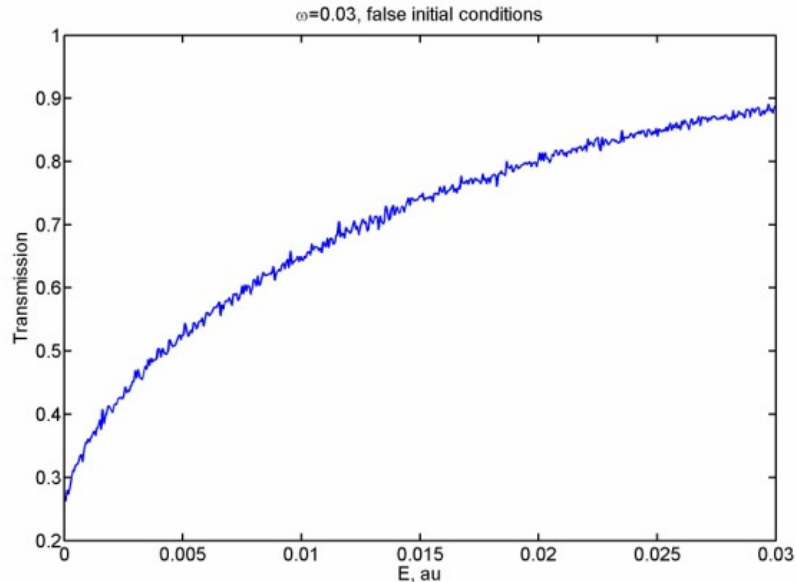

Figure 4.39: Transmission function of a flawed ensemble of particles

The transmission function of an initial ensemble with a very broad spatial distribution does not exhibit the resonances of Fig. 4.32(c). When we used a Gaussian-shaped initial ensemble as described above to calculate the transmission at $\omega = 0.03$ the result was Fig. 4.39. This figure corresponds to Fig. 4.32(c), where we used more sophisticated initial conditions, and clearly shows that simply propagating a classical initial ensemble will not yield any results that could be related to the quantum regime.

Since it is not possible to create a classical ensemble that really imitates a quantum wave packet we made a compromise between the desire to have a comparison to the quantum regime and the necessity to use classical particles. We artificially forced the ensemble to keep its distribution in position and momentum space until the ensemble interacted with the barrier. Therefore Fig. 4.32 does not show the transmission function of a realistic classical ensemble. Fig. 4.32 should rather be understood as the transmission function of an initial ensemble that is prepared in such a way that its distribution in momentum and position space is a Gaussian function in the moment the ensemble hits the target.

Chapter 5

Conclusions and outlook

The aim of this thesis was to study the classical nonlinear dynamics in the system of a single driven square potential barrier with harmonically oscillating position. We found that, surprisingly, for some parameters the barrier possesses a stable periodic orbit. This means that, through the driving, the repulsive potential can trap particles in a small part of phase space. The periodic orbit is surrounded by an elliptic island of quasi-periodic orbits in phase space. We used Poincaré sections to visualize the phase space structure. The KAM islands around the central fixed points show the typical fractal structure of sub-islands and unstable periodic orbits. We used a powerful numerical method to locate these unstable orbits and their stable and unstable manifolds. On the analytic side of our analysis, we were able to analytically determine the position and stability properties of the central periodic orbit. The central periodic orbit exists only for a particular range of parameters, which we were able to analytically derive. We also analyzed in detail the dependence of the shape of the elliptic islands on the parameters. Thus, we have studied the entire phase space structure for the full range of parameters, which has so far not been done for this system.

Since most other works on driven barrier systems focus on the transmission probability of scattering trajectories, we also studied the scattering process in detail. We computed the energy change, transmission, dwelltime and the number of collisions as a function of the initial energy and the collision phase of the incoming particles. Due to the KAM island in phase space the driven barrier is a chaotic scatterer. Particles starting on the stable manifolds of the system's unstable periodic orbits become sticky and have divergent dwelltimes. This kind of behavior is typical for chaotic systems whose phase space is in parts integrable. We analyzed in detail the dynamics of the scattering process and its parameter dependence. Finally, we returned to the transmission of an Gaussian-shaped ensemble through the barrier and made comparisons with the quantum mechanical results in the literature. Even though this is a classical system, we found that the transmission probability of a suitably prepared ensemble is very similar to the transmission function in the quantum systems.

The results of this thesis all depend on the existence of a dynamical trapping process. The stable orbits which we discovered rely on the curvature of the harmonic driving law. When we used a sawtooth shaped driving law, we found no such stable orbits. It can be assumed that other suitably curved driving

functions lead to bounded motion as well. Likewise, our results do not depend on the exact shape of the barrier itself. The transmission function of a Gaussian-shaped barrier, for example, shows resonances similar to those found in this system. (See Ref. [9].)

In future works we want to investigate systems of many different oscillating barriers. This current work allows us to build lattices of driven barriers in which each barrier can have entirely different parameters. We expect to see interesting transport effects like anomalous diffusion and we will try to control the transport properties by changing the parameters of the individual barriers. By using an asymmetric driving law we want to realize a directed transport in such a chaotic system.

Bibliography

[1] P. Schmelcher and F. K. Diakonos. Detecting unstable periodic orbits of chaotic dynamical systems. *Physical Review Letters*, 78:4733–4737, 1997.

[2] M. Henseler, T. Dittrich, and K. Richter. Signatures of chaos and tunneling in ac-driven quantum scattering. *Europhysics Letters*, 49:289295, 2000.

[3] M. Wagner. quenching of resonant transmission through an oscillating quantum well. *Physical Review B*, 49:16544–16547, 1994.

[4] M. Wagner. photon-assisted transmission through an oscillating quantum well. *Physical Review A*, 51:798–808, 1995.

[5] Michael Henseler, Thomas Dittrich, and Klaus Richter. Classical and quantum periodically driven scattering in one dimension. *Physical Review E*, 64:046218, 2001.

[6] T. Timberlake and L. E. Reichl. Changes in floquet-state structure at avoided crossings: Delocalization and harmonic generation. *Physical Review A*, 59:2886–2893, 1999.

[7] B. Galdrikian, M. Sherwin, and B. Birnir. self-consistent floquet states for periodically driven quantum wells. *Physical Review B*, 49:13744–13749, 1994.

[8] Ilya Vorobeichik and Nimrod Moiseyev. Tunneling control by high-frequency driving. *Physical Review A*, 59:2511–2514, 1999.

[9] A Pimpale, S Holloway, and R J Smith. Tunnelling through moving barriers. *J. Phyr. A*, 24:3533–3550, 1991.

[10] Jiu-Yuan Ge and John Z. H. Zhang. Quantum mechanical tunneling through a time-dependent barrier. *Journal of Chemical Physics*, 105:8628–8632, 1996.

[11] I. Vorobeichik, R. Lefebvre, and N. Moiseyev. Field-induced barrier transparency. *Europhysics Letters*, 41:111–116, 1998.

[12] M. L. Chiofalo, M. Artoni, and G. C. La Rocca. Atom resonant tunnelling through a moving barrier. *New Journal of Physics*, 5:78.1–78.15, 2003.

[13] P. K. Papachristou, E. Katifori, F.K. Diakonos, E. Mavrommatis, V. Constantoudis, and P. Schmelcher. Formation of coherent pulse trains via scattering off oscillating barriers. 2007.

[14] W. H. Press, S. A. Teukolsky, W. T. Vetterling, and B. P. Flannery. *Numerical Recipes in C*. Cambridge University Press, second edition edition, 1997.

[15] P. Schmelcher and F. K. Diakonos. General approach to the localization of unstable periodic orbits in chaotic dynamical systems. *Physical Review E*, 57:2739–2746, 1998.

[16] Edward Ott. *Chaos in dynamical systems*. University of Cambridge, 1992.

[17] F. F. Karney. Long-time correlations in the stochastic regime. *Physica*, 8D:360–380, 1982.

[18] G.Contopoulos and M. Harsoula. Stickiness in chaos. *arXiv*, 2007.

[19] Yun-Tung Lau, John M. Finn, and Eward Ott. Fractal dimension in non-hyperbolic scattering. *Physical Review Letters*, 66:978–981, 1991.

[20] P.K. Papachristou, F.K. Diakonos, V. Constantoudis, P. Schmelcher, and L. Benet. Classical scattering from oscillating targets. *Physics Letters A*, 306:116126, 2002.

[21] P. K. Papachristou, F. K. Diakonos, V. Constantoudis, P. Schmelcher, and L. Benet. Scattering off two oscillating disks: Dilute chaos. *Physical Review E*, 70:056215, 2004.